國立臺灣大學電機資訊學院電機工程學系

博士論文

Department of Electrical Engineering

College of Electrical Engineering and Computer Science

National Taiwan University

Doctoral Dissertation

孔徑信號處理技術與其在超音波影像之應用

Aperture Domain Processing and Its Applications in

Ultrasound Imaging

王珣力

Shun-Li Wang

指導教授：李百祺 博士

Advisor: Pai-Chi Li, Ph.D.

中華民國九十八年七月

July, 2009

國立臺灣大學電機工程研究所
博士學位論文

孔徑信號處理技術與其在超音波影像之應用

研 究 生：王珣力

指導教授：李百祺　教授

經考試合格特此證明

博士學位論文考試委員：

指導教授　：

研究所所長：

中華民國九十八年七月

中文摘要

　　本論文主要研究超音波陣列系統的孔徑信號(aperture domain data)相關之成像方法與信號處理技術。一般系統廣泛運用的波束形成技術為延遲-加總法,此方法可藉由調整各頻道的時間延遲和權重而使得聲波波束可以電子式聚焦到特定深度及可以任意地調控與位移波束,並調整橫向解析度及波束形狀而使得掃描深度內皆為動態聚焦。在波束加總前的各頻道接收信號亦稱為孔徑信號。在傳統的系統裡,孔徑信號會因為資料量過於龐大而在波束加總後被捨棄,但延遲-加總法僅能獲得波束方向上的空間資訊反而使得超音波影像在臨床上的應用受到限制。本論文中將探討向量流速估計與相位偏移校正方法等兩種孔徑信號處理技術。

　　在第一部份流速估計的應用上,使用所提出的使用孔徑信號之二維流速估測方式來改善傳統的流速估計方法只能量測平行波束方向的流速分量。在這方法中一個沿著陣列方向之時間偏移量變曲線被建立並近似成為一次多項式來求得軸向與橫向速度分量。我們經由模擬和實驗來驗證方法的可行性,結果顯示所提出的方法能改善向量流速估計之誤差且其結果比傳統流速估計法來的更佳,並且可以實現即時二維血流量測。

　　在相位偏移校正的應用上,我們使用臨床乳房影像驗證一基於接收孔徑信號之同調性的旁瓣抑制法。傳統灰階超音波在乳房病灶偵測上常會因為對比解析度不足而使其效果被限制。由臨床實驗結果顯示相較於傳統基於相關性之方法,所提出的權重方法能顯著的改善乳房影像品質。

　　在本論文的第三部分,基於同調性的旁瓣抑制法也被延伸應用到高速超音波影像上,在這方法中使用一高精確度之 Capon 估計法來量測同調能量,並使用僅八次平面波激發與合成發射孔徑方法來達到高速成像。模擬和實驗結果皆顯示所提出之方法都能對對比度與病灶清晰度等影像品質有所改善。結果顯示這些基於同調性的方法能有效改善臨床上的病灶偵測,因我們所提出之方法無須任何聚焦誤差的假設便能有效降低旁瓣貢獻。本論文開發多種影像方法並有效提升流速與對比解析度有助於提升臨床診斷。論文最後亦將探討相關技術之延伸應用。

ABSTRACT

The purpose of this dissertation is to investigate various processing techniques for ultrasound image formation and signal processing based on aperture domain data for ultrasonic system using arrays. Conventionally, an array system utilizes the widely adopted delay-and-sum method to focus acoustic beams electrically at specific depths with arbitrary steering and shifting by the delay and weighting of each array element. This method can adjust lateral resolution and beam-shapes and therefore provides dynamic focusing throughout the scan depth. The data recorded from individual array channels prior to beam summation are referred to aperture domain data and are often discarded after beam summation due to a large data size. However, the delay-and-sum method only preserves the spatial information along the beam direction and therefore limits the clinical applications. In this thesis, two specific tasks of aperture domain data processing including vector velocity estimation and phase-aberration (i.e., focusing errors resulting from sound-velocity inhomogeneities) correction are investigated.

The first topic in this dissertation is the vector flow estimation. A conventional scanner can only estimate the flow velocity parallel to the beam axis. The proposed flow estimation technique uses aperture domain data for 2D flow-velocity estimation. A time-shift profile along the array direction is constructed and approximated by a first-order polynomial to determine the axial and lateral velocity components. The efficacy of the vector velocity estimation method is verified by simulations and experiments. The results demonstrate that the accuracy of the proposed method is comparable to existing vector velocity estimation method and real-time two-dimensional velocity vector estimation is feasible.

For phase-aberration correction, a sidelobe-reduction technique based on the coherence of the receive aperture domain data is tested with clinical breast data. The performance in lesion detection using B-mode ultrasound is often limited by poor contrast resolution. Experimental results demonstrate that the proposed weighting

method is feasible in breast imaging and rivals the conventional correlation-based method with significant image quality improvement.

In the third part of the dissertation, the coherence-based sidelobe-reduction technique is also extended to high-frame-rate adaptive imaging with a high accuracy Capon estimator to estimate the coherent energy. The high frame rate image is formed using plane-wave excitation and a synthetic transmit aperture method using only 8 firings. Significant improvement in contrast and lesion definition is demonstrated through the simulations and breast imaging experiments. The results demonstrate that these coherence-based methods are feasible to improve lesion detection in clinics since these techniques can effectively reduce sidelobe contributions without any assumption regarding the source of focusing errors. In summary, advanced imaging techniques were developed in this thesis to improve velocity and contrast resolution and thus increase diagnostic confidence in clinics. Potential extended application of these methods will also be described.
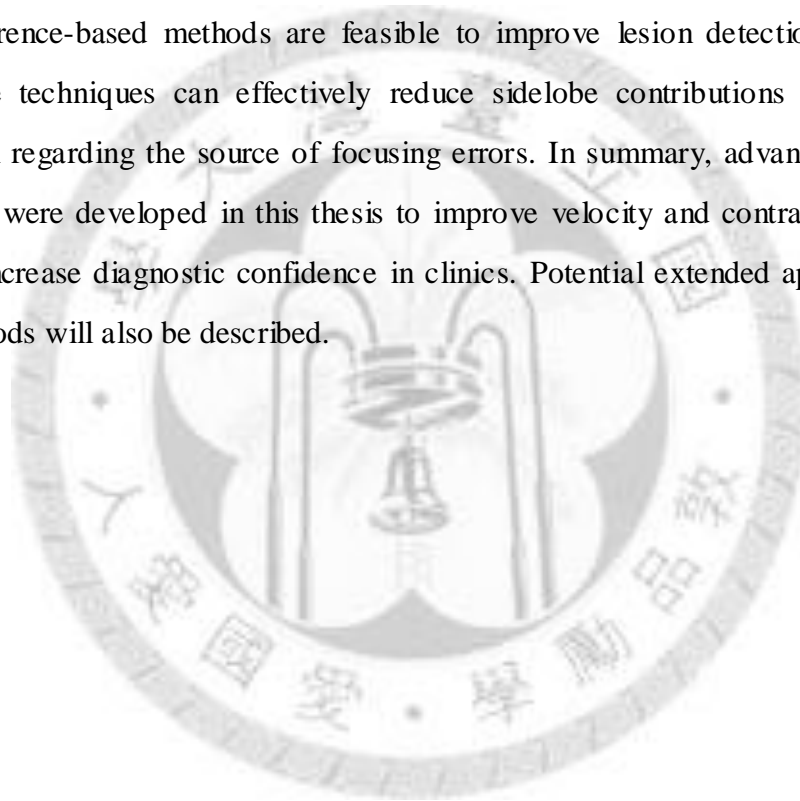
LIST OF SYMBOLS

A	envelope of receive data
A_n	envelope of the receive signal at channel n
a	denotes the half aperture size
$\mathbf{a}(\theta)$	steering vector
a_0	zeroth-order coefficient of the first-order time-shift polynomial
a_1	first-order coefficient of the first-order time-shift polynomial
B_n	energy level fluctuation factor
$C_n(t)$	cross-correlation function at channel n
CF	coherence factor
CF_{MVDR}	coherence factor using the MVDR method
c	sound velocity
$d\phi_{axial}$	phase shift of het_{axial}
$d\phi_{lateral}$	phase shift of $het_{lateral}$
$F\#$	F-number
f_0	center frequency of the emitted signal
filter(i)	coefficient of low pass filter
GCF	generalize coherence factor
het_{axial}	heterodyning function to remove the interaction between the axial velocity component
$het_{lateral}$	heterodyning function to remove the interaction between the lateral velocity component
I	$N \times N$ identity matrix
i	pulse index
k	wave number
$k_{lateral}$	wave number used in the lateral apodization function
L	number of subapertures
l	subaperture index
M	number of firings used for slow-time temporal averaging
M_0	prespecified cut-off frequency
N	total number of elements
n	channel index
PRI	pulse repetition interval
$P(\theta, t)$	array output power
$P_{MVDR}(\theta, t)$	array output power using the MVDR method
$p(k, t)$	Fourier spectrum
SNR	signal-to-noise ratio
R	range from the focal point to the center of the transducer

$R(t)$	auto-correlation function
$R_{xx}(t)$	spatial autocovariance matrix of the receive-channel data
$r(t)$	receive signal
T	correlation duration
t	arrival time of the receive signal
Var	variance
v_{axial}	axial velocity component
$v_{lateral}$	lateral velocity component
$\hat{v}$	estimate of vector velocity
$\hat{v}_{axial}$	estimate of axial velocity
$\hat{v}_{lateral}$	estimate of lateral velocity
$\mathbf{w}$	weighting vector
$\mathbf{w}_{MVDR}$	optimum weighting using MVDR method
X_n	channel position along the array direction
$\overline{X}$	mean of lateral positions
$x(t)$	aperture domain data
$\mathbf{x}_K(t)$	K-length block of sampled data
$y(t)$	beam sum data
$y_{weighted}$	weighted beam sum data
α	improvement ratio
β	lateral-to-axial estimation error ratio
Δ	prespecified weighting constant
ΔX	lateral displacement
ΔZ	axial displacement
$\Delta\tau$	arrival time shift
$\Delta\varphi$	phase difference of the $R(t)$
ε	diagonal loading constant
λ	wavelength
θ	beam steering angle
$\hat{\theta}_{Doppler}$	estimate of Doppler angle
ρ	correlation coefficient
σ	standard deviation
τ	arrival time
τ_{err}	arrival time error
τ_n	receive delay at channel n
ϕ	arbitrary phase factor
φ_{err}	phase error of the receive data
ϕ_{rot}	phase rotation

TABLE OF CONTENTS

LIST OF FIGURES

XII

XIV

LIST OF TABLES

CHAPTER 1 INTRODUCTION

1.1 ULTRASONIC ARRAY SYSTEM

Ultrasound, because of its noninvasiveness and cost-effectiveness, is often the preferred imaging modality. Diagnostic ultrasound continues to evolve by improving in convenience, ease of use, portability, diagnostic capability, and image quality. Over the years, ultrasound has adapted to new applications through new arrays suited to specific clinical purposes and to signal processing. Also, a variety of transducer types have been invented and adapted to specific clinical usage (Fig. 1-1). New functionalities and features from the new arrays and signal processing techniques provide many opportunities to solve relevant and interesting problem.

Fig. 1-1. A variety of (a) ultrasound array systems and (b) array transducers (from the website: http://www.gehealthcare.com/).

In a typical medical ultrasound system (Fig. 1-2), the transmit beam former determines the delay pattern and pulse train that set the desired focal point. The outputs of the transmit beam former are then amplified by high-voltage transmit amplifiers to drive the transducer array. These amplifiers can be controlled by digital-to-analog converters to shape the transmit pulses. Multiple transmit focal regions are typically used to extend the field of view by ameliorating the attenuation

associated with propagation through tissues. On receive, the transmit/receive switch blocks the high-voltage transmit pulses, allowing the receive signals to be amplified using low-noise amplifiers. In receive beam forming, radio frequency (RF) signals are acquired from multiple channels of the transducer array and geometrical delays are applied to each channel to focus the signal at a certain range. The channels are then summed across the aperture domain prior to B-mode image processing, color Doppler, or spectral Doppler. Finally, the processed data are scan-converted for video display.
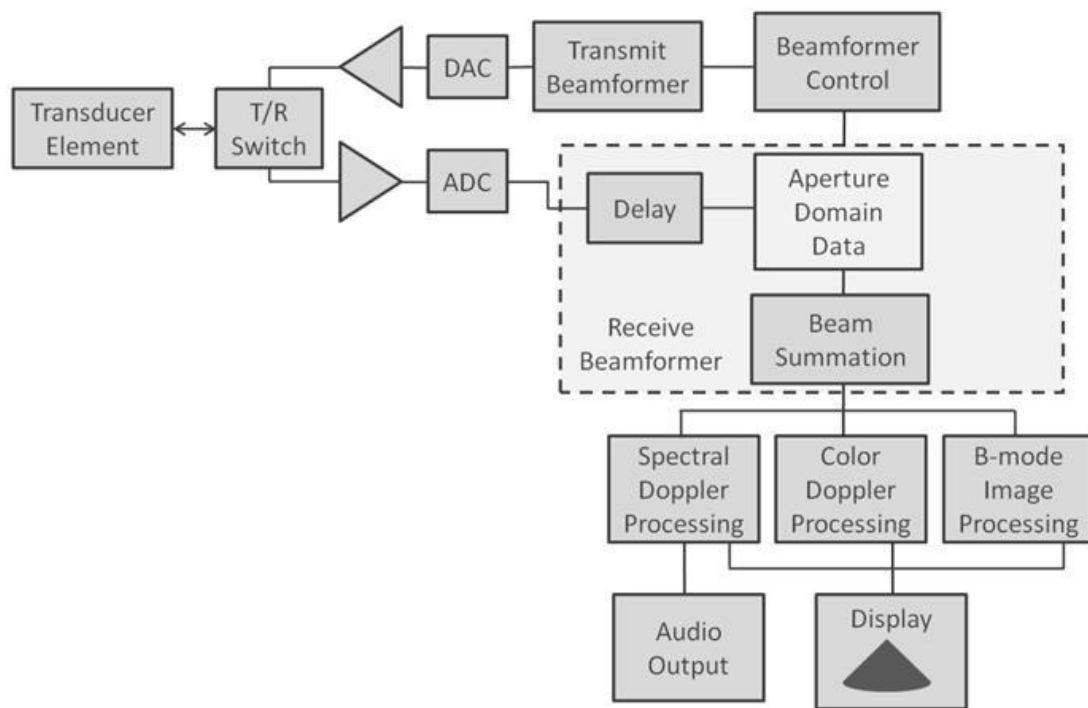
Fig. 1-2. Schematic diagram of a medical ultrasound system.

1.2 BEAM FORMATION AND APERTURE DOMAIN PROCESSING

Beam formation is an aperture domain data processing algorithm that is used to control the directionality of the reception or transmission of a signal on a transducer array [1]. The beam is controlled by beam control methods, such as dynamic aperture, dynamic focusing and apodization. Beam forming techniques direct the majority of

signal energy from a group of transducer in a chosen angular direction. The most prevalent beam forming method is the delay-and-sum method [2]. This method forms an ultrasonic beam with a linear phased array by properly delaying the transmit and receive signals. Since the spherical wave propagation in the near field region should be considered, both steering and focusing delays are required in the delay-and-sum technique for ultrasound beam forming.
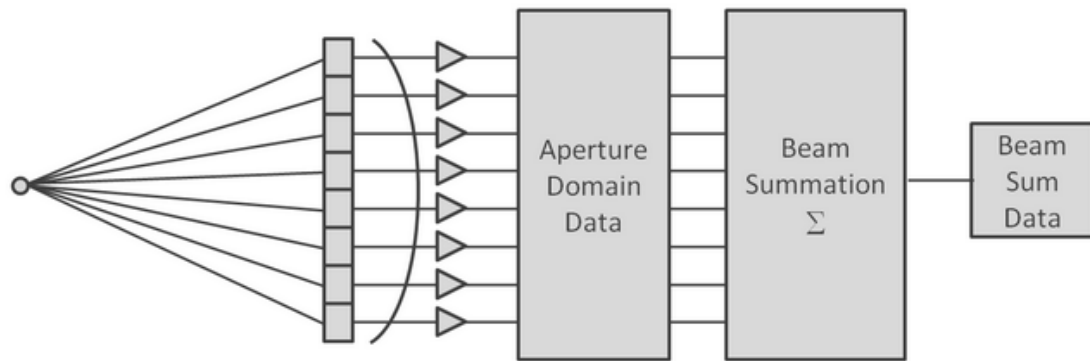
Fig. 1-3. Schematic diagram of receive beam formation

An ultrasound receive beam former is schematically shown in Fig. 1-3. Typically, the receive channel data can be expressed as:

$$r_n(t) = A_n(t) \exp(-j2\pi f_0(t) + \varphi), \qquad (1\text{-}1)$$

where A is the envelope of the receive signal from channel n, f_0 is the center frequency of the emitted signal, φ is an arbitrary phase factor that depends on the depth, and t is the arrival time of the receive signal. The aperture domain data are obtained after applying the geometrical delays but prior to beam summation, that is:

$$x_n(t) = r_n(t + \tau_n) = A_n(t + \tau_n) \exp(-j2\pi f_0(t + \tau_n) + \varphi), \qquad (1\text{-}2)$$

3
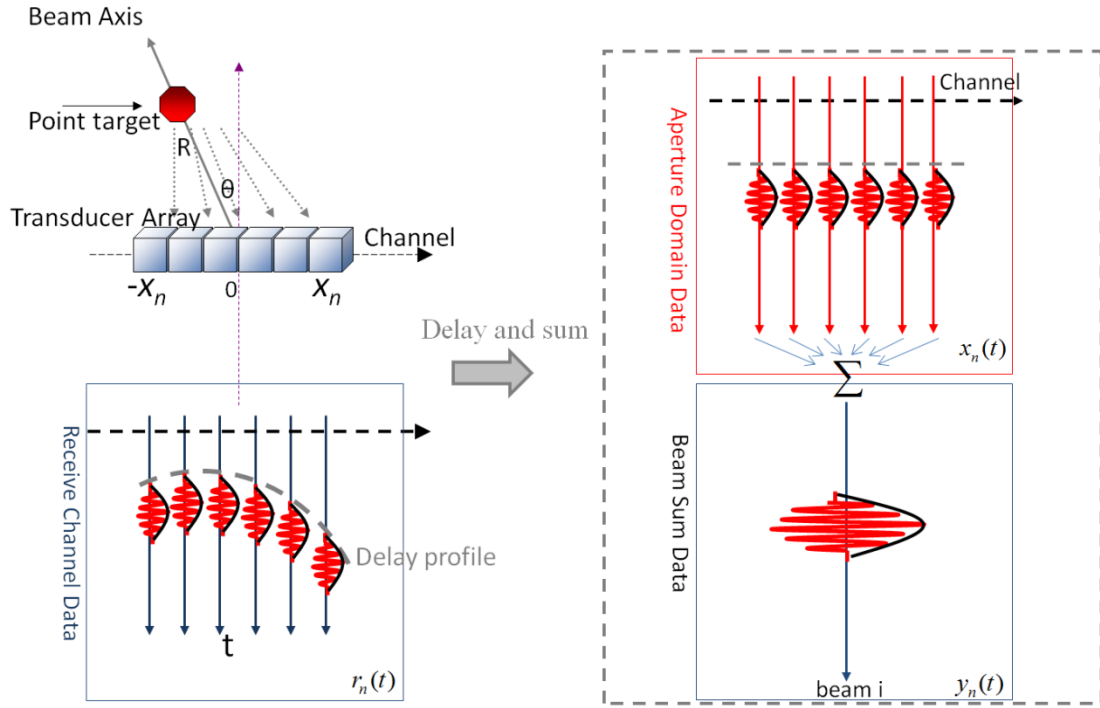
Fig. 1-4. An illustration of a conventional beam forming processing.

where τ_n is the receive delay at channel n. Finally, beam sum data are the sum of the

aperture domain data across the array:

$$y(t) = \sum_{n=1}^{N} x_n(t). \qquad (1\text{-}3)$$

where N is the total number of elements. Typically, the applied delay at each channel

τ_n can be formulated as:

$$\tau_n \cong \frac{2R}{c} - \frac{\sin\theta}{c} X_n + \frac{\cos^2\theta}{2Rc} X_n^2. \qquad (1\text{-}4)$$

where R is the range from the focal point to the center of the transducer, c is the sound

velocity, θ is the beam steering angle, and X_n is the channel position along the array

direction (X). Fig. 1-4 illustrates the relationship among the $r_n(t)$, $x_n(t)$, and $y(t)$. Since

each element itself has a broader radiation pattern (i.e., is associated with more spatial

4

information) than the entire aperture, the aperture domain data provide more information than the beam-sum data. However, the data rate of aperture domain data (e.g., typically several GB/sec for a real-time 128-channel system) makes it technically difficult to transfer and to store them in real time, and so a conventional ultrasound system discards these data after beam summation. The use of aperture domain processing techniques to extract the hidden spatial information such as directional flow or to improve the imaging quality is of great interest. Moreover, the increasing capabilities of high-performance digital electronic devices have enabled implementation of new aperture domain processing techniques for digital ultrasound systems, which have been extensively studied to improve the performance in adaptive imaging [3-17], vector flow estimation [18-20], limited-angle tomography [21, 22], and coded excitation [23].

1.3 LIMITATIONS OF BEAM SUM DATA

Most ultrasound systems discard aperture domain data after the processing of beam summation due to the large amount of data size. Although the data size is less to use the beam sum data than to use the aperture domain data, the beam sum data also contain less spatial information than the aperture domain data. The state-of-the-art aperture domain processing techniques utilize this hidden information and enable the study to improve the accuracy of flow estimation or to improve the imaging quality.

1.3.1 Issues of Flow Estimation

Determining the true blood flow velocity is important in medical ultrasound for diagnosing various diseases and traumas [18, 19, 24-32]. Current commercial ultrasound imaging systems utilize conventional color Doppler techniques. The estimated blood velocities are visualized in a color image that is superimposed on a B-mode image. Such images that combine information on the blood flow and tissue structure have been extensively used for studying blood flow in the human body. The conventional method, however, can only estimate the axial velocity component of the

blood flow (i.e., the velocity component parallel to the axis of the stimulating beam) [24]. The inability to estimate nonaxial velocity components results in underestimation of the vector velocity, and is a fundamental limitation to quantitatively estimating blood flow.

Conventional flow estimation techniques use autocorrelation technique to estimate the arrival time difference resulting from the flow motion. The autocorrelation function is formulated as:

$$R(t) = \frac{1}{M-1} \sum_{i=1}^{M-1} y(i) \cdot y^*(i+1), \qquad (1\text{-}5)$$

where the $R(t)$ is the auto-correlation function, i is the i-th firing out of M firings. Then the arrival time difference can be estimated using the phase of the auto-correlation function [24], as:

$$\Delta\tau = \frac{\Delta\varphi}{2\pi f_0} = \frac{\arctan(\frac{\mathrm{Im}(R(t))}{\mathrm{Re}(R(t))})}{2\pi f_c}, \qquad (1\text{-}6)$$

where $\Delta\varphi$ is the phase of the $R(t)$. Finally, the flow velocity can be estimate as:

$$v = \frac{\Delta\tau \cdot c}{\mathrm{PRI}}, \qquad (1\text{-}7)$$

where PRI denotes the pulse repetition interval. This phase-shift or time-shift estimation technique for blood flow estimation is extensively used in the conventional system. Conventional systems utilize this technique to estimate the flow velocity along the beam direction and maps the estimated velocities using red and blue colors to indicate the flow is toward and away the transducer, respectively. This real-time flow velocity visualization technique is also known as the color Doppler technique (Fig. 1-5). However, the conventional technique can only estimate the arrival time difference for the motion along the beam axis (i.e., axial velocity). This results in

estimation errors of the flow velocity. To estimate the true flow velocity the flow component transverse to the beam axis (i.e., lateral velocity) should also be estimated.
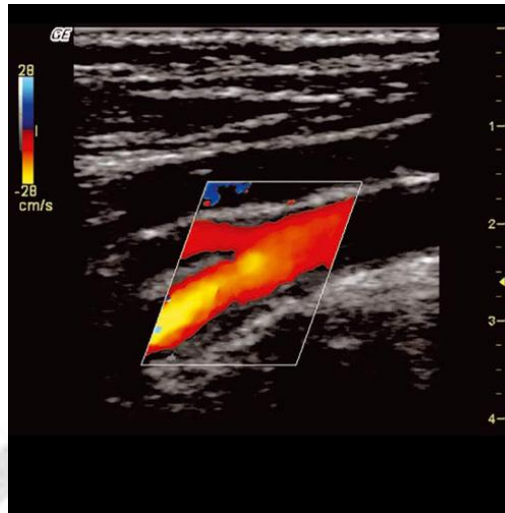
Fig. 1-5 Flow estimation within internal carotid artery using color Doppler technique (from the website: http://www.gehealthcare.com/).

Figs. 1-6 and 1-7 illustrate the effects of a point-like target with an axial motion and a lateral motion, respectively. The top panels of Figs. 1-6 and 1-7 illustrate that a point target is moving along the beam axis (i.e., axial motion) and is moving transverse to the beam axis (i.e., lateral motion), respectively. The bottom panels of Figs. 1-6 and 1-7 illustrate the corresponding aperture domain data and the beam sum data. Fig. 1-6 shows that an axial-motion results in time-shifts in both aperture domain data and beam sum data. Furthermore, the time-shifts for the aperture domain data are identical at all receive channels. Therefore, axial velocity estimation can be further improved using the mean estimated velocity with multiple estimations from all array elements. Fig. 1-7, on the other hand, shows that only aperture domain data can estimate the laterally moving target. The beam sum data are not influenced by a lateral motion of the target and cannot be used for lateral velocity estimation. For aperture domain data, the arrival time differences are tilt shifts along the array direction. The lateral velocity can be estimated using the tilt slope of the arrival time differences across the array. Therefore, aperture domain data are of particular interests in the flow estimation studies.
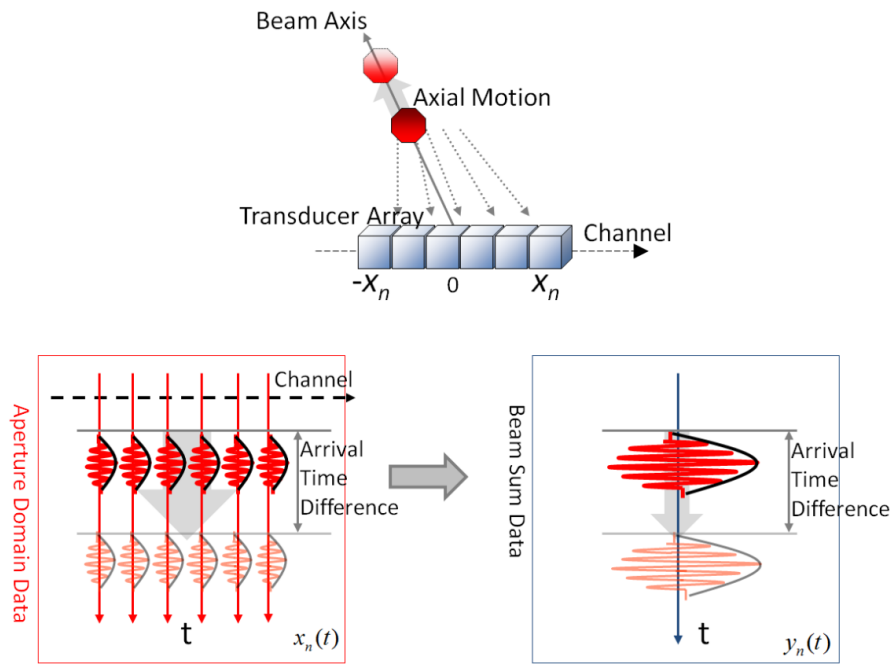
Fig. 1-6. Illustration of the relationship between the aperture domain data and beam sum data for a point-like target with an axial motion.
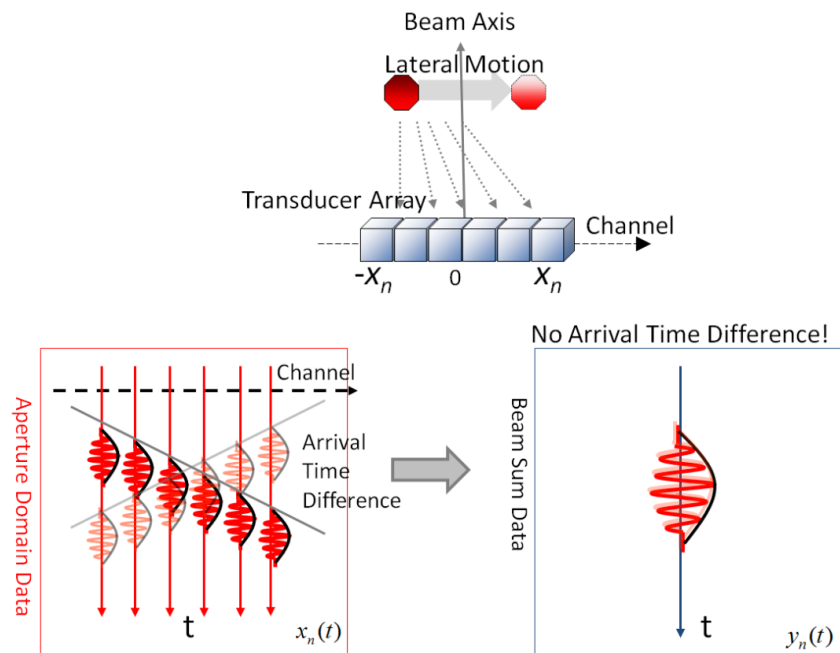
Fig. 1-7 . Illustration of the relationship between the aperture domain data and beam sum data for a point-like target with a lateral motion.

1.3.2 Issues of Phase Aberration

A practical limitation of medical ultrasound is the focusing errors introduced by sound-velocity inhomogeneities in the human body. Because the sound velocity varies over a wide range (e.g., 1450 m/s in fat and 1665 m/s in collagen [33]), the use of a constant sound velocity to calculate focusing delays inevitably results in focusing errors. Therefore, the delay calculation of the conventional beam forming is not generally correct for imaging the human body. Such focusing errors are also termed phase aberrations, and they degrade both the spatial resolution and the contrast in the obtained images.
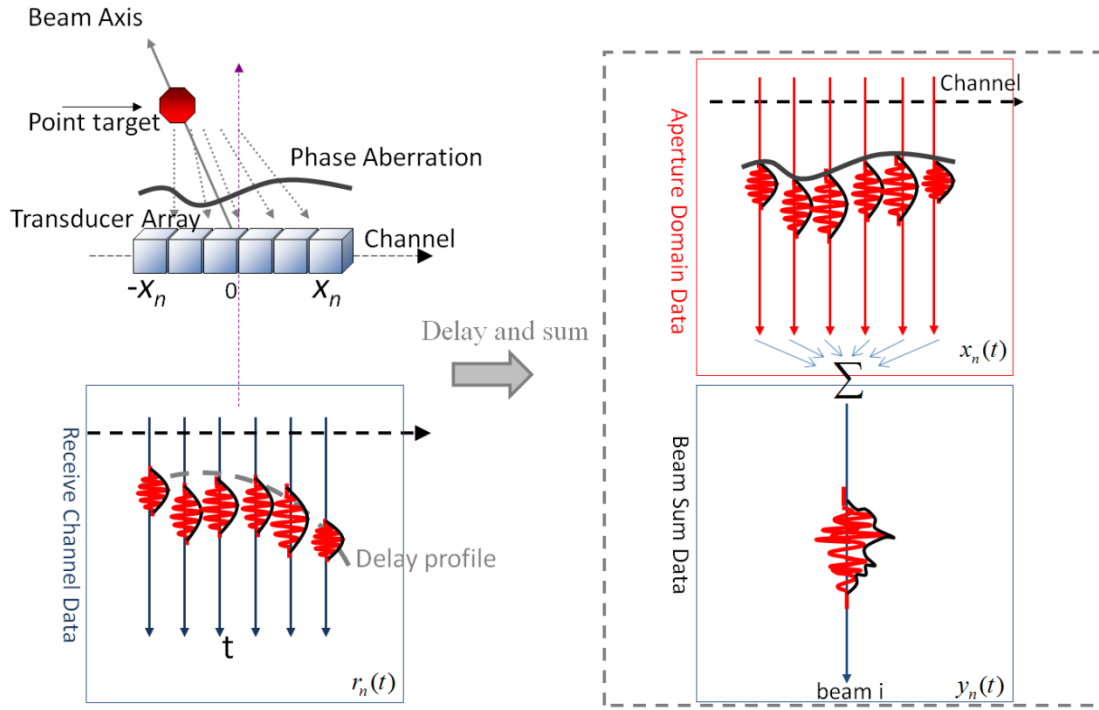
Fig. 1-8. Illustration of the effects resulted from phase aberration including time delay errors, energy level fluctuations, and waveform distortions.

As illustrated in Fig. 1-8, the aperture domain data are degraded due to time delay errors, energy level fluctuations, and waveform distortions. In case of phase aberration, the aperture domain data are expressed as:

$$x_n(t) = B_n \cdot x_n(t + \tau_{err}) = B_n \cdot A(t + \tau_n + \tau_{err}) \exp(j2\pi f_0(t + \tau_n) + \varphi + \varphi_{err}) , \qquad (1\text{-}8)$$

where B_n is the energy level fluctuation factor, and τ_{err} is the arrival time error, and

φ_{err} is the phase error of the receive data and $\varphi_{err} = \tau_{err} / 2\pi f_0$. The effect of phase aberration cannot be directly corrected from the beam sum data $y(t)$. Therefore, aperture domain processing technique is a must for phase aberration correction. Fig. 1.9 shows an example that the imaging quality in female breast is improved by the adaptive imaging technique. The breast tissue is technically difficult to image, since the speed of sound varies in different types of tissues. Adaptive imaging method corrects the phase aberration, and thus improving contrast resolution, and boundary definition. The results are better detection of the lesion characteristics to increase diagnostic confidence. Following sections will introduce the prior arts of aperture domain processing techniques including vector flow estimation and phase aberration correction.
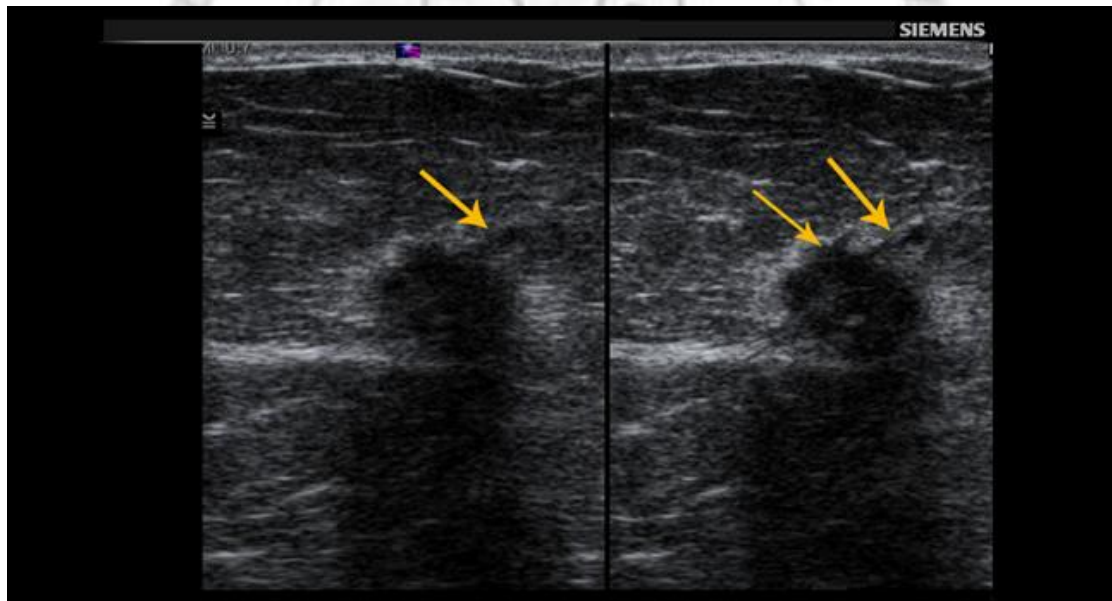
Fig. 1-9. An example of adaptive breast imaging. The left and right images show the results of conventional imaging and adaptive imaging. The adaptive imaging method improves lesion detectability and with calcifications (pointed using arrows) being better presented (from the website: http://www.medical.siemens.com).

1.3.3 Issues of High Frame Rate Adaptive Imaging

Ultrasound imaging is extensively used in clinics due to its real-time capabilities, noninvasiveness, safety, and cost effectiveness. Typically fixed focusing is applied on transmit and dynamic focusing is applied on receive. Frame rates of tens of frames per second can be achieved in most diagnostic applications, but this limits applications such as the imaging of heart motion [34] and measurements of shear-wave propagation [35] where frame rates greater than 100 frames/sec are desirable.

The round-trip propagation time physically limits the imaging frame rate, and so reducing the number of firings is necessary to increase the frame rate. Existing high frame rate (HFR) imaging methods use broad transmit beams to decrease number of firings [36-38]. A broad transmit beam can be formed using plane-wave excitation (i.e., an unfocused transmit beam) [39], a defocused beam [40], or a limited-diffraction beam [41, 42]. In this case the insonifying energy is more distributed than a focused beam, allowing the simultaneous formation of parallel receive beams. Although the frame rate can be increased using broad transmit beams, such beams result in a low signal-to-noise ratio (SNR) and image quality [43]. Furthermore, the image quality of an HFR system is degraded particularly when adaptive imaging methods are applied.

1.4 VECTOR VELOCITY ESTIMATION TECHNIQUES

1.4.1 Multibeam Methods

Several techniques have been proposed for obtaining the velocity vector of blood flow, of which one is the multibeam method [25, 26]. The flow velocity axial components are estimated along individual beams that are formed using either multiple transducers or multiple subapertures that are electronically divided from a single transducer array. The flow velocity vectors are estimated along each beam, with the vector velocity then reconstructed and estimated using the geometric relationship of these beams. However, such systems are complex due to the

requirement for confocal, nonparallel transmit beams. Moreover, the angle between the beams needs to be large enough to produce an acceptably low estimation variance, with the resulting large aperture size limiting the clinical applicability.

1.4.2 Speckle Tracking Methods

Another technique is the speckle tracking method [27, 28], which is based on the assumption that speckle translation closely reflects target translation at small displacements. The 2-D velocity vector can be estimated by tracking the motion of speckle patterns between consecutive B-mode images. This method for estimating the blood flow velocity is feasible provided that no significant speckle decorrelation occurs during the data acquisition time, and hence large amounts of data must be acquired. Furthermore, this method is less suitable for real-time estimation since it is computationally demanding.

1.4.3 Transit-time Spectral Broadening Methods

Another approach is based on the transit-time spectral broadening effect [29-32]. This method utilizes the property that the Doppler bandwidth of echo signals is inversely proportional to the transit time of a scatterer crossing the sample volume of an ultrasound beam; the linear relationship between the Doppler bandwidth and the lateral velocity component enables 2-D velocity estimation. However, the bandwidth estimation tends to be influenced by system noise and the presence of speckle-generating scatterers in the blood, and so achieving an adequate spectral resolution requires a long data acquisition time.

1.4.4 Spatial Quadrature Methods

One Aperture domain-data-based flow estimation method is spatial quadrature [18, 19]. To find the motion transverse to the ultrasound beam, the beam pattern is laterally modulated by aperture apodization or a transmit focusing technique. This allows phase shifts across the aperture and allows the lateral motion of the blood flow can be estimated. Quadrature receive apodizations including an even and an odd

12

apodization function can be used to weight the aperture domain data to generate laterally modulated echoes y_{even} and y_{odd}. The axial and lateral motions can be estimated by applying heterodyning functions to remove the interaction between the axial and lateral velocity components:

$$
\begin{aligned}
\text{het}_{axial} &= (y_{even} + jy_{odd}) \times (y_{even} - jy_{odd})^*, \\
\text{het}_{lateral} &= (y_{even} + jy_{odd}) \times (y_{even} - jy_{odd}).
\end{aligned}
\tag{1-9}
$$

The phase shifts of het_{axial} and $\text{het}_{lateral}$ are only related to the axial and lateral velocity components, respectively. For scatterers that move across the modulated beam over an ensemble time period, the axial and lateral velocity can be estimated as axial and lateral phase shifts ($d\phi_{axial}$ and $d\phi_{lateral}$):

$$
\begin{aligned}
v_{lateral} &= \frac{d\phi_{lateral}}{2\pi 2 \ \text{PRI} \ k_{lateral}}, \\
v_{axial} &= \frac{d\phi_{axial} c}{2\pi 4 \ \text{PRI} \ f_0}.
\end{aligned}
\tag{1-10}
$$

where $k_{lateral}$ is the wave number used in the lateral apodization function, and $d\phi_{axial}$

and $d\phi_{lateral}$ are the estimated phase shifts of het_{axial} and $\text{het}_{lateral}$, respectively. This method, however, using aperture appodiation degrades the lateral sensitivity, and the axial-lateral inter-modulation degrades the estimation accuracy in the presence of both axial and lateral velocity components

1.5 ADAPTIVE IMAGING TECHNIQUES

1.5.1 Correlation-based Methods

The adaptive imaging technique first proposed by Flax and O'Donnell [3, 4] can correct errors in beam formation resulting from sound-velocity inhomogeneities. This is a correlation-based method that models sound-velocity inhomogeneities as a

near-field phase screen, thereby assuming that time-delay errors produce phase aberrations only at the surface of the transducer and can thus be estimated by finding the peak of the cross-correlation function of the signals from adjacent channels [3, 4] defined as

$$C_n(t) = \frac{1}{T}\int_0^T x_n(t)x_{n+1}(t+\tau)\mathrm{d}\tau,\qquad(1\text{-}11)$$

where T is the correlation duration, and x_n and x_{n+1} are the receive-aperture domain data at channels n and $n+1$, respectively. At each channel, the differential time delay between the n-th and $n+1$-th channels is given by

$$\Delta t_n = \max_{\Delta t_n} C_n(\Delta t_n).\qquad(1\text{-}12)$$

The unwrapped time delays across the aperture are estimated as

$$\Delta T_n = \sum_{i=1}^N \Delta t_i.\qquad(1\text{-}13)$$

After estimating time-delay errors, phase aberrations can be corrected by appropriately adjusting for focusing errors. Besides the signal from the adjacent channel, the beam sum [5] or partial beam sum [6] is an alternative reference signal for estimating arrival-time errors.

The near-field phase-screen model is inadequate in practice since sound-velocity inhomogeneities result in not only time-delay errors but also energy-level fluctuations and waveform distortion. This led to a proposed displaced-phase-screen model that assumes that phase aberrations can be modeled as a phase screen at some distance from the transducer surface [7]. Nevertheless, correlation-based methods remain largely inadequate due to aberration integration errors induced by 3D sound-velocity inhomogeneities [8]. Removing the effects of such errors in time-delay estimation requires the use of a 1.5D or 2D array [8, 44]. Furthermore, the performance of these

14

methods in ultrasonic breast imaging remains inadequate due to the wide spatial variations in the sound velocity in breast tissue.

1.5.2 Adaptive Sidelobe-reduction Methods

Another approach for correcting phase aberrations is to adaptively reduce sidelobes [9-17], which are elevated by focusing errors. In the parallel adaptive receive-compensation algorithm (PARCA) [9-12], unwanted sidelobe contributions are removed whilst maintaining the mainlobe signal intensity by removing the off-axis component from the receive signals after constructing multiple receive beams in each transmit direction. The method uses a total-least-squares model to minimize focusing imperfections from scatterers. However, the main drawback of the PARCA is that it is computationally demanding.

1.5.3 Coherence-based Methods

Another adaptive sidelobe-reduction method is based on the use of the coherence factor (CF) of the receive-channel data [13-15], which represents a focusing-quality index:

$$\text{CF}(t) = \frac{\text{coherent energy}}{\text{total incoherent energy}} = \frac{\left|\sum_{n=1}^{N} x_n(t)\right|^2}{\sum_{n=1}^{N} |x_n(t)|^2} = \frac{y(t)^2}{\sum_{n=1}^{N} |x_n(t)|^2}. \tag{1-14}$$

The CF weighting processing can be expressed as

$$y_{weighted}(\text{t}) = \text{CF}(t) \cdot y(t), \tag{1-15}$$

where $y_{weighted}$ denotes the amplitude of the beam sum weighted by the CF. In other words, the CF is defined as the ratio between the energy of the coherent sum to the total incoherent energy (i.e., N times the incoherent sum). Therefore, an image point with a high CF value possesses good focusing quality and its amplitude should be

maintained, whereas the amplitude of an image point with a low CF value possesses poor focusing quality and its amplitude should be suppressed. Thus, this method is effectively an adaptive weighting technique in which the amplitude of each image pixel is weighted by the corresponding CF such that the unwanted sidelobes are effectively reduced. The CF has also been modified to the generalized CF (GCF) to accommodate the coherence properties of speckle-generating objects [16]. The efficacy of the GCF-weighting method has been demonstrated for phantom data [16]. Continuing study is to test the feasibility of applying the GCF to clinical breast data. Specifically, the method will be applied to different types of breast lesions: cyst, fibroadenoma, carcinoma, and abscess. Also the potential of coherence-based method for high frame rate imaging will be investigated.

1.6 SCOPE AND DISSERTATION ORGANIZATION

The functionalities of ultrasound array systems have been limited since only the beam sum data are used for signal processing. Regarding the system complexity for the array system, it is more preferable to use the beam sum data than the aperture domain data. However, only a small fraction of valuable spatial information is recorded by the beam sum data. The purpose of this thesis is to develop aperture domain processing techniques to improve accuracy of blood flow estimation and to improve the image qualities in the presence of phase aberration. Specifically, a flow estimation technique based on the arrival time difference of each array element is developed. Also, two sidelobe-reduction-based adaptive imaging techniques are developed to correct image quality degradation resulted from sound velocity inhomogeneities within the human body.

The dissertation is organized as follows. In Chapter 2, a proposed vector velocity estimator using aperture domain data is presented. The conventional velocity estimator and the principles of the proposed method are investigated. The performance of the proposed method is discussed theoretically. Simulation and real

16

ultrasound data are used to evaluate efficacy of the proposed technique. The proposed technique is also compared with conventional vector velocity estimation method.

Chapter 3 explores the contrast and other general characteristics of the coherence-based adaptive imaging technique-generalized coherence factor (GCF). The basic principles and experimental methods for the GCF-weighting method are described. Clinical breast data are used to verify the efficacy of the method. The experimental results are also performed with a correlation-based method as a comparison. The results are also discussed.

In Chapter 4, a coherence-based adaptive imaging method for high frame rate imaging is proposed. This method utilizes a high accuracy angle-of arrival estimator, namely Capon estimator, to estimate the coherent energy for high frame rate imaging. The basic principles of high frame rate imaging and the proposed method are described. Simulations and clinical experiments are performed to investigate the proposed method. The adaptive imaging method for high frame rate imaging and conventional imaging are also discussed. This dissertation concludes in chapter 5. Future works are also described.

CHAPTER 2 BLOOD VELOCITY VECTOR ESTIMATION

Most conventional blood flow estimation methods only measure the axial component of the blood velocity vector. In this chapter, we developed a new method for 2-D velocity vector estimation in which time shifts resulting from blood motion are calculated for the individual channels using aperture domain data. This allows the construction of a time-shift profile along the array direction as a function of channel index, which is approximated by a first-order polynomial whose zeroth-order and first-order terms can be used to determine the axial and lateral velocity components, respectively. The efficacy of the proposed method was verified by simulations and experiments in which the transducer array had 64 elements and a center frequency of 5 MHz. In Section 2.1, the principles of the proposed method is described. The performance of the proposed method is discussed in Section 2.2, and the simulation results and the experimental results are presented in Section 2.3 and 2.4 respectively. The discussion and conclusions are given in Section 2.5.

2.1 VECTOR VELOCITY ESTIMATION

2.1.1 Basic Principles of Vector Flow Estimation

The arrival time of a blood flow echo signal generated by a pulse of ultrasound is controlled by the spatial positions of the red blood cells in the sample volume. As shown in Fig. 2-1, using the parabolic approximation [45], the arrival time (τ) of a target source positioned at $p_0 = (R_0, \theta_0)$ for an array element positioned at x_n relative to the center of the array is
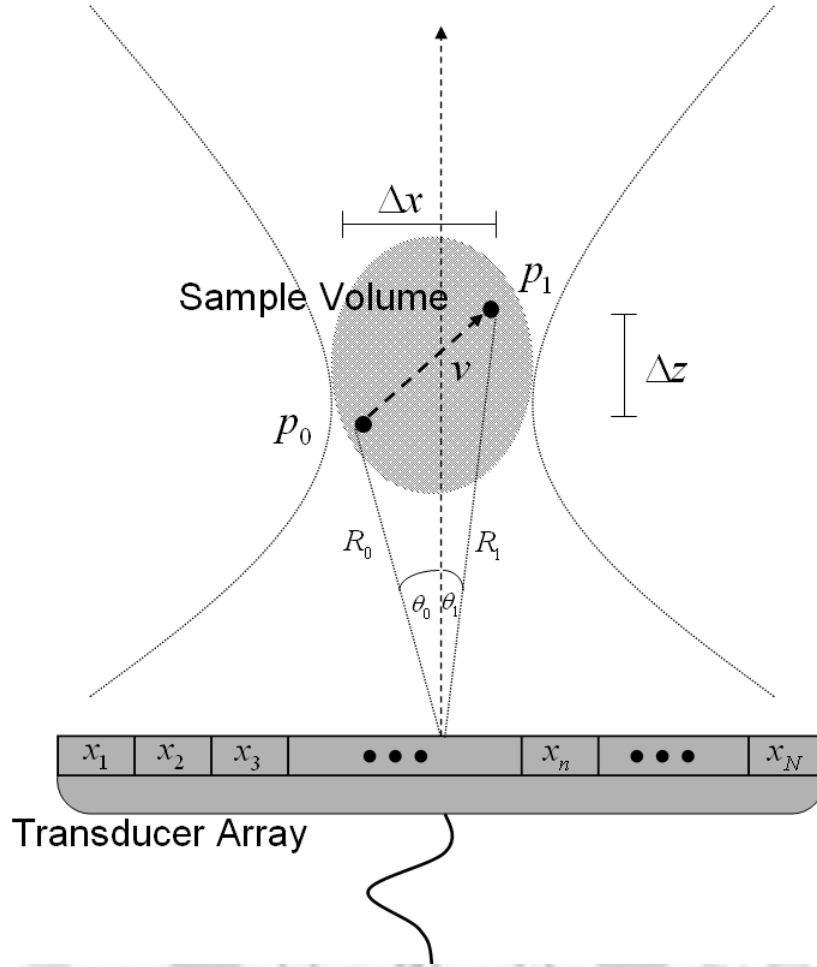
Fig. 2-1. Schematic diagram of the displacement of a point target.

$$\tau(X_n, R_0, \theta_0) \approx 2\frac{R_0}{c} - \frac{X_n}{c}\sin\theta_0 + \frac{X_n^2\cos^2\theta_0}{2R_0 c}, \qquad (2\text{-}1)$$

where the sample volume is determined by an *N*-element transducer array at a range R, and c is the sound velocity in the tissue. At the second firing, the target source position has moved from p_0 to $p_1 = (R_1, \theta_1)$, for which the corresponding arrival time is

$$\tau(X_n, R_1, \theta_1) \approx 2\frac{R_1}{c} - \frac{X_n}{c}\sin\theta_1 + \frac{X_n^2\cos^2\theta_1}{2R_1 c}. \qquad (2\text{-}2)$$

The time shift caused by the target displacement is referred to as the arrival-time difference. Assuming that the displacement is small enough such that the difference in the focusing term can be ignored, the time shift is

$$
\begin{aligned}
\Delta\tau(x_n) &= \tau(X_n,R_1,\theta_1) - \tau(X_n,R_0,\theta_0) \\
&\approx 2\frac{R_1-R_0}{c} - \frac{X_n}{Rc}(R\sin\theta_1 - R\sin\theta_0) \\
&= 2\frac{\Delta R}{c} - \frac{X_n}{Rc}(X_1-X_0),
\end{aligned}
\tag{2-3}
$$

where X_1 and X_0 are the spatial positions of the target sources on the x-axis, ΔR denotes the difference in the range of the sources, and R is the range of interest. In the Fresnel region ($Z^2 \gg (X_n-X)^2$, where $Z = R\cos\theta$), ΔR can be further approximated as ΔZ. Thus,

$$
\Delta\tau \approx 2\frac{\Delta Z}{c} - \frac{\Delta Z}{Rc}X_n,
\tag{2-4}
$$

where $\Delta X = X_1 - X_0$. The first term in this time shift $(2\Delta Z/c)$ is related to the axial velocity component because

$$
\Delta Z = v_{axial} \cdot \mathbf{PRI},
\tag{2-5}
$$

where v_{axial} denotes the axial velocity component and PRI denotes the pulse repetition interval. The second term in (2-4) $((\Delta X/Rc)X_n)$ is related to the lateral velocity component according to

$$
\Delta X = v_{lateral} \cdot \mathbf{PRI}.
\tag{2-6}
$$

Combining (2-4), (2-5), and (2-6) yields

21

$$\Delta\tau(X_n) = 2\frac{v_{axial} \cdot \mathbf{PRI}}{c} + \frac{v_{lateral} \cdot \mathbf{PRI}}{Rc}X_n$$

$$\equiv a_0 + a_1 X_n.$$

(2-7)

This time shift is a first-order polynomial in x_n with zeroth- and first-order coefficients of a_0 and a_1, respectively, which can be used to estimate the axial and lateral velocity components, respectively.

In the proposed method, the time shifts of the aperture domain data are derived from the autocorrelation function. The main difference between the proposed and conventional methods is that in the former the autocorrelation processing is applied before beam summation.

2.2.2 Auto-Correlation Based Method

For a target moving with a constant velocity, which results in a constant arrival-time shift between each firing, the baseband received signal for an element located at X_n at time i is given by

$$r(i, X_n) = A(i \cdot \Delta\tau(X_n))\exp(j2\pi f_0 i \cdot \Delta\tau(X_n) + \varphi),$$

(2-8)

where A is the envelope of r, f_0 is the center frequency of the emitted signal, i is the pulse index, and ϕ is an arbitrary phase factor that depends on the depth. The discrete first-lag autocorrelation of aperture domain data is

$$R(i, X_n) = \frac{1}{M-1}\sum_{i=1}^{M-1} r(i, X_n) \cdot r^*(i+1, X_n),$$

(2-9)

where * denotes the complex conjugate and M is the number of firings, which is used for slow-time temporal averaging. The phase of $R(i, X_n)$ equals the phase difference of two consecutive echoes:

22

$$\Delta\varphi(i, X_n) = \arctan(\frac{\text{Im}(R(i, X_n))}{\text{Re}(R(i, X_n))}) \, , \qquad (2\text{-}10)$$

and the time delay profile $\Delta\tau$ is constructed as

$$\Delta\tau(X_n) = \frac{\Delta\varphi(i, X_n)}{2\pi f_0} \, . \qquad (2\text{-}11)$$

By applying the first-order linear regression model using least-squares fitting to $\Delta\tau$, both a_0 and a_1 in (2-7) can be estimated and then used to calculate the axial and lateral velocities according to

$$\hat{v}_{axial} = \frac{a_0 \cdot c}{2PRI} \qquad (2\text{-}12)$$

and

$$\hat{v}_{lateral} = \frac{a_1 \cdot R \cdot c}{PRI} \, , \qquad (2\text{-}13)$$

respectively. The vector sum and phase angle of these two velocity components correspond to the estimated vector velocity

$$\hat{v} = \sqrt{\hat{v}_{axial}^{\,2} + \hat{v}_{lateral}^{\,2}} \qquad (2\text{-}14)$$

and the estimated Doppler angle

$$\hat{\theta}_{Doppler} = \arctan(\frac{\hat{v}_{lateral}}{\hat{v}_{axial}}) \, , \qquad (2\text{-}15)$$

respectively.
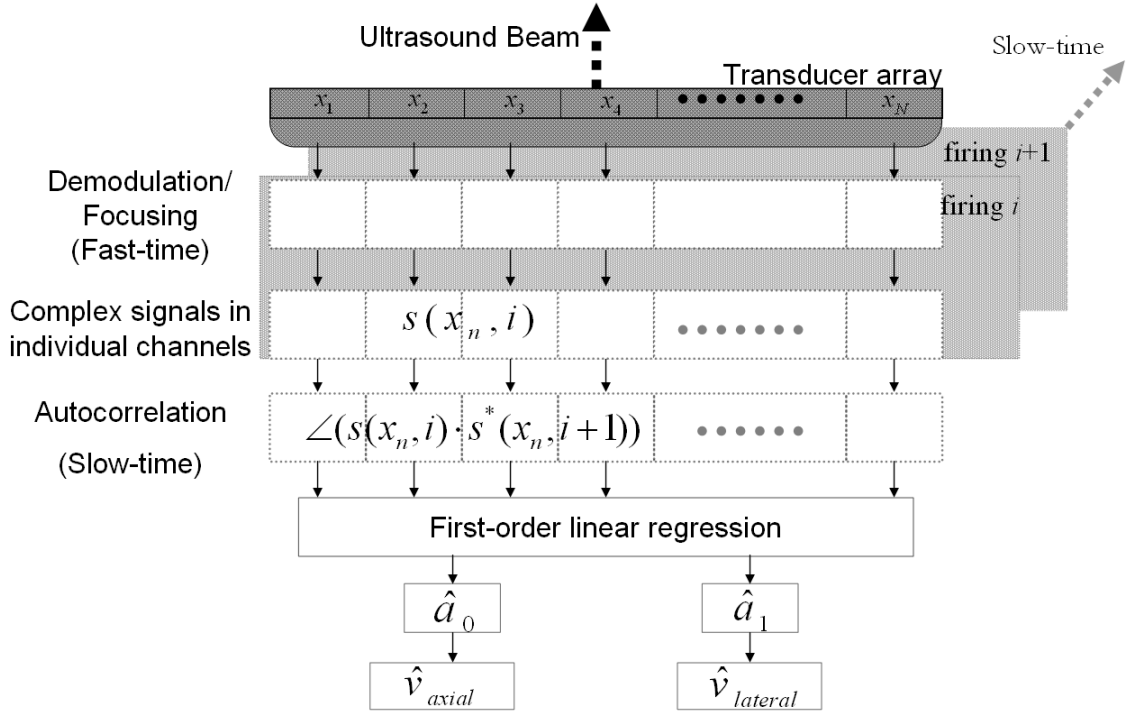
Fig. 2-2. Signal flow for the vector velocity estimator based on the processing of aperture domain data.

The signal processing in the proposed technique is shown schematically in Fig. 2-2. After the echo signal is received and digitized by the A/D converter, the received RF data are demodulated down to baseband. The baseband beam former applies the appropriate dynamic receive delays and phase rotations to the baseband data, and then the autocorrelation functions of the aperture domain data for different firings are calculated for all channels. First-order linear regression is applied to the estimated phases of the autocorrelation functions as a function of channel index, with the axial and lateral velocities then estimated based on the zeroth- and first-order coefficients, respectively. Both the estimated vector velocity and the estimated Doppler angle can subsequently be obtained using (2-14) and (2-15), respectively.

2.2 ESTIMATION ERROR ANALYSIS

2.2.1 Axial Velocity Estimation

The measurement errors of $\Delta\tau$ corresponding to different channels are assumed to be independently and identically distributed with a zero mean and a standard deviation (SD) of σ. The Cramér-Rao lower bound (CRLB) [46] of the SD is

$$\sigma \geq \sqrt{\frac{3}{2f_0^{\,3}\pi^2 T(B^3+12B)}(\frac{1}{\rho^2}(1+\frac{1}{\mathrm{SNR}^2})^2-1)}\,,\qquad (2\text{-}16)$$

where the SNR is for the channel, and the ρ is the correlation coefficient between the signals corresponding to two consecutive firings. For an N-channel system the variance of the zeroth-order term in the linear regression [47] (for x_n with a zero mean) is

$$Var(a_0)=[\frac{1}{N}+\frac{\overline{X}^2}{\sum_{n=1}^{N}(X_n-\overline{X})^2}]\sigma^2 \qquad (2\text{-}17)$$

$$=\frac{\sigma^2}{N}\bigg|_{\bar{x}=0}\,,$$

where $\overline{X}$ is the mean of X_n.

The SNR for the conventional method that uses N-channel beam-summation data is N times larger than that for a single channel. According to (2-16) and (2-17), the improvement ratio α defined as the ratio of the lower bounds of the SDs for the conventional and proposed methods is

$$\alpha = \sqrt{(\frac{1}{\rho^2}(1+\frac{1}{N \cdot \text{SNR}^2})^2 - 1)} \bigg/ \sqrt{\frac{(\frac{1}{\rho^2}(1+\frac{1}{\text{SNR}^2})^2 - 1)}{N}} \,. \tag{2-18}$$

The improvement ratio α as a function of the SNR for different correlation coefficients is shown in Fig. 2-3 for a system with 64 channels. The nominal correlation coefficient for blood flow estimation is typically 0.98 [48]. With $\rho = 0.98$, α is larger than 1 when SNR is higher than −1.93 dB. Fig. 2-3 shows that the improvement ratio α degrades as SNR decreases, and hence the conventional method is the better choice when the SNR is low. Since the SNR is related to the size of the aperture, this result indicates that using multiple small apertures may be inferior to the conventional method, which employs a single large aperture. Therefore, the subaperture size should be adaptively adjusted according to the SNR.
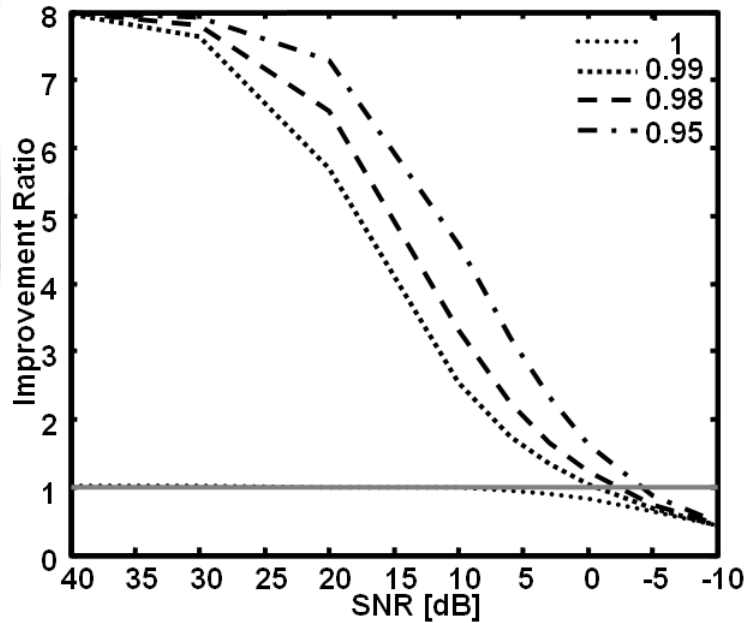
Fig. 2-3. Improvement ratio α as functions of the SNR for different correlation coefficients.

In our new approach, recursive subaperture processing using partial beam-summation signals at adjacent receive positions is employed to improve the performance when the SNR is low. This effectively produces new subaperture data

corresponding to a larger subaperture size, with the total number of channels being reduced. Fig. 2-4 shows the relations between the SNR and the optimal number of subapertures for different correlation coefficients. The optimal number of subapertures decreases as the SNR decreases, and hence the conventional method remains the preferred choice when the SNR is low.

2.2.2 Lateral Velocity Estimation

The variance of the estimated lateral velocity is proportional to the first-order coefficient (a_1) in (2-7). According to the first-order linear regression model [47], its variance is

$$Var(a_1) = \frac{\sigma^2}{\sum X_n^2}. \tag{2-19}$$

The ratio of the SDs of the estimated lateral and axial velocities according to (2-12), (2-13), (2-17), and (2-19) is defined as the lateral-to-axial estimation error ratio β:

$$\beta_{\textbf{proposed}} = \sqrt{\frac{Var(\hat{v}_{lateral})}{Var(\hat{v}_{axial})}} = 2R\sqrt{\frac{Var(a_1)}{Var(a_0)}}$$
$$= 2R\sqrt{\frac{N}{\sum X_n^2}} = \frac{4R}{pitch}\sqrt{\frac{3}{(N-1)(N+1)}}. \tag{2-20}$$

The value of β_{proposed} is 10.8 for a 64-element transducer array with a pitch of 0.3 mm and an R of 3 cm. For larger N, (2-20) can be approximated as

$$\beta_{\text{proposed}} \approx \frac{4\sqrt{3}R}{N \cdot pitch} = \frac{4\sqrt{3}R}{2a} = 4\sqrt{3}F\#, \tag{2-21}$$
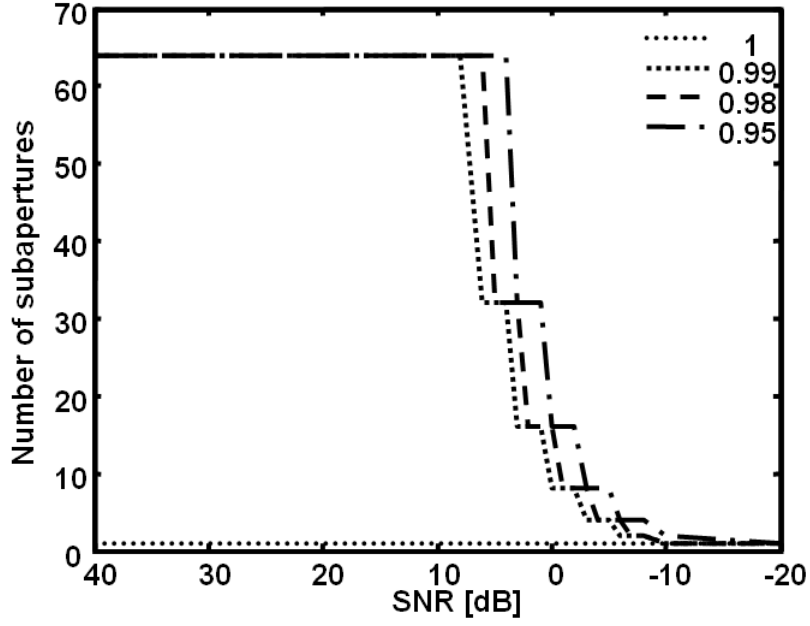
Fig. 2-4. Optimal number of subapertures as functions of the SNR for different correlation coefficients.

where $2a$ denotes the aperture size, and $F\#$ is the F-number defined as the ratio of the focal depth to the aperture size. That is, the error of the estimated lateral velocity component is proportional to the F-number. The ratio of the CRLBs [49] of the SDs of the axial and lateral velocities in the speckle tracking method becomes

$$\beta_{\text{speckle tracking}} = \frac{\sqrt{5}R}{2af_c\sigma_t}, \tag{2-22}$$

where σ_t is a constant defining the pulse length. The value of $\beta_{\text{speckle tracking}}$ is 10.2 for the parameters used in the present study.

28

2.3 SIMULATION INVESTIGATION

2.3.1 Simulation Methods

The proposed method was tested using simulation data generated by Field II [50]. In the simulations, the transducer comprised a 64-element linear array with a center frequency of 5 MHz and an aperture size of 19.2 mm. The sample volume was located at the focal point, which was 30 mm from the transducer. The corresponding pulse-echo -6 dB beam width and pulse witdh was 636 and 554 μm at the focal point. The sound velocity was 1500 m/s, the sampling frequency was 50 MHz, the pulse length was 1.37 μs, the pulse repetition frequency was 5 kHz, and white Gaussian noise was added to the received RF data to produce a SNR of 25 dB. Randomly generated scatterers were placed in the sample volume of the sound field in the x-z plane at a density of 100 scatterers/mm^2. These scatterers flowed at a constant velocity according to the predetermined Doppler angle and the displacement between two consecutive firings. All the echo signals were used for estimating the axial and lateral velocities according to (2-12) and (2-13), respectively, with the vector velocity and Doppler angle estimated using (2-14) and (2-15), respectively. The number of firings (M) was selected as a compromise between the data acquisition time and estimation errors. Fig. 2-5 shows the relations between the SD of the estimated vector velocity normalized by the ideal value (of 20 cm/s) and the number of firings for Doppler angles of 0°, 45°, and 90°. Based on these results, we decided to use 16 firings in this study.

2.3.2 Simulation Results

An illustration of a first-order linear regression processing using simulation data is shown in Fig. 2-6. The theoretical velocity and Doppler angle for the data are 30 cm/s and 45°, respectively, and hence both the axial and lateral velocity components are 21.2 cm/s. Both the estimated and fitted curves are shown in the figure with black and gray lines, respectively. The $\Delta\phi$ according to (2-10) is estimated as a function of
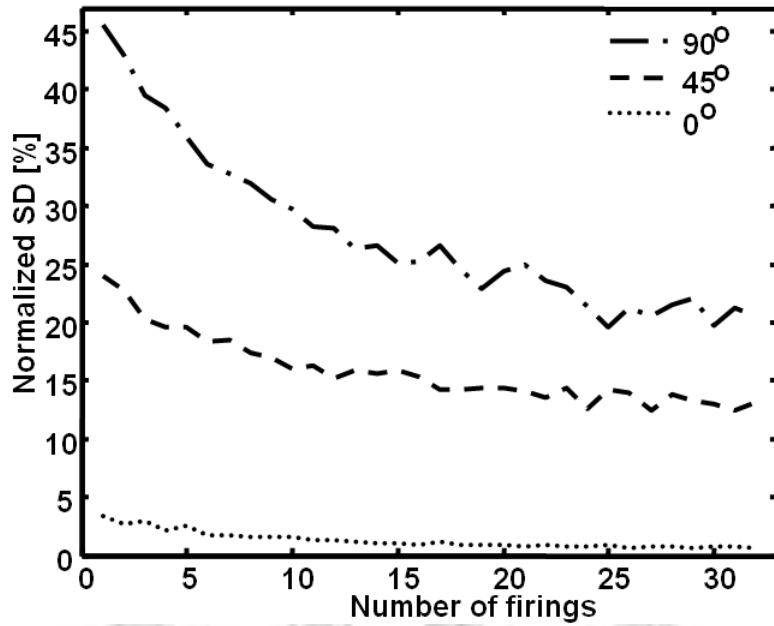
Fig. 2-5. Effect of the number of firings on the normalized SD for different Doppler angles. The vector velocity was 20 cm/s.

$$\Delta\phi(x_n) = 31.38x_n + 1.72$$
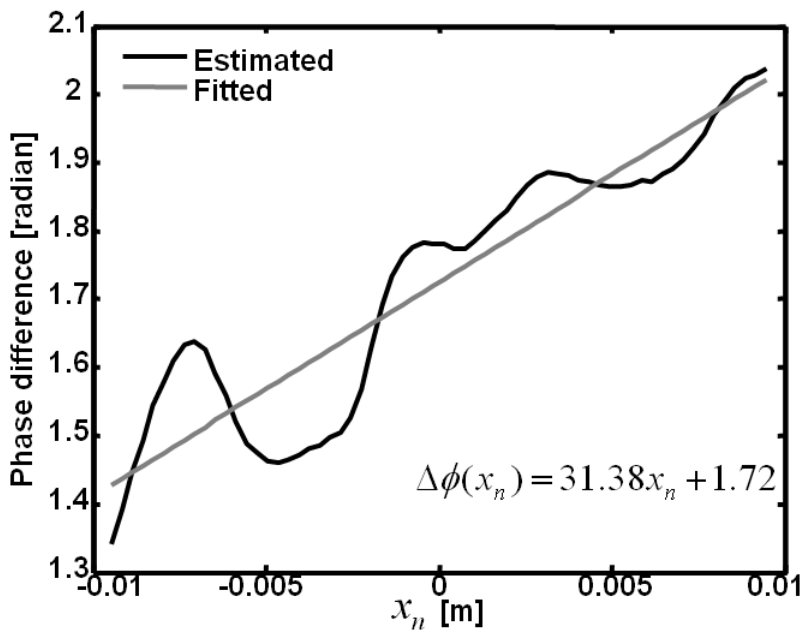
Fig. 2-6. Illustration of the phase differences as functions of the x_n for a simulation data. The theoretical velocity and Doppler angle for the data are 30 cm/s and 45°, respectively.

X_n, then using (2-11), (2-7), (2-12), and (2-13), the estimated axial and lateral velocity components are 21.1 and 23.1 cm/s, respectively.

Fig. 2-7 shows the relations between the SD of the estimated axial velocity and the Doppler angle for the proposed and conventional methods. This figure also shows the SD for the lateral velocity estimated using the proposed method. As a comparison, the predicted value using (2-20) for the lateral velocity (gray line) estimated using the speckle tracking method [29] is also shown. The results were normalized by the ideal value (of 20 cm/s). This figure shows the data for Doppler angles from $0°$ to $90°$ with a step size of $15°$, with 30 data sets used at each angle to produce the means and SDs. As predicted, our method is superior to the conventional method for axial velocity estimation, and exhibits lower variance for axial velocity estimation than for lateral velocity estimation.
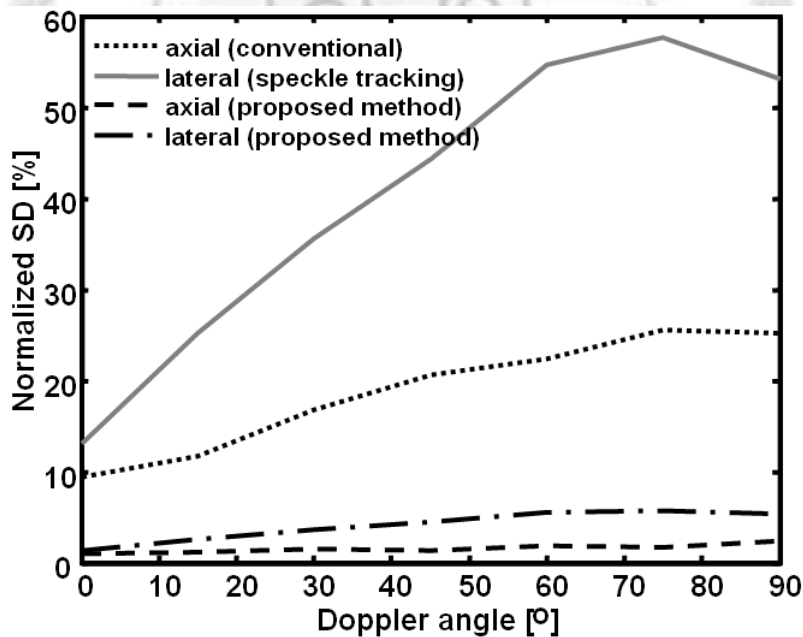
Fig. 2-7. Simulation results. Estimation errors as functions of the Doppler angle for the axial and lateral velocities using the proposed technique. For comparison, the results for estimating the axial velocity using the conventional method and the predicted values using a speckle-tracking method as described previously [49] are also shown.
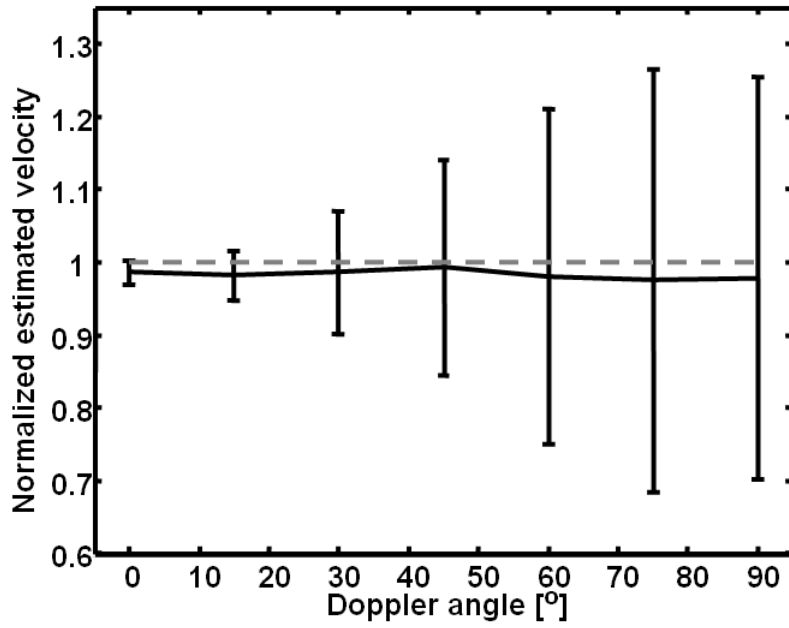
(a)
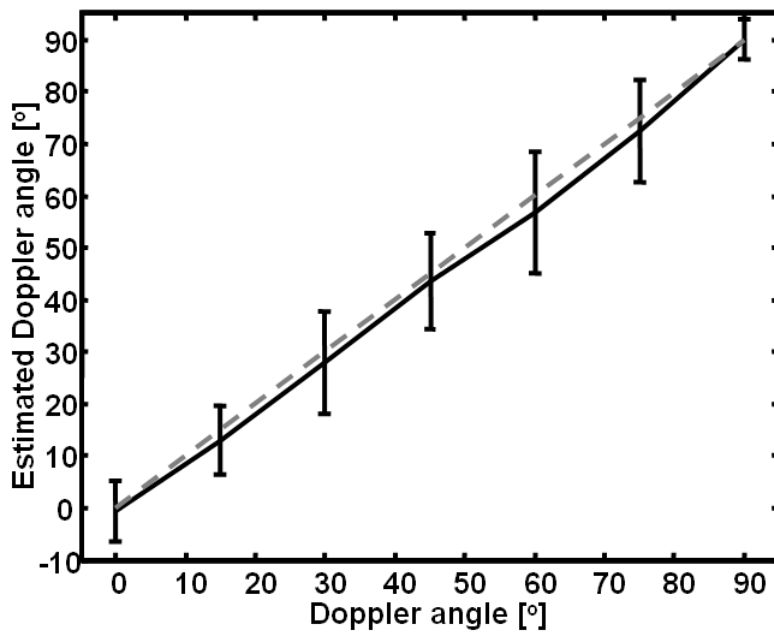
(b)
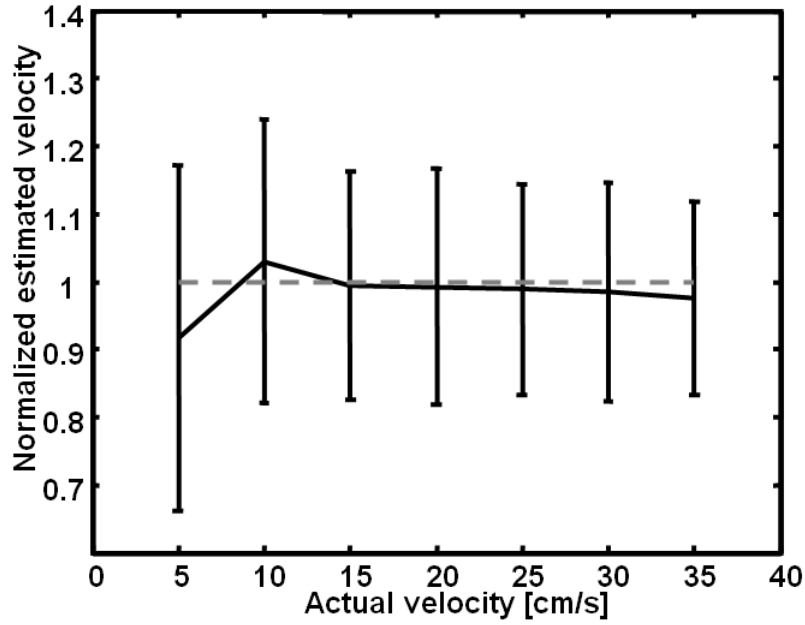
(c)

Fig. 2-8. Simulation results. (a) Normalized estimated vector velocity as a function of the Doppler angle. (b) Estimated Doppler angle as a function of the actual Doppler angle. (c) Normalized estimated vector velocity as a function of the actual velocity. The dashed line shows the ideal value, and the error bars indicate plus and minus one SD relative to the mean.

The estimated vector velocities are shown in Fig. 2-8 for Doppler angles from $0°$ to $90°$ with a step size of $15°$, and for velocities ranging from 5 to 35 cm/s with a step size of 5 cm/s. Fig. 2-8(a) plots the amplitude of the estimated vector velocity versus the Doppler angle, normalized by the ideal values. The mean and SD for the estimated velocity vector were 0.98 and 0.15, respectively. Fig. 2-8(b) plots the estimated Doppler angle versus the Doppler angle in the same format as Fig. 2-8(a). The mean SD of the estimated Doppler angle was $8.11°$. Fig. 2-8(c) plots the amplitude of the vector velocity versus the actual velocity. The SDs for velocities of 5 and 35 cm/s were 0.25 and 0.14, respectively. The results were normalized by the ideal values. The dashed line shows the ideal value, and the error bars indicate plus and minus one SD relative to the mean. Fig. 2-8(a) shows that the accuracy of velocity estimation generally decreases with the Doppler angle, whereas Fig. 2-8(b) shows that the accuracy of Doppler angle estimation generally increases with the Doppler angle. This

is due to the variances being larger for the estimated lateral velocity than for the estimated axial velocity. Fig. 2-8(c) shows that the variance is large when estimating a small velocity, which is due to estimation errors resulting from small phase differences in the arrival data.

2.4 EXPERIMENTAL INVESTIGATION

2.4.1 Experimental Methods

Experiments were performed to evaluate the efficacy of the proposed vector velocity estimator. Fig. 2-9 shows a schematic of the experimental setup. A programmable array system with 64 channels (DiPhAS, IBMT, Fraunhofer Institutes, Germany) was used to acquire the aperture domain data. A gelatin phantom containing 106-μm acid-washed glass beads (G-4649, Sigma, St. Louis, MO) for speckle generation was placed in a water tank. The linear-array transducer with a central frequency of 5 MHz (L6/128, Acuson, Mountain View, CA) was moved along the x- and z-axes controlled by a 3-D positioning system so as to emulate the lateral and axial velocity components, respectively. In this way, 2-D constant flows were emulated for different Doppler angles comprising motion in the directions of the x- and z-axes. For each position, a complete data set (i.e., 4096 RF A-scans recorded from a 64-element array, where each recording represents the echo signal of 64 independent transmitters and 64 independent receivers without any time delay applied) was acquired at a sampling frequency of 20 MHz. The data sets were used to reconstruct the aperture domain data with full dynamic focus on both transmit and receive.
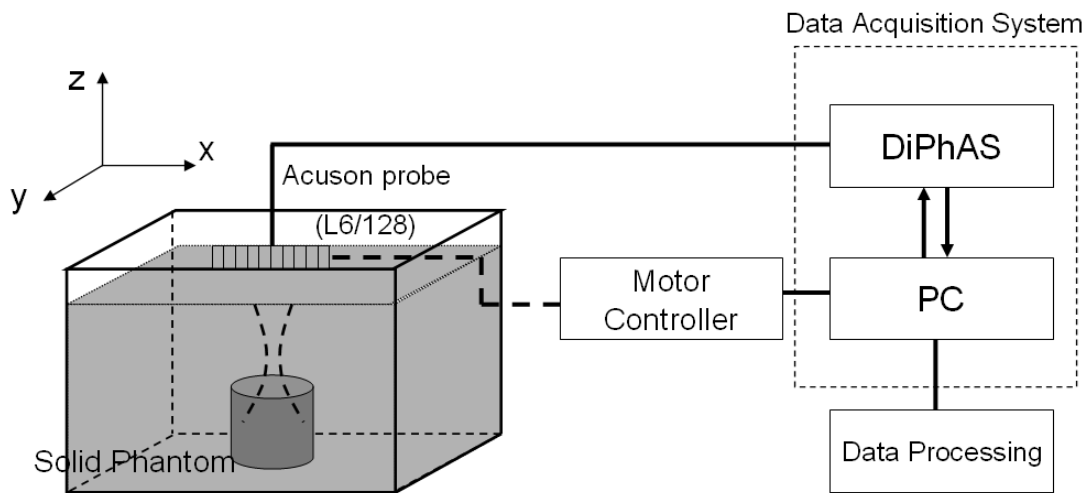
Fig. 2-9. The experimental setup.

2.4.2 Experimental Results
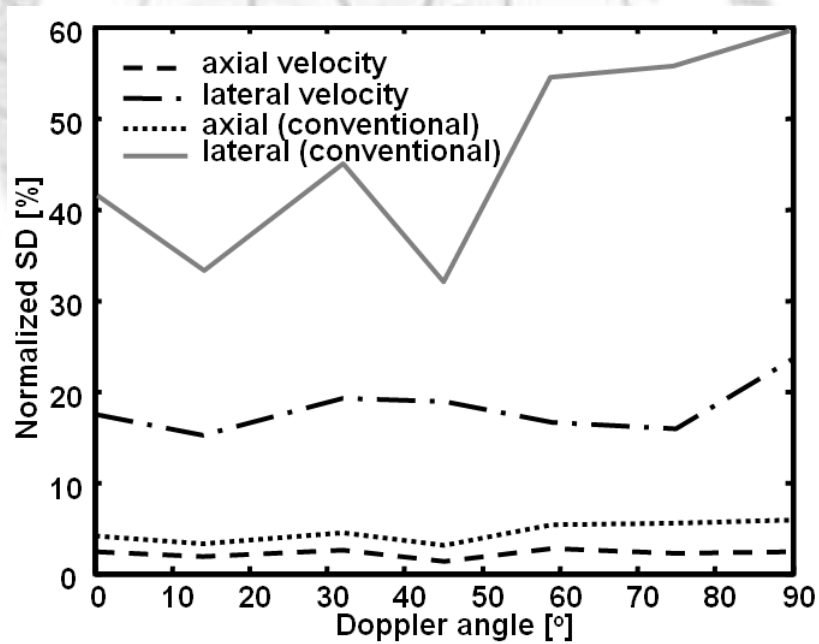
Fig. 2-10. Experimental results. Estimation errors as functions of the Doppler angle for the axial and lateral velocities using the proposed technique. For comparison, the results for estimating the axial velocity using the conventional method and the predicted values using a speckle-tracking method as described previously [49] are also shown.
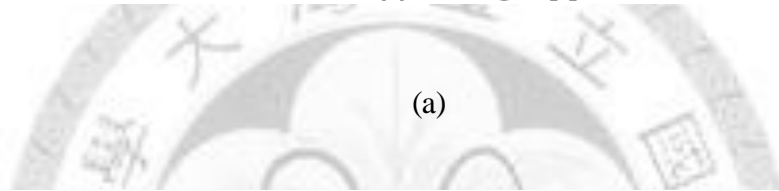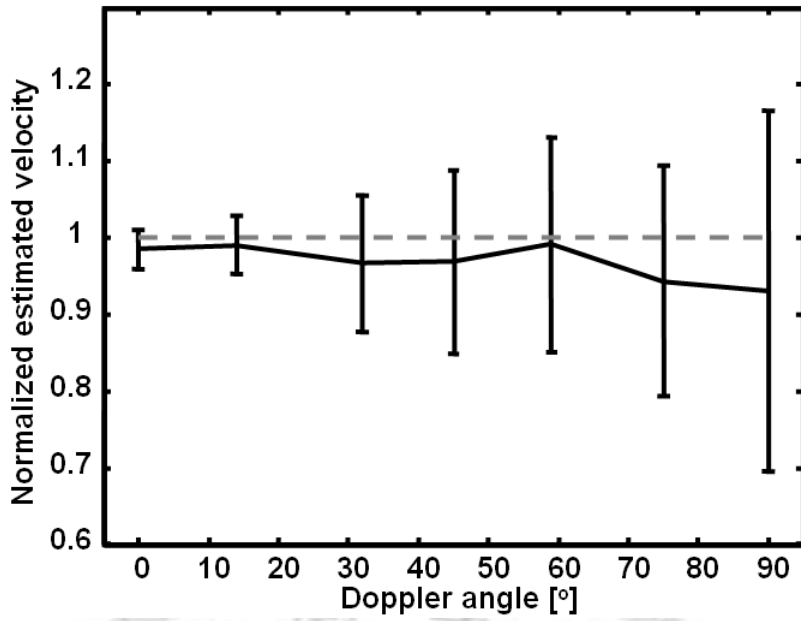
(a)
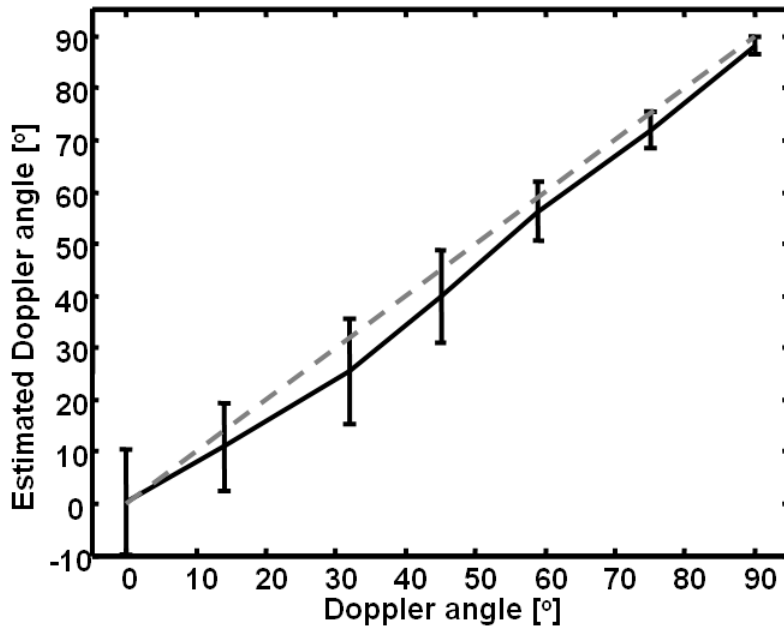
(b)

Fig. 2-11. Experimental results. (a) Normalized estimated vector velocity as a function of the Doppler angle. (b) Estimated Doppler angle as a function of the actual Doppler angle. The dashed line shows the ideal value, and the error bars indicate plus and minus one SD relative to the mean.

36

The parameters were similar to those for the simulations: 16 firings, and Doppler angles ranging from $0°$ to $90°$ with a step size of $15°$. 20 independent experiments performed to produce the means and SDs. Comparing the experimental results shown in Figs. 10 and 11 with those in Figs. 7 and 8 (in the same format) reveals that the experimental and simulation results were generally consistent. For all Doppler angles, the mean errors for the axial and lateral velocities were 2.18% and 18.11%, respectively. For comparison, the mean error for the axial velocity was 4.51% when using the conventional method. The mean and SD for the estimated velocity vector were 0.96 and 0.11, respectively. The mean SD of the estimated Doppler angle was $6.9°$. The accuracy was higher for the estimated axial velocity than for the estimated lateral velocity, and the accuracy of the estimated axial velocity was higher when using the proposed method than when using the conventional method.

2.5 DISCUSSION AND CONCLUDING REMARKS

This chapter has analyzed a proposed system that uses aperture domain data to estimate the 2-D vector velocity for an arbitrary Doppler angle. The differential time shifts of aperture domain data between two consecutive firings caused by the flow can be estimated by the phase shifts of the baseband data, which are determined using an autocorrelation function at each channel. The performance of the estimator can be improved by temporal or spatial averaging (i.e., a selected Doppler range gate) so as to reduce the influence of system noise. When the SNR is higher than -1.93 dB, the accuracy of the estimated axial velocity is higher for the proposed method than for the conventional method. The simulation and experimental results show that axial velocity estimation is more accurate than lateral velocity estimation. The results also show that the ratio of the variances of the estimated axial and lateral velocities was consistent with the results of Walker and Trahey [49], whereas the means of the vector velocities and the Doppler angles were underestimated in the experimental results. The underestimation of the lateral velocity component (which was responsible for the other underestimations) did not occur in experiments using a wire phantom as a moving source, but only when using the speckle-generating phantom. As discussed

in[3, 4], measurements of the arrival time from diffuse scatterers underestimate the actual arrival-time function determined from a Fresnel integral. As a result, the arrival-time function (2-1) related to the lateral extent of the insonifying beam is underestimated, resulting in the estimation errors evident in the present experimental results. The lateral velocity estimated using parameter a_1 in (2-7) is too low due to the arrival-time function (2-1) being underestimated along the array direction. The arrival-time function was not underestimated in the simulations using Field II. Since the underestimation of arrival time is noteworthy when the beam is broad [3], the randomly generated scatterers placed in the *x-z* plane with tight focus in lateral extent did not influenced by the phenomenon. Furthermore, the Doppler angle in the experimental results also tended to be underestimated due to this underestimation of the lateral velocity component.

The accuracy of the proposed method is related to the number of system channels, and using (2-17) and (2-19) with the assumption that the number of channels is sufficiently large ($N \geq 8$), the variance of the estimated axial and lateral velocities can be approximated by

$$Var(\hat{v}_{lateral}) \propto \frac{1}{N^3}$$

$$Var(\hat{v}_{axial}) \propto \frac{1}{N}.$$

(2-23)

These relationships indicate that the accuracies of both the estimated axial and lateral velocities improve with the number of system channels, with this dependence being stronger for the lateral velocity.

The implementation of the proposed method requires splitting the receive aperture into (smaller) subapertures that widen the receive beam and thereby degrade the lateral spatial resolution and sensitivity. However, since the effective beam is the multiplication of transmit and receive beams, it is not as wide as the receive beam due to the full aperture size being used for transmit. As a result, although the lateral spatial

resolution is slightly degraded compared to using the entire aperture for both transmit and receive, the effective resolution of the aperture is still sufficient for estimating the lateral velocity.

The proposed method requires N autocorrelators due to the use of N subapertures for velocity estimation, compared with the conventional color Doppler method requiring only one autocorrelator. Thus, the system complexity increases with the number of subapertures, and hence determining the optimal number of subapertures requires both the system complexity and the estimation accuracy to be taken into account. A practical approach to achieving a good trade-off between the system complexity and the estimation accuracy is adaptively adjusting the number of subapertures according to the SNR given an upper limit for the number of subapertures.

The experiments in this chapter did not being performed with real flow. The minimum PRI specified by the DiPhAS programmable array system is 3 ms, which is quite high due to the large amount of aperture domain data. The maximum velocity that can be detected without aliasing is $v_{\max} = \lambda/(4 \cdot PRI)$, and hence the maximum flow velocity that could be detected in this study was about 0.6 cm/s (with $M = 4$). This long data acquisition time makes it infeasible for real flow experiments. Therefore, the vector velocity was only estimated for a constant flow in both simulations and experiments.

For real flow estimation, the signal scattered from blood is degraded by signals scattered from the stationary or slowly moving tissue. The robustness of the flow estimation technique depends on sufficient clutter rejection. Therefore, wall filters for the proposed technique should be used in parallel for all individual subapertures over slow-time, and this highly increases the system complexity. Another concern is that a wall filter degrades the performance of the proposed method due to spatial resolution degradation resulted from a small receive subaperture size. A trade-off between performance and system complexity should be taken into account for the wall filter

design. To simplify the design, a method [51] using direct component removal as a high pass filter has been suggested, and the signal from slowly moving tissue can be suppressed by down mixing the signal with the estimated mean tissue frequency prior to the wall filter. Temporal averaging schemes (using (2-9)) and spatial averaging schemes (using the Doppler range gate) can be used to reduce the estimation errors due to nonnegligible velocity gradients and the presence of turbulence. Future studies should investigate the performance and robustness of the proposed technique in the regions where temporal or spatial velocity gradients are present.

The estimation accuracy for the proposed method is expected to be inferior due to velocity gradients, stationary or moving clutters, and at low SNR. However, since both blood and tissue are speckle generating objects, another feasible application for the proposed method is for tracking tissue motion such as heart wall motion detection or elastography. The proposed method should be suitable for these applications, because the wall filter is no longer required and the performance is improved for a higher SNR. The presence of phase aberration (i.e., time delay errors due to sound velocity inhomogeneities) is expected to degrade both the spatial resolution and sensitivity of the proposed technique. This could be improved by combining aberration-correction techniques using aperture domain processing, such as correlation-based methods [3, 4].

The first advantage of the proposed method is that it requires fewer firings (e.g., 4 to 16, depending on the SNR) than conventional methods (e.g., typically 64 firings for the spectral broadening technique) for estimating velocity vectors. The second advantage is that it is less computationally demanding than other methods (e.g., speckle tracking). The third advantage is that the proposed method does not increase the system complexity for transmit beam formation (e.g., spatial quadrature). The fourth advantage is that the use of the entire time-shift profile improves the accuracy of the estimated axial velocity compared with that of the conventional Doppler technique.

CHAPTER 3 PERFORMANCE EVALUATION OF COHERENCE-BASED ADAPTIVE IMAGING

Sound-velocity inhomogeneities degrade both the spatial resolution and the contrast in diagnostic ultrasound. We previously proposed an adaptive imaging approach based on the coherence of the data received in the channels of a transducer array, and tested it on phantom data. In this study the approach was tested on clinical breast data, and compared with a correlation-based method that has been widely reported in the literature. The main limitations of the correlation-based method in ultrasonic breast imaging are the use of a near-field phase-screen model and the integration errors due to the lack of a 2D array. In contrast, the proposed coherence-based method adaptively weights each image pixel based on the coherence of the receive-channel data. It does not make any assumption about the source of the focusing errors and has been shown to be effective using 1D arrays. This study tested its *in vivo* performance using clinical breast data acquired by a programmable system with a 5 MHz, 128-channel linear array. Twenty-five cases (six fibroadenomas, ten carcinomas, six cysts, and three abscesses) were investigated. This chapter explores the contrast and other general characteristics of the GCF technique, and is organized as follows: In Section 3.1, the definition of GCF is given. Section 3.2 describes the basic principles of the GCF-weighting technique. The experimental methods for the GCF-weighting method are described in Section 3.3. Section 3.4 presents the experimental results, and the results are then discussed in Section 3.5. The chapter concludes in Section 3.6.

3.1 GENERALIZED COHERENCE FACTOR (GCF)

The GCF is calculated using the Fourier spectrum of the aperture domain data, which are the data received in individual array channels after the application of

focusing delays but prior to beam summation. The corresponding Fourier spectrum is obtained by performing a discrete Fourier transform across the array at each time (i.e., depth):

$$x_n(t) \xrightarrow{\text{FT}} p(k,t), \tag{3-1}$$

where $p(k, t)$ is the Fourier spectrum with spatial frequency index k and time variable t. As described in [12], the spectrum can be viewed as an approximation of multiple parallel receive beams centered at the transmit beam direction. The definition of the CF described in (1-14) can also be expressed as follows:

$$\text{CF} = \frac{|p(0,t)|^2}{\sum_{k=-N/2}^{N/2-1} |p(k,t)|^2}. \tag{3-2}$$

The numerator of (3-2) is the energy of the DC component of the spectrum, and the denominator is the total spectral energy. The DC component represents the signals received from the transmit beam direction (i.e., on-axis component), and the other components represent the signals from other angles (i.e., off-axis components).

Adaptive weighting using CF is feasible for point-like targets. However, for diffuse scatterers (i.e., speckle-generating objects), part of the mainlobe signal appears within the low-frequency region. Therefore, using the ratio of the DC energy to the total energy as a weighting factor underestimates the coherence. The GCF was proposed to take this into account [16], and is thus defined as the ratio of the energy within a certain low-frequency region to the total energy:

$$\text{GCF} = \frac{\sum_{k=-M_0}^{M_0} |p(k,t)|^2}{\sum_{k=-N/2}^{N/2-1} |p(k,t)|^2}, \tag{3-3}$$

where M_0 denotes the prespecified cut-off frequency in the spatial frequency domain. Note that the CF is the special case of the GCF with M_0=0.

3.2 SIGNAL PROCESSING PROCEDURES

The signal processing procedures we employed are shown schematically in Fig. 3-1. After the echo signal is received and digitized by the A/D converter, the received RF data are demodulated down to baseband and the baseband beam former applies geometric focusing delays and phase rotations to the baseband data. The B-mode image is then obtained by performing beam summation across the array with prespecified apodization. The GCF is calculated for the specific configuration using the delayed baseband data across the aperture at all ranges prior to beam summation. Note that a baseband beam former is necessary fot the GCF estimation. The amplitude of the beam sum is then simply multiplied by the corresponding GCF:

$$y_{\textbf{weighted}} = \textbf{GCF} \cdot y, \tag{3-4}$$

The weighted beam-sum data are then stored in a buffer for further signal processing, scan conversion, and display.
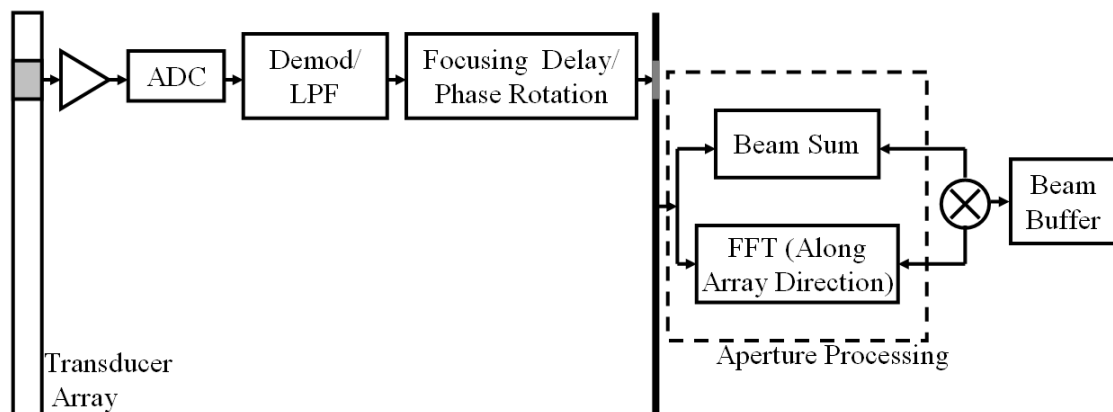
Fig. 3-1. Signal processing procedures of the proposed GCF-weighting technique.

3.3 CLINICAL EXPERIMENTS SETUPS

Experiments were performed to evaluate the efficacy of the proposed method in clinical breast imaging. Clinical data of the female breast were collected in the ultrasonic consulting room of the Taipei Veterans General Hospital by one of the authors (Y.-H. Chou) after patients had provided informed consent. The 25 included patients, aged from 23 to 89 years, presented with six fibroadenomas, ten carcinomas, six cysts, and three abscesses. A schematic of the experimental apparatus is shown in Fig. 3-2, which included a mechanical compression stage similar to that used in X-ray mammography to stabilize the breast during data acquisition. A programmable imaging system with 64 system channels (DiPhAS) was used to acquire the aperture domain data. The linear transducer array had a center frequency of 5 MHz, a -6 dB bandwidth of 4.1 MHz and 128 channels (L6/128) at a pitch of 0.3 mm. A complete data set was obtained from each patient (i.e., 128×128 RF A-mode scans recorded from the 128-element array, where each A-mode scan represents the echo signal of a particular transmit/receive combination) at a sampling rate of 20 MHz. Each complete data set took approximately 3 s to acquire. The acquired data sets were used to reconstruct the aperture domain data with full dynamic focus on both transmit and receive. To confirm that no severe motion occurs during data acusition, the B-mode image is compared to a pre-scan image is also acquired using real-time imaging of DiPhAS. An f-number of 1 was applied for aperture control. All images displayed here are in linear gray scale with a dynamic range of 60 dB and are shown in a linear scan format. The step size for the linear scan was 0.15 mm (i.e., half the pitch of the transducers). B-mode images are formed by applying transmit and receive focusing delays before beam summation, and multiple imaging methods can be compared with one another using the same data set.
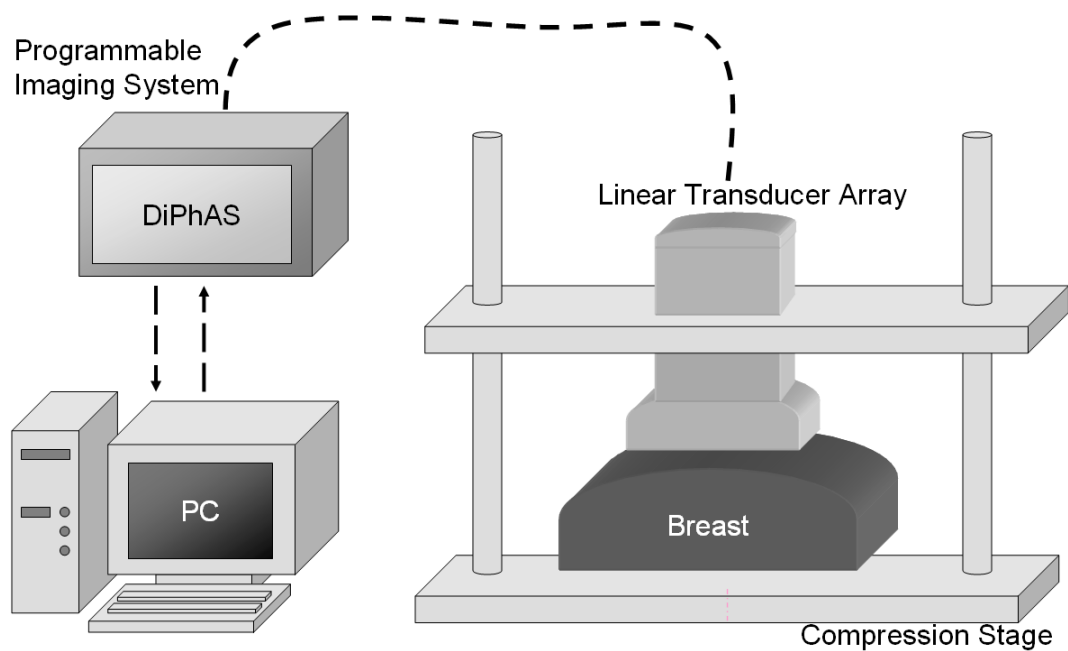
Fig. 3-2. Clinical data-acquisition apparatus.

3.4 EXPERIMENTAL RESULTS

3.4.1 Cut-off Frequency M_0

In the GCF technique, cut-off frequency M_0 should be specified so as to achieve optimal performance. Both the contrast ratio (CR) and contrast-to-noise ratio (CNR) were used in the experiments to evaluate the effects of varying M_0. The CR is defined as the ratio between the mean value in a background region to that in a region of interest (ROI) [4]. The CNR is defined as the ratio between the CR and the SD of the image intensity in a background region [5]. Fig. 3-3(a) shows an original image without application of the GCF-weighting method, and Figs. 3-3(b)–(f) show the GCF-weighted images with M_0 ranging from 0 to 4. Note that $M_0=0$ represents the case of using the CF. The background region and ROI used to calculate CRs and CNRs are indicated in Fig. 3-3(a) by the black and white boxes, respectively. The ROI in this case is a cyst. Note that in all cases the contrast is clearly improved and

the background noise is suppressed. Figs. 3-4(a) and (b) show the CR and CNR after GCF weighting as functions of M_0, respectively. Fig. 3-4(a)
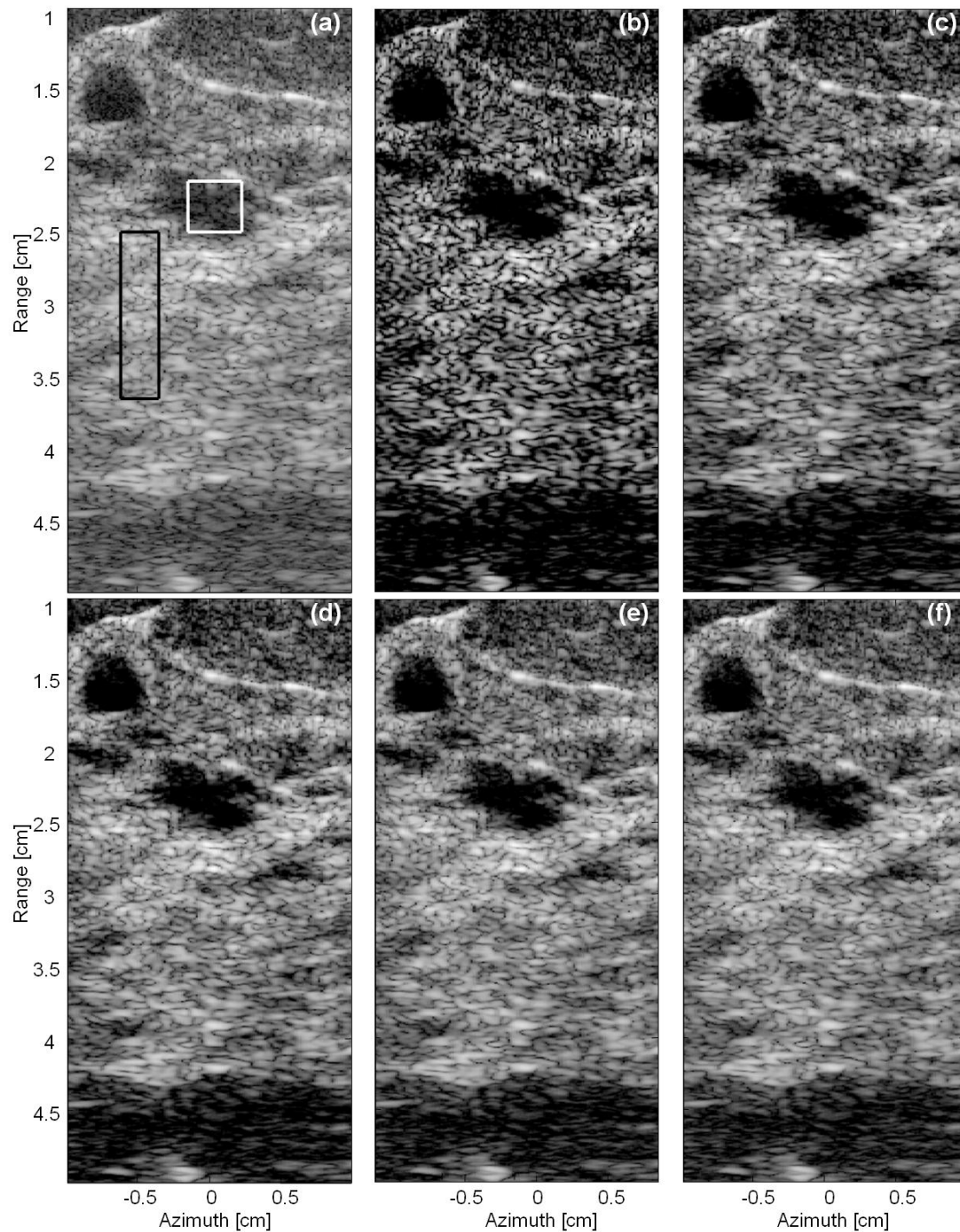
Fig. 3-3. Effects of cut-off frequency M_0 on the images of a a cyst, displayed with a dynamic range of 60 dB. (a) Original image. (b)–(f). GCF-corrected images for M_0 values of 0 (b), 1 (c), 2 (d), 3 (e), and 4 (f).

shows that the CR was improved in all cases, decreasing as M_0 increased. When the background-intensity variations are taken into account, Fig. 3-4(b) shows that the CNR was not improved when $M_0=0$. Nevertheless, with $M_0 \geqq 1$, CNR improvement is again demonstrated. Specifically, the optimal CNR was achieved at $M_0=3$ in this case. The results indicate that using CF as a weighting index can effectively increase the CR. However, CF also gives rise to strong intensity variations and degrades the CNR. This is also illustrated in Fig. 3-3(b), where the CF-weighting technique introduced artifactual black holes in the background region, which in turn affect the detection of an ROI. Based on these results, $M_0=3$ was used in the subsequent investigations (which are described below).
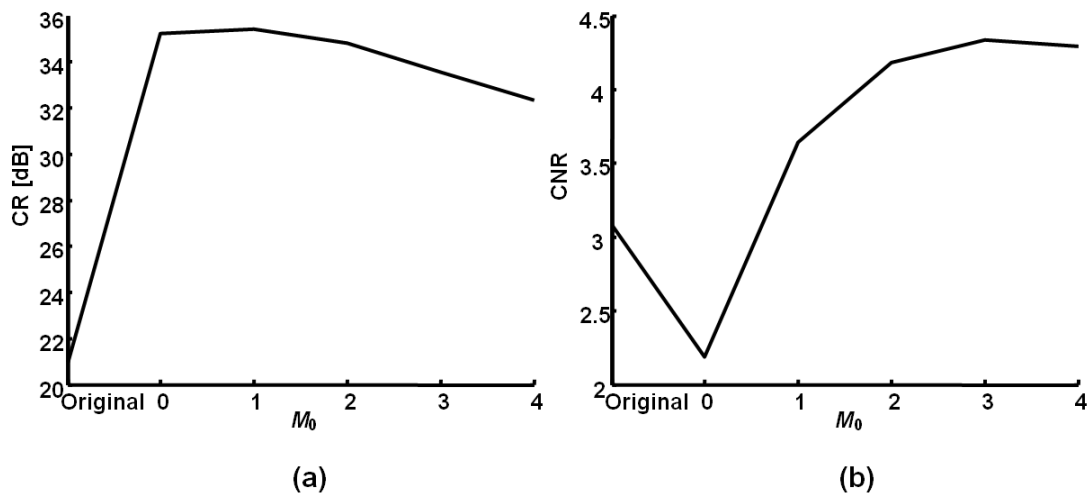
Fig. 3-4. Values of CR (a) and CNR (b) for the specimen shown in Fig. 3-3 as functions of M_0.

3.4.2 Cyst

The sonogram needs to be interpreted accurately in order to avoid unnecessary biopsies and to differentiate a cyst from a solid mass. Fig. 3-5 shows images of a cyst in a 66-year-old female patient. The background and the ROI regions used in the CR and CNR calculations are indicated in Fig. 3-5(a) by the black and white boxes, respectively. Fig. 3-5(a) shows the original image, Fig. 3-5(b) shows the image
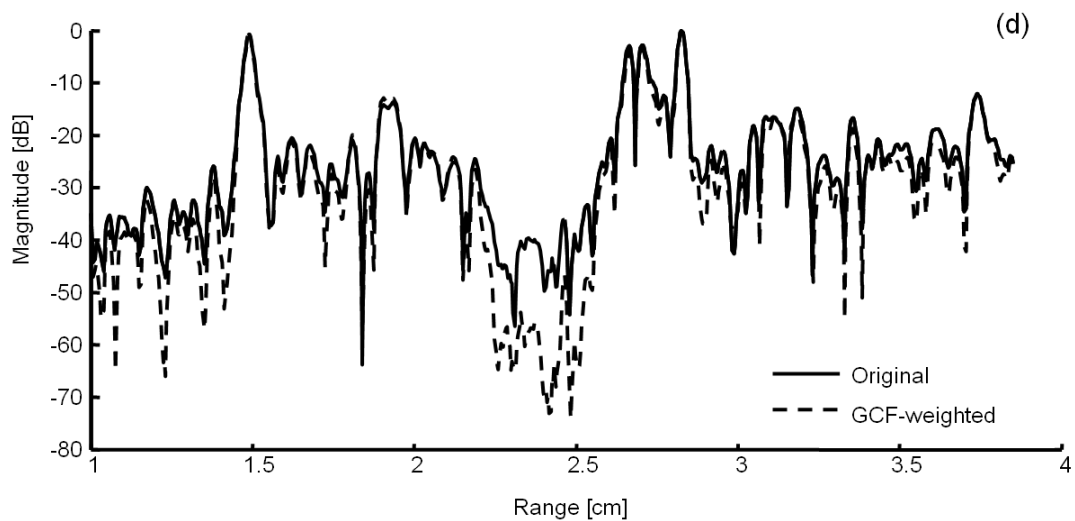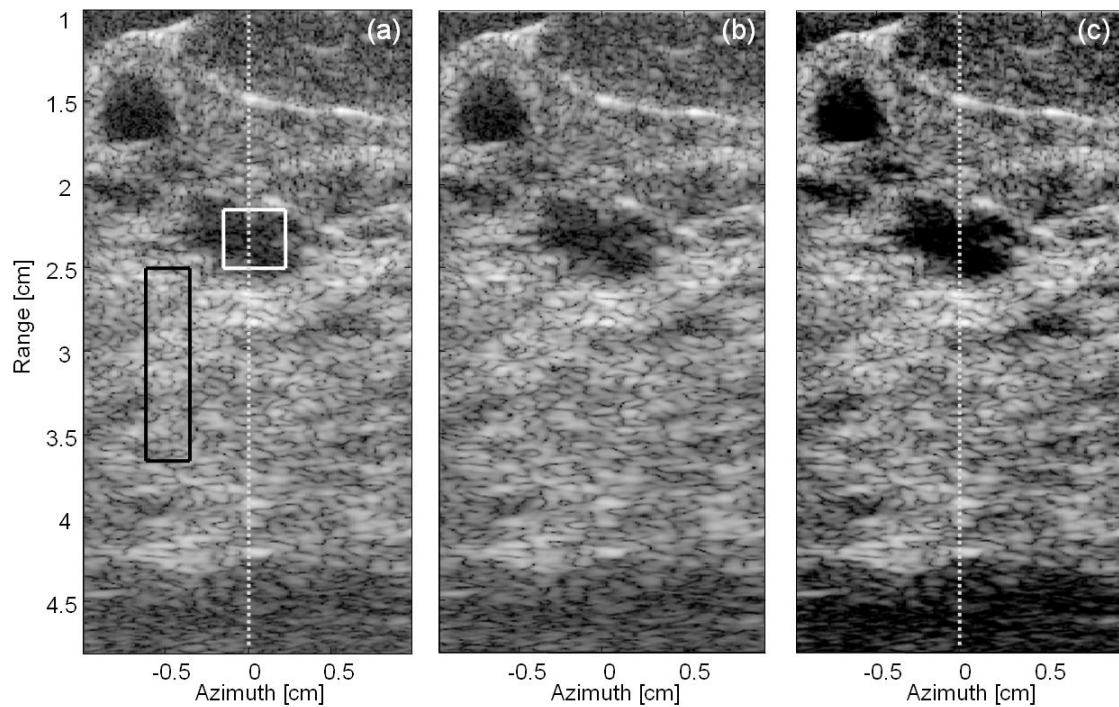
Fig. 3-5. Images of a cyst in a 66-year-old woman, displayed with a dynamic range of 60 dB: original B-mode image (a), and images obtained using the correlation-based method (b) and the GCF-weighting method (c). (d) shows the scan-line data along the gray dotted lines shown in (a) and (c) using solid and dashed lines, respectively.

obtained using the correlation-based method (as a reference) [3, 4], and Fig. 3-5(c) is the image obtained with adaptive compensation using GCF weighting. A single

aberration profile (infinite-sized isoplanatic patch) is used to correct the entire image for the correlation-based method. The aberration profile is calculated using the peak of the cross correlation with the linear components removed. The CRs and CNRs were 20.97 dB and 3.07 for the original image, 20.52 dB and 2.95 for the correlation-based method, and 33.53 dB and 4.33 for the GCF-weighting method. With the correlation-based method, the CR and CNR were slightly degraded: by 0.44 dB and 3.85%, respectively. This may be due to the phase aberrations in the breast being more distributed, and aberrator integration errors may be present with the 1D array. In contrast, the improvements in the CR and CNR using the GCF-weighting method were 12.56 dB and 40.97%, respectively. The original image shows an indistinct internal echo within the cystic mass, whereas the GCF-weighted image shows that the signal within the cystic mass was effectively suppressed and that the CR was enhanced. Fig. 3-5(d) shows the scan-line data along the gray dotted lines shown in Figs. 3-5(a) and (c). The results also demonstrate the efficacy of effective sidelobe reduction using GCF-weighting method in the ROI region while the background noise is just slightly increased. The margin of the cyst was more distinct than that in the original image. These results illustrate the significant improvement in contrast and boundary definition in this case.

3.4.3 Fibroadenoma

Fig. 3-6 shows images of a fibroadenoma lesion in a 42-year-old female patient. The background and the ROI regions used in the calculation of the CR and CNR are indicated in Fig. 3-6(a) by the black and white boxes, respectively. Fig. 3-6(a) shows the original image, and Figs. 3-6(b) and (c) show the corrected images obtained using the correlation-based method and the GCF-weighting method, respectively. The CRs and CNRs were 16.92 dB and 2.76 for the original image, 17.51 dB and 2.82 for the correlation-based method, and 25.73 dB and 3.67 for the GCF-weighting method. The CR and CNR improved by 0.58 dB and 2.36% with the correlation-based method and by 8.81 dB and 33.07% with the GCF-weighting method. The original image and the image obtained using correlation-based method show poor boundary definition.

However, the use of the GCF-weighting method noticeably improves the contrast and boundary definition in this case. In spite of these improvements, the suppression of the echo signal in the ROI region reduces the delineation of the interior echo, resulting in possible confusion when differentiating a fibroadenoma (solid) from a cyst (liquid) – this requires further investigation. Nonetheless, in this case the lesion is detected as a fibroadenoma without confusion due to the boundary echogenicity. Typically, a cyst has brighter wall echoes, while the echogenicity of a fibroadenoma is not so strong.
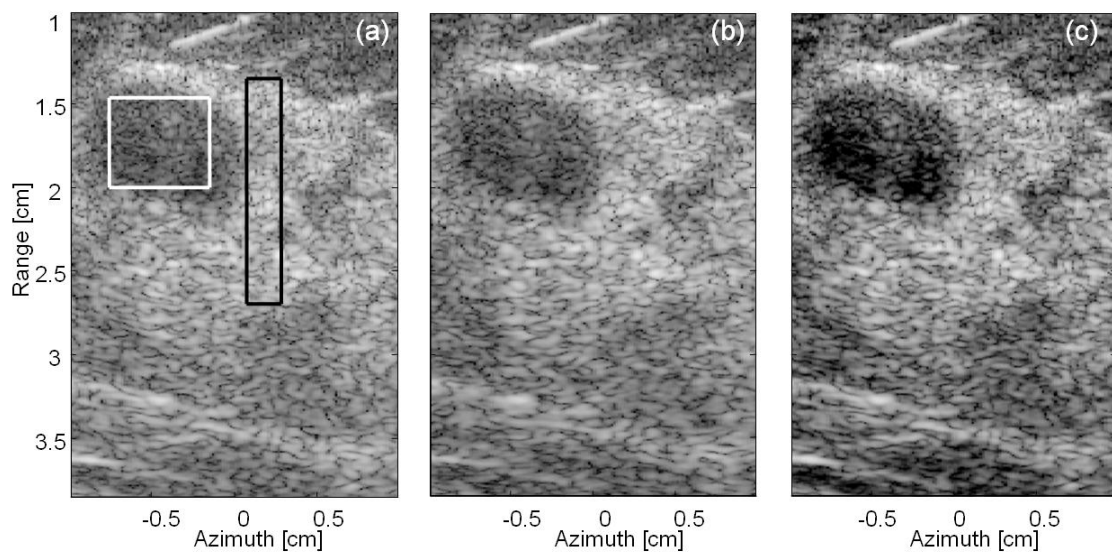
Fig. 3-6. Images of a fibroadenoma in a 42-year-old woman, displayed with a dynamic range of 60 dB: original B-mode image (a), and images obtained using the correlation-based method (b) and the GCF-weighting method (c).

3.4.4 Carcinoma

Fig. 3-7 shows images of a carcinoma lesion in a 63-year-old female patient. The background and the ROI regions used in the calculation of the CR and CNR are indicated in Fig. 3-7(a) by the black and white boxes, respectively. Fig. 3-7(a) shows the original image, and Figs. 3-7(b) and (c) show the corrected images obtained using the correlation-based method and the GCF-weighting method, respectively. The CRs and CNRs were 13.63 dB and 2.19 for the original image, 13.80 dB and 2.23 for the

correlation-based method, and 21.52 dB and 2.87 for the GCF-weighting method. The CR and CNR improved by 0.16 dB and 1.59% with the correlation-based method and by 7.89 dB and 30.75% with the GCF-weighting method, respectively. Again, the original image shows an indistinct lesion margin. The internal echo and several echogenic foci indicating microcalcifications within the breast parenchyma are also not clearly evident. The image obtained using correlation-based method is again almost the same. The GCF-weighted image shows better characterization of the margin, enhanced delineation of the internal architecture, and enhanced conspicuity of microcalcifications within the breast parenchyma due to improved spatial resolution and contrast.
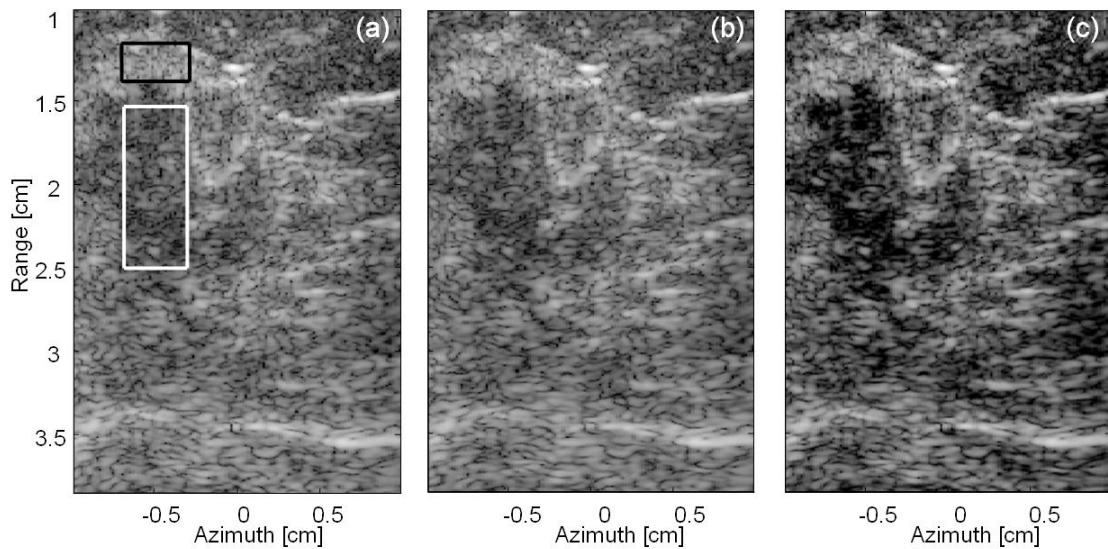
Fig. 3-7. Images of a carcinoma in a 63-year-old woman, displayed with a dynamic range of 60 dB: original B-mode image (a), and images obtained using the correlation-based method (b) and the GCF-weighting method (c).

3.4.5 Abscess

Fig. 3-8 shows images of an abscess lesion in a 31-year-old female patient. The background and the ROI regions used in the calculation of the CR and CNR are indicated in Fig. 3-8(a) by the black and white boxes, respectively. Fig. 3-8(a) shows the original image, and Figs. 3-8(b) and (c) show the corrected images obtained using

the correlation-based method and the GCF-weighting method, respectively. The CRs and CNRs were 22.20 dB and 3.73 for the original image, 22.85 dB and 3.80 for the correlation-based method, and 32.11 dB and 4.59 for the GCF-weighting method. The CR and CNR improved by 0.65 dB and 1.83% with the correlation-based method and by 9.91 dB and 23.10% with the GCF-weighting method, respectively. The original image shows a well-circumscribed hypoechoic mass with internal echogenic debris, a slight posterior acoustic enhancement, and indistinct calcification. Again, the image obtained using correlation-based method is almost the same. The GCF-weighted image shows a clearer lesion margin and enhanced delineation of the internal architecture due to improvement of the contrast.
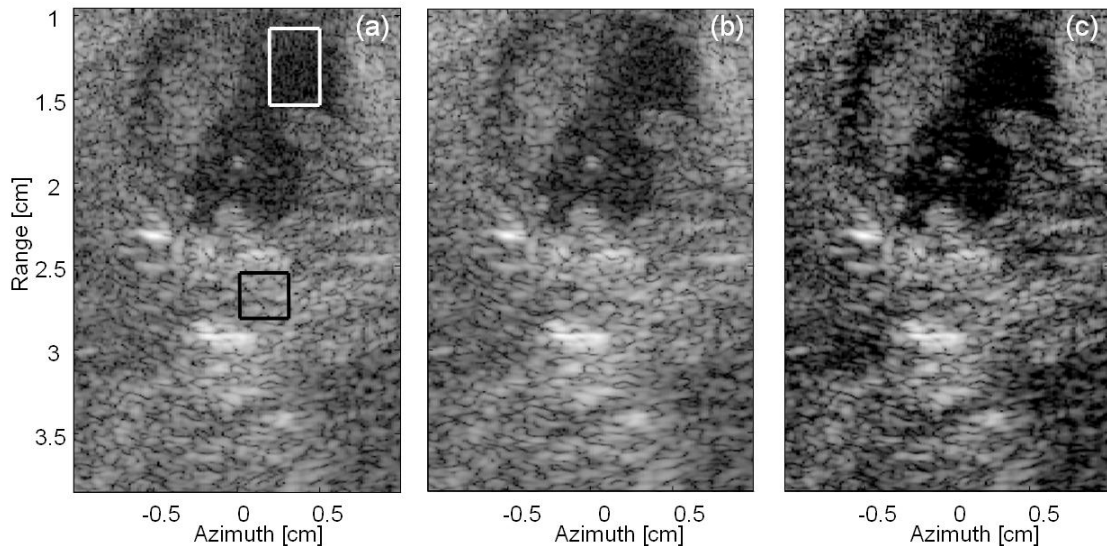
Fig. 3-8. Images of an abscess in a 31-year-old woman, displayed with a dynamic range of 60 dB: original B-mode image (a), and images obtained using the correlation-based method (b) and the GCF-weighting method (c).

3.4.6 Milk of Calcium

Fig. 3-9 shows images of a milk of calcium in a cyst lesion in a 25-year-old female patient. Fig. 3-9(a) shows the original image, and Figs. 3-9(b) and (c) show the corrected images obtained using the correlation-based method and the GCF-weighting

method, respectively. The contrast between the milk of calcium and the tissue improved by 0.05 dB for the correlation-based method and by 4.47 dB for the GCF-weighting method. The lateral and axial −6-dB widths of the milk of calcium object were 0.51 and 0.39 mm in the original image, 0.55 and 0.41 mm in the correlation-based image, and 0.43 and 0.32 mm in the GCF-weighted image, respectively. The GCF-weighting method improved both the spatial resolution and the contrast in this case, which in turn helped in the detection of calcification.
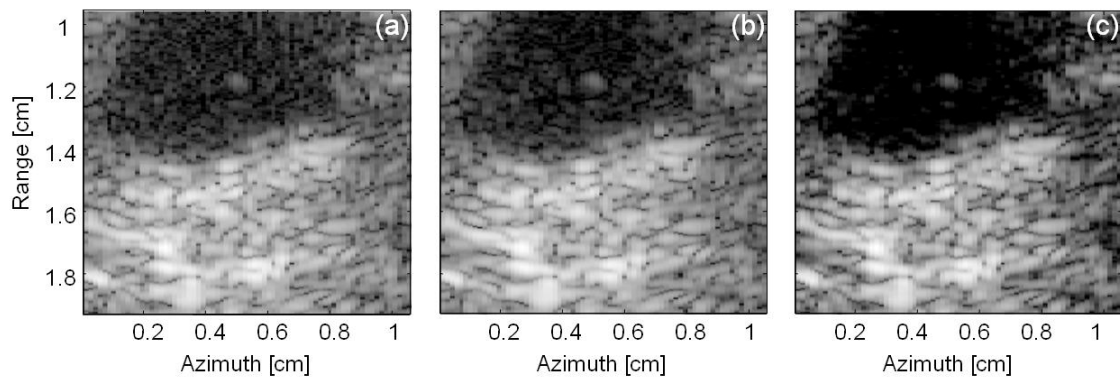
Fig. 3-9. Images of a milk of calcium in a cyst in a 25-year-old woman, displayed with a dynamic range of 60 dB: original B-mode image (a), and images obtained using the correlation-based method (b) and the GCF-weighting method (c).

3.5 DISCUSSION

The CR and CNR values obtained with the correlation-based and GCF-weighting methods are listed in Table 3-1. The mean values for the CR and CNR improvements were 0.42 dB and 3.4% for the correlation-based method and 8.57 dB and 23.20% for the GCF-weighting method. It should be noted that whilst the CR and CNR are widely reported as performance indices in the literature and are directly related to fundamental characteristics of an image, their exact values may change with the selected ROI and may not be directly related to diagnostic outcomes. Therefore, these images were also evaluated by an experienced clinician (Y.-H. Chou) using the following scoring system: 2+, significant improvement; 1+, moderate improvement; 0,

no noticeable effects; 1−, slight degradation; and 2−, significant degradation. In general, application of the GCF-weighting method improved the image quality in all the cases assessed in this study. The improvement in the contrast was more significant for a liquid lesion (e.g., a cyst) than for a solid lesion (e.g., a fibroadenoma), and the improvement in the boundary definition makes it easier to detect a malignant tumor (e.g., a carcinoma).

The complete data set was used for clinical data acquisition in this study. Some inevitable drawbacks for beam formation using the complete data set including poor signal-to-noise ratios and motion artifacts resulted from long data acquisition time limit the practical application. However, using the complete data set is helpful for dynamic transmit focusing and therefore improves the coherence of the received channel data. For clinical application, using multi-zone transmit focusing may achieve an optimal compromise among these factors.

Although the correlation-based method is one of the most popular adaptive imaging methods reported in the literature, several problems were encountered when we applied this to breast imaging in this study. The estimated time delays are affected by several factors, including the cumulative error along the array direction, the signal-to-noise ratio, the correlation between adjacent channels, the kernel size, and the aberrator integration errors of a 1D array [6, 49, 52]. In addition to the above problems, the distributed sound-velocity inhomogeneities also represent a uniquely difficult problem in adaptive breast imaging, as illustrated in Fig. 3-10. The image shown in Fig. 3-10(a) is displayed without any aberration correction, and Fig. 3-10(b) plots the estimated time-delay errors as a function of the channel index at the image points corresponding to the boxes marked in Fig. 3-10(a), which are located along the same beam and are spaced by 7.7 mm. The time delays were estimated according to previously described principles [4]. Significant variations in the estimated time delays are clearly evident, and these limit the performance of the correlation-based method. The depth dependency of the estimated time delay may result from breast tissue

comprising a heterogeneous mixture of fatty, fibrotic, connective, and glandular tissues.

Table 3-1. Summary of the CR and CNR values.

Patient no.	Age (years)	Lesion type	CR			CNR			CR improvement (dB)		CNR improvement (%)		Subjective score
			Original	Corr. based	GCF	Original	Corr. based	GCF	Corr. based	GCF	Corr. based	GCF	GCF
1	53	Cyst	38.84	38.51	53.19	5.84	5.82	6.96	–0.33	14.34	–0.28	19.18	2+
2	49	Cyst	42.00	41.58	57.05	6.09	6.37	7.08	–0.41	15.04	4.51	16.19	2+
3	59	CA	26.00	26.53	36.70	4.03	3.99	4.73	0.52	10.69	–0.88	17.43	1+
4	28	FA	16.88	17.16	23.48	3.05	2.97	3.77	0.28	6.59	–2.73	23.37	1+
5	63	CA	13.63	13.80	21.11	2.19	2.23	2.85	0.16	7.47	1.59	28.09	2+
6	79	CA	10.39	11.05	19.57	1.53	1.59	2.46	0.65	9.17	3.85	60.94	2+
7	66	Cyst	20.97	20.52	33.53	3.07	2.95	4.33	–0.44	12.56	–3.85	40.97	2+
8	43	CA	4.35	4.84	7.67	0.66	0.73	0.96	0.49	3.32	11.65	45.41	1+
9	33	Abscess	14.11	14.57	20.05	2.16	2.23	2.59	0.46	5.93	2.96	19.58	1+
10	59	CA	16.37	17.94	24.87	2.58	2.79	3.29	1.56	8.50	7.92	27.24	2+
11	63	FA	15.32	15.28	20.59	2.67	2.65	2.99	–0.03	5.27	–0.90	12.05	1+
12	46	FA	15.74	16.12	20.94	2.47	2.53	2.89	0.38	5.20	2.30	16.94	1+
13	63	Abscess	12.99	13.05	20.68	2.20	2.15	3.05	0.06	7.68	2.60	38.29	2+
14	89	CA	12.22	12.26	19.43	1.70	1.73	2.04	0.03	7.20	1.90	20.04	1+
15	23	FA	14.19	14.07	18.40	2.54	2.65	2.92	–0.11	4.20	4.28	14.94	1+
16	50	CA	21.07	22.07	30.27	3.55	3.69	4.21	0.99	9.19	3.86	18.36	1+
17	42	FA	16.36	16.91	24.12	2.67	2.73	3.44	0.54	7.75	2.23	28.97	2+
18	25	Cyst	15.45	19.61	27.09	2.56	3.12	3.18	4.16	11.63	22.09	24.50	2+
19	45	CA	21.56	21.18	29.26	3.55	3.29	3.92	–0.37	7.70	–7.26	10.29	1+
20	45	CA	15.85	16.06	21.33	2.98	3.07	3.46	0.21	5.48	3.17	16.17	1+
21	47	Cyst	23.10	23.83	34.91	3.53	3.74	4.08	0.73	11.81	6.02	15.62	1+
22	55	FA	24.18	24.33	33.58	3.80	3.86	4.31	0.14	9.39	1.52	13.30	1+
23	58	Cyst	24.43	24.20	35.70	3.45	3.83	4.32	–0.22	11.26	11.07	25.18	1+
24	31	Abscess	22.20	22.85	30.98	3.73	3.80	4.37	0.65	8.78	1.83	17.12	1+
25	57	CA	26.51	26.92	34.83	4.14	4.33	4.56	0.40	8.31	4.51	10.02	2+

* CA=carcinoma, FA=fibroadenoma, Corr.=Correlation

The arrival time and energy level reportedly vary with breast sample thickness [53], and the correlation length of the aberration profile in breast tissue varies with age and body type [53-55]. It is therefore to be expected that the near-field phase-screen model is inaccurate, resulting in poor breast imaging when using the correlation-based method. It has also been reported that waveform distortion is severe and sidelobes are high for breast tissue, primarily because it is a highly refracting and heterogeneous medium [53, 56-58]. Therefore, adaptive sidelobe-reduction techniques, such as the GCF-weighting method investigated in the study, are of particular interest since they do not make any assumptions regarding the origin of the sidelobes. As shown in this chapter, application of the GCF-weighting method significantly improves the contrast and boundary definition for cyst and solid masses. We have also demonstrated that the GCF-weighting method is more effective than correlation-based methods in improving the quality of images obtained from ultrasonic breast imaging without the use of a 2D (or 1.5D) array.

(a)   (b)
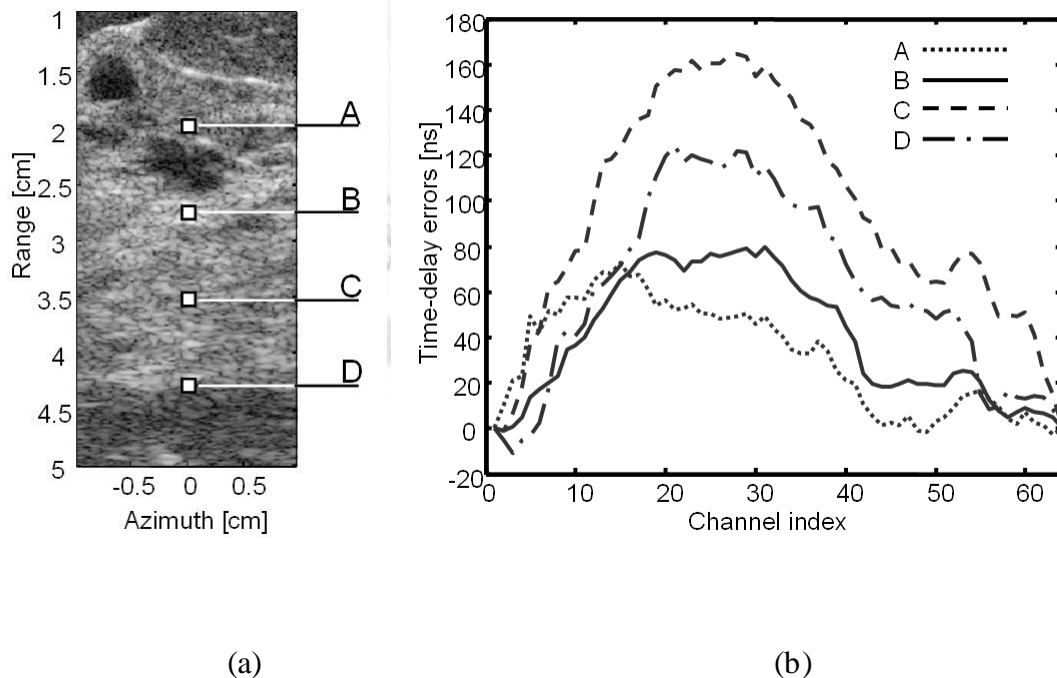
Fig. 3-10. Estimated time-delay errors. (a) Clinical image displayed with a dynamic range of 60 dB. (b) Corresponding estimated time-delay errors as functions of channel index at the imaging points indicated in (a).

This chapter has focused on reducing sidelobe components from imperfect focusing along lateral direction using 1D array. The presence of a 2D array can extend the method for reducing sidelobe components along elevational direction provided a sufficient elevationally spectral resolution (i.e., a sufficient large aperture size and number of channels along the elevational direction). The GCF can be estimated as the ratio within a certain low-frequency region of the k-space data to the total energy, where the k-space data are obtained by applying 2D discrete Fourier transform to all received channels at each time. For a 1.5D array (or an array without sufficient large aperture size and number of channels along the elevational direction), the GCF can be estimated from the channel data which are partial beamsumed along the elevational direction (as using a 1D array).

3.6 CONCLUDING REMARKS

In this chapter we have experimentally evaluated an adaptive imaging approach for reducing focusing errors in ultrasonic imaging. This method is based on coherence, and corrects focusing errors by suppressing unwanted sidelobes. The presented experimental results demonstrate that the image quality was noticeably improved in all of the cases investigated using a 1D array.

CHAPTER 4 COHERENCE WEIGHTING FOR HIGH-FRAME-RATE ADAPTIVE IMAGING

Some success has been demonstrated in the extensive studies of adaptive imaging, but these approaches are generally not suitable for high-frame-rate (HFR) imaging where broad transmit beams are required. In this study, we propose an effective adaptive imaging method suitable for HFR imaging based on CF weighting and the minimum-variance-distortionless-response (MVDR) method. The CF is an index of focusing quality estimated from receive-channel data in which the amplitude of each image pixel is weighted by the corresponding CF so as to reduce the unwanted sidelobes. Direct implementation of CF weighting in HFR imaging does not provide satisfactory results because the broad transmit beams required for HFR imaging reduce the accuracy of CF calculations. In this study, we alleviated this problem by applying the MVDR method. We test the proposed method with the synthetic transmit aperture method where only eight firings are required to form an image. Both simulations and clinical breast imaging data were used, and the results demonstrate that the proposed method is effective at improving the image quality.

This chapter is organized as follows: Sections 4.1 and 4.2 describe the basic principles of HFR imaging and the proposed method, respectively. Sections 4.3 and 4.4 present the simulation and experimental results, respectively, and the results are discussed and conclusions are drawn in Section 4.5.

4.1 HIGH FRAME RATE ULTRASOUND IMAGING

The round-trip propagation time fundamentally limits the acquisition time of each image frame in ultrasound imaging. To obtain images with a higher frame rate,

using a broad transmit beam with a parallel receive-beam formation is essential to effectively decrease the total number of firings and thereby shorten the acquisition time of each frame. A broad transmit beam can be generated using single-element firing, plane-wave excitation, a defocused beam, or a limited-diffraction beam on transmit. Although these methods can increase the frame rate many-fold, a broad transmit beam directly degrades both the spatial and contrast resolutions of the image. Furthermore, the SNR of the images is degraded due to the absence of transmit focusing.

A retrospective focusing method named the synthetic-transmit-aperture (STA) imaging technique [59] is introduced here to perform dynamic transmit focusing using the channel data from multiple firings. At each firing, all receive elements record the echoes from a transmit aperture that comprises either a single array element or a subaperture formed using multiple array elements. The recorded signals are then used to form low-resolution images according to each firing by applying receive focusing. Dynamic transmit focusing is then applied to all subimages according to the positions of the transmit apertures. Finally, a two-way dynamically focused image is synthesized by coherently summing all the beam formed subimages. The use of an STA improves the spatial resolution relative to that when using a single transmit element, and the SNR is also improved due to the use of coherent summing. One of the main drawbacks of the STA imaging method, the motion artifact [60], is a less serious problem for HFR imaging due to a short data acquisition interval.

4.2 Coherence-based Adaptive Imaging

Adaptive imaging techniques for sidelobe reduction have been studied extensively [11, 13, 16]. These methods estimate the energies contributed by the on-axis and off-axis components in the receive data. The estimated on-axis components are preserved and the off-axis components are suppressed in the resultant image. The CF method [13] is one of the sidelobe reduction methods. The CF is defined as Equation (1-14). Equation (1-14) estimates the CF value of the receive data with no beam steering. To estimate the CF value with steered beams, steering

vector a(θ) corresponding to the phase shift of each element across the entire N-element array is defined as

$$\mathbf{a}(\theta) = \begin{bmatrix} a_1(\theta) \\ a_2(\theta) \\ \vdots \\ a_N(\theta) \end{bmatrix} = \begin{bmatrix} 1 \\ e^{-jkd\sin\theta} \\ \vdots \\ e^{-(N-1)jkd\sin\theta} \end{bmatrix}, \tag{4-1}$$

where θ is the steering angle, the subscript of a is the element index, k denotes the wave number ($k = 2\pi/\lambda$, where λ is the wavelength), and d denotes the interelement spacing. The receive-beam sum data y for steering angle θ is

$$y(\theta,t) = \sum_{n=1}^{N} a_n(\theta) x_n(t) = \mathbf{a}(\theta)^H \mathbf{x}(t), \tag{4-2}$$

where the H superscript denotes the conjugate transpose operation, and the receive signals from all channels are represented by the vector x(t):

$$\mathbf{x}(t) = \begin{bmatrix} x_1(t) \\ x_2(t) \\ \vdots \\ x_N(t) \end{bmatrix}. \tag{4-3}$$

The relationship between receive signals among all channels and steering angle θ is illustrated in Fig. 4-1. The CF with beam steering is expressed as the ratio between the coherent energy after beam steering and the total incoherent energy:

$$CF(\theta,t) = \frac{\left| y(\theta,t) \right|^2}{\sum_{n=1}^{N} \left| x_n(t) \right|^2} = \frac{\left| \mathbf{a}^H(\theta)\mathbf{x}(t) \right|^2}{\sum_{n=1}^{N} \left| x_n(t) \right|^2}$$

$$= \frac{\mathbf{a}^H(\theta)\mathbf{R}_{xx}(t)\mathbf{a}(\theta)}{tr\{\mathbf{R}_{xx}(t)\}}, \tag{4-4}$$

where $tr\{\cdot\}$ denotes the trace operation, and $R_{xx}(t)$ is the spatial autocovariance matrix of the receive-channel data:

$$\mathbf{R}_{xx}(t) = \mathbf{x}(t)\mathbf{x}^H(t). \tag{4-5}$$
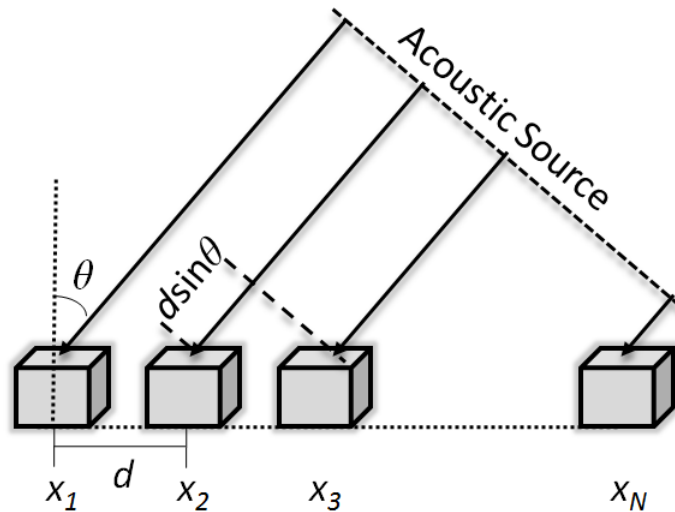
Fig. 4-1 Schematic diagram of the receive-channel data and the steering angle.

4.2.3 Capon Estimator (MVDR Method)

Beam formers conventionally use delay-and-sum operations to form receive beams. The associated apodization involves weighting the receive-channel data, with the receive-beam data being obtained by summing across the channels. Apodization function can be viewed as spatial filtering to control the width of the mainlobe and amplitudes of the sidelobes (i.e., beam shaping).

An adaptive beam formation approach using adaptive weighting has been proposed by Capon [61]. The weighting for each channel is chosen to minimize the output power of the array subject to the constraint that the array gain must be unity in the desired beam direction. Capon's method is also known as the MVDR method. Optimization of the array weights can be formulated as

$$
\min_{w(t)} \mathbf{w}^H(t)\mathbf{R}_{xx}(t)\mathbf{w}(t),
$$
$$
\text{subject to } \mathbf{w}^H(t)\mathbf{a} = 1,
\tag{4-6}
$$

where $\mathbf{w}$ denotes the weighting vector, and steering vector $\mathbf{a}$ is a unity vector for cases where focusing delays have been applied previously. Then, the optimum weighting solution of (4-7) becomes

$$
\mathbf{w}_{\text{MVDR}}(\theta, t) = \frac{\mathbf{R}_{xx}^{-1}(t)\mathbf{a}(\theta)}{\mathbf{a}^H(\theta)\mathbf{R}_{xx}^{-1}(t)\mathbf{a}(\theta)}.
\tag{4-7}
$$

where the $\{\cdot\}^{-1}$ denotes the matrix inverse operation. The array output power $P(\theta, t)$ for a particular weighting vector is

$$
P(\theta, t) = \mathbf{w}(\theta, t)\mathbf{R}_{xx}(t)\mathbf{w}(\theta, t).
\tag{4-8}
$$

Combining (4-7) and (4-8) yields the estimated array output power along the steered beam using the MVDR weighting:

$$
P_{\text{MVDR}}(\theta, t) = \mathbf{w}_{\text{MVDR}}^H(\theta, t)\mathbf{R}_{xx}(t)\mathbf{w}_{\text{MVDR}}(\theta, t)
$$

$$
= \frac{1}{\mathbf{a}^H(\theta)\mathbf{R}_{xx}^{-1}(t)\mathbf{a}(\theta)}.
\tag{4-9}
$$

This output power can be used for high-resolution angle-of-arrival estimation. As a comparison, the estimated output power of the aforementioned steered beam method is

$$P(\theta, t) = \left| y(\theta, t) \right|^2 = \mathbf{a}^H(\theta) \mathbf{R}_{xx}(t) \mathbf{a}(\theta) . \tag{4-10}$$

4.2.4 Adaptive Imaging Using the CF and MVDR

Broad transmit beams are used in HFR imaging to increase the frame rate. On the other hand, aberration correction techniques rely on the coherence of the receive data and hence need a focused beam (i.e., a narrow beam) on transmit. Therefore, aberration correction is more challenging in HFR imaging using broad transmit beams due to the degraded coherence and reduced SNR. As a consequence, a coherence-based method with high spectral resolution was explored in this study to estimate the coherence when imaging using broad transmit beams. In our method, spectral estimation as described in (4-9) is used to estimate the coherent energy of the receive data, and the CF estimation in (4-4) is modified to

$$\mathrm{CF}_{\mathrm{MVDR}}(\theta, t) = \frac{P_{\mathrm{MVDR}}(\theta, t)}{\sum_{n=1}^{N} \left| x_n(t) \right|^2} = \frac{1}{\mathbf{a}^H(\theta) \mathbf{R}_{xx}^{-1}(t) \mathbf{a}(\theta)} \frac{1}{tr\left\{ \mathbf{R}_{xx}(t) \right\}} . \tag{4-11}$$

Hence, CF estimation with a high spectral resolution and low sidelobes is possible.

In practice, since the noise is unknown, the estimated R_{xx} also varies rapidly with time. The robust estimation of R_{xx} requires temporal or spatial averaging, which is also beneficial when estimating at low SNRs resulting from the use of broad transmit beams. Good estimates are obtained using spatial averaging with data blocks of length K. The K-length block of sampled data is

$$\mathbf{x}_K(t) = \begin{bmatrix} x_1(t-K/2) & x_1(t-K/2+1) & \cdots & x_1(t+K/2-1) \\ x_2(t-K/2) & x_2(t-K/2+1) & & x_2(t+K/2-1) \\ \vdots & \vdots & \ddots & \vdots \\ x_N(t-K/2) & x_N(t-K/2+1) & & x_N(t+K/2-1) \end{bmatrix}, \qquad (4\text{-}12)$$

and the corresponding estimated R_{xx} is

$$\hat{\mathbf{R}}_{xx}(t) = \frac{1}{K} \mathbf{x}_K(t)\mathbf{x}_K^H(t), \qquad (4\text{-}13)$$

where K is the corresponding block length. $\hat{\mathbf{R}}_{xx}$ in (4-12) can be used to estimate the on-axis energy component more robustly, but this degrades the resultant spatial resolution due to spatial averaging. Therefore, selecting the optimal value of K requires an appropriate trade-off.

Diagonal loading can also be used to improve the robustness of the method. This involves adding a constant ε to all the diagonal elements of $\hat{\mathbf{R}}_{xx}$ before estimating (4-11):

$$\hat{\mathbf{R}}_{xx}(t) = \hat{\mathbf{R}}_{xx}(t) + \varepsilon \mathbf{I}, \qquad (4\text{-}13)$$

where $\mathbf{I}$ is the $N \times N$ identity matrix. Since the matrix inversion is performed with all the estimated autocovariance matrices, diagonal loading can prevent errors when $\hat{\mathbf{R}}_{xx}$ is not a full-rank matrix [62]. The addition of diagonal loading is analogous to adding spatial white noise to the receive signals, so ε should be chosen appropriately based on the intensity of the receive data. In this study, the chosen ε was proportional to the total incoherent energy of the receive signal:

$$\varepsilon = \Delta \cdot tr\{\mathbf{R}_{xx}(t)\}, \qquad (4\text{-}15)$$

where Δ is a prespecified constant.

Scattering effects also need to be taken into account to improve the robustness of coherence estimation. Previous studies have found that the signals from homogeneous scatterers are not totally coherent [16, 17]. Scattering affects the amplitude and phase of the receive-channel data and broadens the estimated intensity laterally. Therefore, estimating the coherent energy from scatterers requires consideration of both the on-axis component and the distributed energy caused by scattering effects:

$$\text{CF}_{\text{MVDR}}(t) = \left(\sum_{\theta_i} \frac{1}{\mathbf{a}^H(\theta_i)\hat{\mathbf{R}}_{xx}^{-1}(t)\mathbf{a}(\theta_i)} \right) \frac{1}{tr\{\hat{\mathbf{R}}_{xx}(t)\}}, \qquad (4\text{-}16)$$

where θ_i is the prespecified steering angle around the beam direction, and should be chosen to cover the energy distribution resulting from scattering [16, 17]. Since the spatial resolution is higher for the Capon estimator than for the conventional spectral estimator (4-8), the spacing between adjacent θ_i's should be narrower than the conventional one. However, since the computational complexity increases in proportional with the total number of θ_i's, their number should also be selected based on a trade-off between accuracy and computational complexity. In practice, the spacing is chosen according to $\Delta \sin(\theta_i) = \frac{1}{4N}$.

Fig. 4-2 shows a schematic diagram of the signal processing procedures employed in this study. After the echo signals are received and digitized by the A/D converter, the received RF data are demodulated down to baseband and the baseband beam former applies geometric focusing delays and phase rotations to the baseband data. The B-mode image is then obtained by summing the beam across the array with prespecified apodization. The value of CF_{MVDR} is estimated using the delayed baseband data across the aperture at all ranges prior to beam summation. Note that a baseband beam former is necessary for estimating CF_{MVDR}. The amplitude of the beam sum is then simply multiplied by the corresponding CF_{MVDR}:

$$y_{\text{weighted}}(\text{t}) = \text{CF}_{\text{MVDR}}(t) \cdot y(t), \qquad\qquad (4\text{-}17)$$

where y denotes the amplitude of the beam-sum data, and y_{weighted} denotes the amplitude of the beam sum weighted by CF_{MVDR}. The weighted beam-sum data are then stored in a buffer for further signal processing, scan conversion, and display.
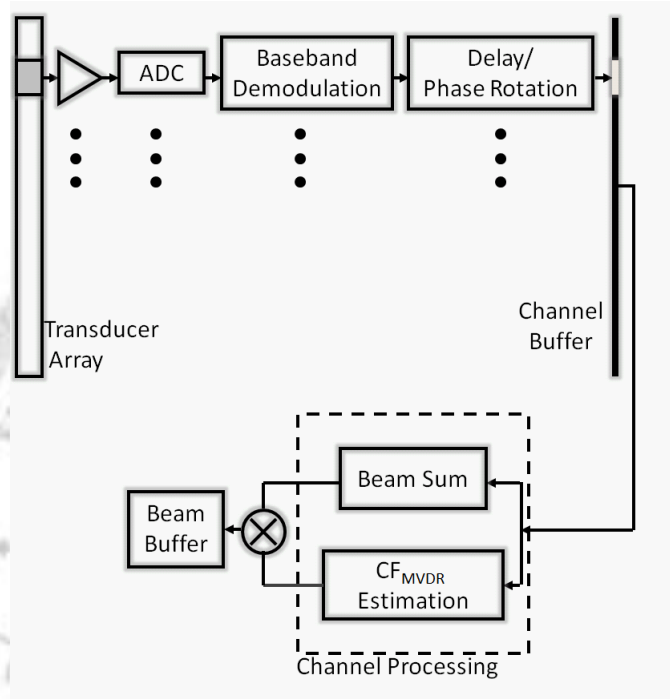
Fig. 4-2. Schematic diagram of the signal processing of the proposed technique.

4.3 SIMULATION INVESTIGATION

Simulated ultrasound data were used to test the efficacy of the proposed technique. The acoustic-field simulation program Field II [50] was used to generate receive-channel data for each element. In the simulations, the array transducer was a 128-element linear array with a center frequency of 5 MHz and a pitch of 0.3 mm.

4.3.1 Capon Estimator for a PointTtarget

Simulated data were used to test the efficacy of the Capon estimator (4-9) with broad transmit beams. Plane-wave excitation (i.e., no relative transmit delays among transmit elements) with Hamming apodization was applied. Only the central 64 elements of the transducer were used to generate the transmit beam. The receive-channel data (i.e., the recorded signal from each channel after the application of geometrical delays prior to beam summation) were generated and used to estimate the spatial energy distribution. Fig. 4-3 shows the relationship between the receive-channel data of the central 64 elements and the energy distributions estimated using the different methods. The results using the Capon estimator (4-9) are compared to those using the conventional estimator (4-10). The first column of Fig. 4-3 shows the receive-channel data, where the vertical axis represents the range and the horizontal axis represents the channel index. The second column of Fig. 4-3 shows the energy distribution estimated using the conventional estimator (4-10), where the vertical axis represents time and the horizontal axis represents the beam spacing in $\sin(\theta)$ from $-1/5$ to $1/5$. The third column of Fig. 4-3 shows the energy distribution estimated using the Capon estimator (4-11) with both axes defined as in the second column. The fourth column shows the lateral projection of the estimated energy distribution for the conventional and Capon estimators, where the vertical axis represents the intensity (on a logarithmic scale) and the horizontal axis represents the beam spacing. The top panels of Fig. 4-3 show the channel data and the estimated energy for a point target located at a range of 5 cm from the transducer. The receive-channel data are in-phase along the channels in this case. The estimated energy distributions show that the mainlobe is narrower and the sidelobes are lower for the Capon estimator than for the conventional method due to the minimization of interferences, and hence the Capon estimator produces a more selective spatial energy distribution. The middle panels of Fig. 4-3 shows the channel data and the estimated energy for a point target that has moved 1° from the beam direction, which emulates a steering error. Again the estimation using the Capon estimator has a narrower mainlobe and lower sidelobes. The bottom panels of Fig. 4-3 show the channel data

and the estimated energy for a point target located at 6 cm when the receive focal point is located at 5 cm from the transducer, which emulates a range focusing error. The results show that the energy obtained using the Capon estimator is concentrated in the beam direction while the energy estimated using the conventional method spreads laterally. Fig. 4-3 clearly demonstrates the advantages of using the Capon estimator to estimate the spatial energy distribution for a point target.
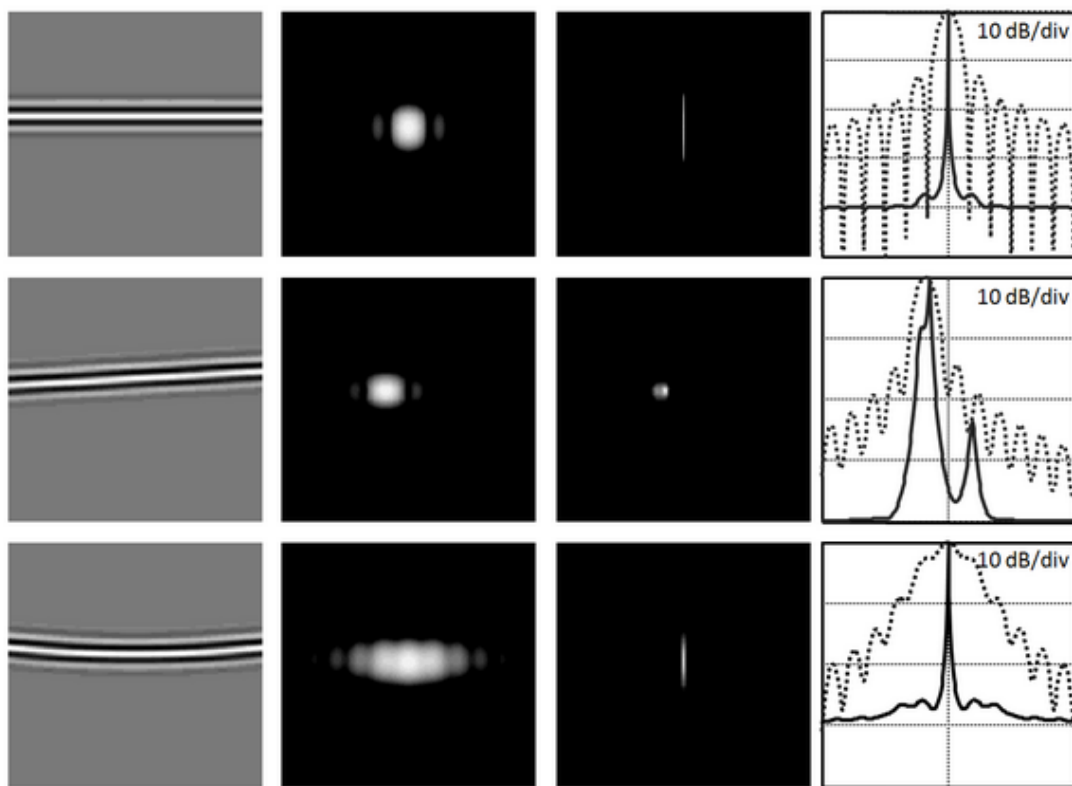
Fig. 4-3. Channel data and the corresponding spectra over the aperture for a point target using a broad transmit beam. The top panels correspond to ideal focusing, the middle panels have a steering error, and the bottom panels have a range focusing error. The first column shows the channel data with the horizontal and vertical axes representing the channel index and the range, respectively. The second and third columns show the spectra estimated using (4-10) and (4-16), respectively. The fourth column shows the projections of the estimated spectra.

4.3.2 Capon Estimator for a Speckle-generating Target

The feasibility of using the Capon estimator to assess the spatial energy distribution was also tested with speckle-generating targets. Since scattering occurs in most clinical situations, an adaptive imaging technique should also be robust in the presence of speckle-generating targets. Simulations were performed to test the proposed method with broad transmit beams and diffuse scatterers. Plane-wave excitation with Hamming apodization was again applied using only the central 64 elements of the transducer. Fig. 4-4 shows the channel data of the speckle-generating targets and the corresponding energy distribution. The effects of phase aberrations are also shown in the figure. The first column shows the receive-channel data from
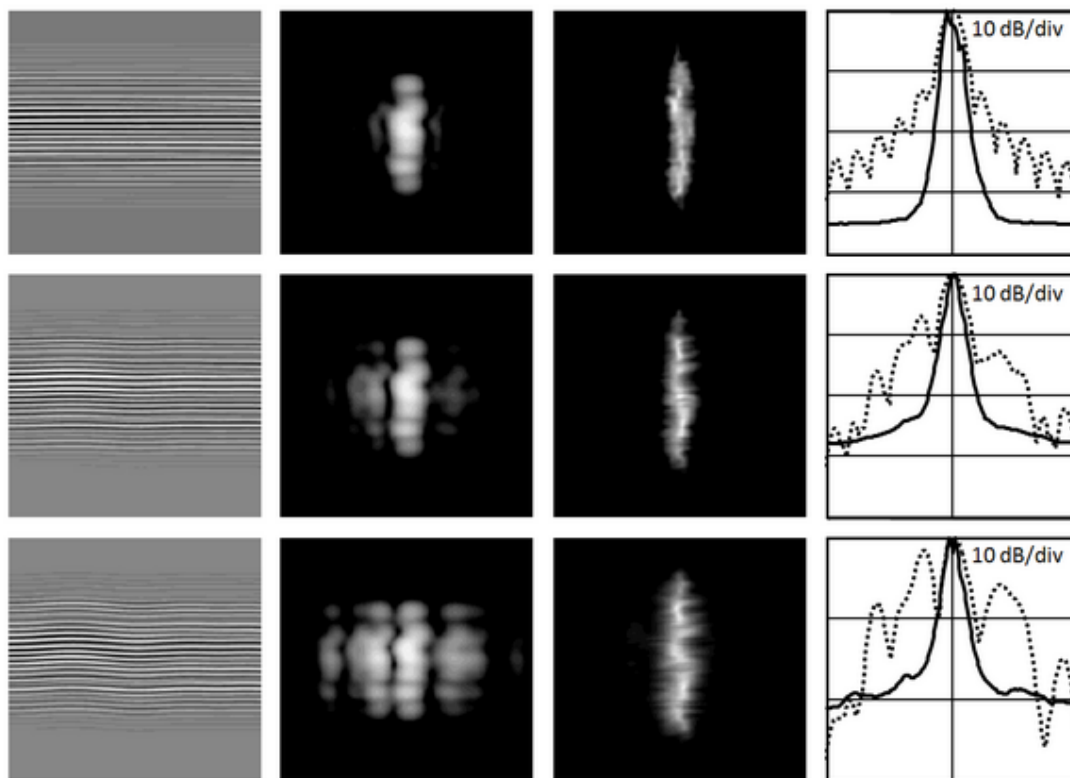
Fig. 4-4. Channel data and the corresponding spectra over the aperture for a speckle-generating target using a broad transmit beam. The top panels correspond to ideal focusing, the middle panels have a maximum phase error of $\pi/4$, and the bottom panels have a maximum phase error of $\pi/2$. The first column shows the channel data with the horizontal and vertical axes representing the channel index and the range, respectively. The second and third columns show

the spectra estimated using (4-10) and (4-16), respectively. The fourth column shows the projections of the estimated spectra.

speckle-generating targets, the second and third columns show the energy distributions estimated using the conventional and Capon estimators, respectively, and the last column shows the lateral projection of the estimated energy distribution. For each panel in Fig. 4-4, both the axial and lateral axes are defined as in Fig. 4-3. The top panels show the case with perfect focusing, and the middle and bottom panels show the cases with maximum phase aberrations of $\pi/4$ and $\pi/2$, respectively. In general the energy distribution is broader for speckle-generating targets than for a point target, which is due to the effects of scattering. Again, estimation using the Capon estimator produces better spatial resolution and lower sidelobes. Therefore, the results demonstrate that the Capon estimator is robust to the direction of the insonifying energy from diffuse scatterers and is feasible for estimations made using broad transmit beams.

4.3.3 Aberration Correction for a Simulated Anechoic-cyst Phantom

The feasibility of using the CF_{MVDR} method to correct phase aberrations was further tested with an anechoic-cyst phantom containing speckle-generating targets. The center of an anechoic cyst with a radius of 5 mm was located at a depth of 5 cm, and the cyst was surrounded by speckle-generating targets. The dimension of the phantom was 3 cm in both the lateral and axial directions. The STA method was used to improve the image quality of the obtained HFR image. An HFR image was two-way dynamically focused using the synthesized receive data from eight different transmit apertures, each of which consisted of eight adjacent elements. Phase aberrations were corrected using the correlation-based method proposed by Flax and O'Donnell [3, 4] and the technique proposed in this study. Fig. 4-5 shows the images of the simulated anechoic-cyst phantom and those with phase aberrations. The figure also shows the corrected results obtained using the proposed method and the correlation-based method. The top panels show the anechoic cyst with ideal focusing, and the middle and bottom panels show the cysts with maximum phase errors of $\pi/4$ and $\pi/2$,
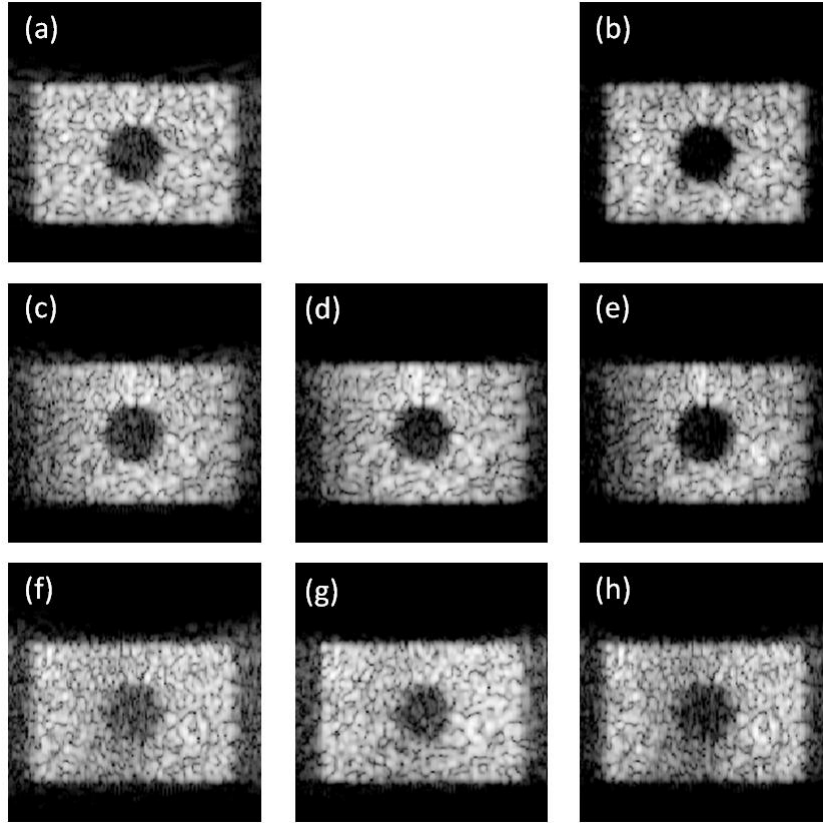
Fig. 4-5. Original and corrected images of a phantom containing an anechoic cyst displayed with a dynamic range of 45 dB. The left panels show the uncorrected image, and the middle and right panels show the images corrected obtained using the correlation-based method and the proposed method. (a) and (b) No aberration. (c)–(e) Maximum phase error of $\pi/4$ at the imaging frequency of 5 MHz. (f)–(h) Maximum phase error of $\pi/2$.

respectively. The left panels show the original images, and the middle and methods, respectively. The CR and the CNR were used to evaluate the improvement in image quality. The CR and CNR are defined in Section 3. The results listed in Table 4-1 indicate that the proposed method can improve the CR and CNR by 10.1 dB and right panels show the images corrected using the correlation-based and proposed 43.3%, respectively. When imaging the same cyst with phase aberrations, the CR improvements when using the proposed and correlation-based methods were 3.12 dB and 7.89 dB, respectively, when the maximum phase error was $\pi/4$, and 4.34 dB and 5.59 dB when the maximum phase error was $\pi/2$; the corresponding CNR improvements were 14.34% and 36.28% for a maximum phase error of $\pi/4$, and

22.84% and 29.42% for a maximum phase error of $\pi/2$. The contrast improvement is greater and the margin is clearer for the proposed method based on adaptive sidelobe reduction than for the correlation-based method.

Table 4-1. CR and CNR values for images of a simulated phantom containing an anechoic cyst.

CR (dB)	Original image	Correlation-based method	Proposed method
No aberration	23.31		33.41
Maximum aberration of $\pi/4$	21.75	24.87	29.64
Maximum aberration of $\pi/2$	19.00	23.34	24.59
CNR	Original image	Correlation-based method	Proposed method
No aberration	4.41		5.65
Maximum aberration of $\pi/4$	4.02	5.05	5.36
Maximum aberration of $\pi/2$	3.70	4.49	4.65

4.4 EXPERIMENTAL INVESTIGATION

4.4.1 Experimental Setups

Experiments were also performed to test the efficacy of the proposed method in clinical breast imaging. Clinical female breast data were collected at the Taipei Veterans General Hospital with assistance from Dr. Y.-H. Chou and with the patients' consent. A schematic diagram of the experimental setup is shown in Fig. 4-6. The experimental setup is identical to that in Section 3.
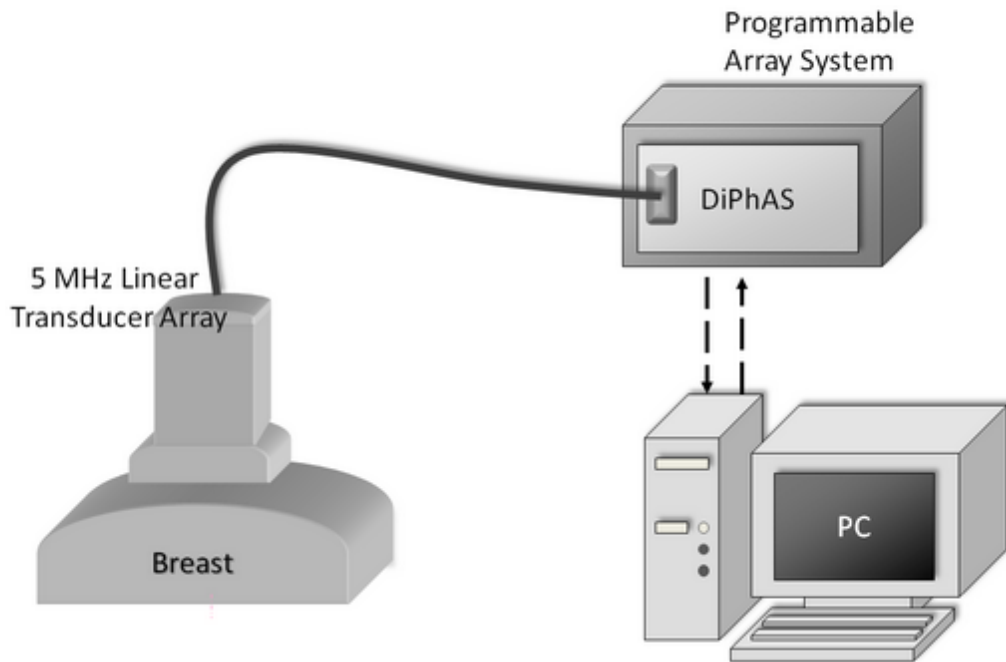
Fig. 4-6. Schematic diagram of the experimental setup.

The STA method was used to obtain high-quality HFR images. An HFR image was two-way dynamically focused using the synthesized receive data for different transmit apertures. Each transmit aperture generally consisted of eight adjacent elements. In other words, the total number of active transmit elements was 16, 32, and 64 for 2, 4, and 8 firings, respectively. The only exception was when the number of firings was 64, in which case a transmit aperture consisting of 2 elements was used. An f-number of 1

was applied to control the receive aperture. Fig. 4-7 shows how the number of firings affected the image quality. For images using only two or four firings, the insonified energy was concentrated in the central region of the image, and visualization of the lesion was poor since the full field of view was not illuminated. When using eight or more firings the insonified energy was sufficient for imaging. Furthermore, the FWHMs (full widths at half maximum) of the autocovariance function of the imaging object were 1.99 mm, 1.91 mm, 1.77 mm, and 1.75 mm when using 2, 4, 8, and 64 firings, respectively. The results demonstrate that using eight firings represents a good compromise between the image acquisition time and image quality.
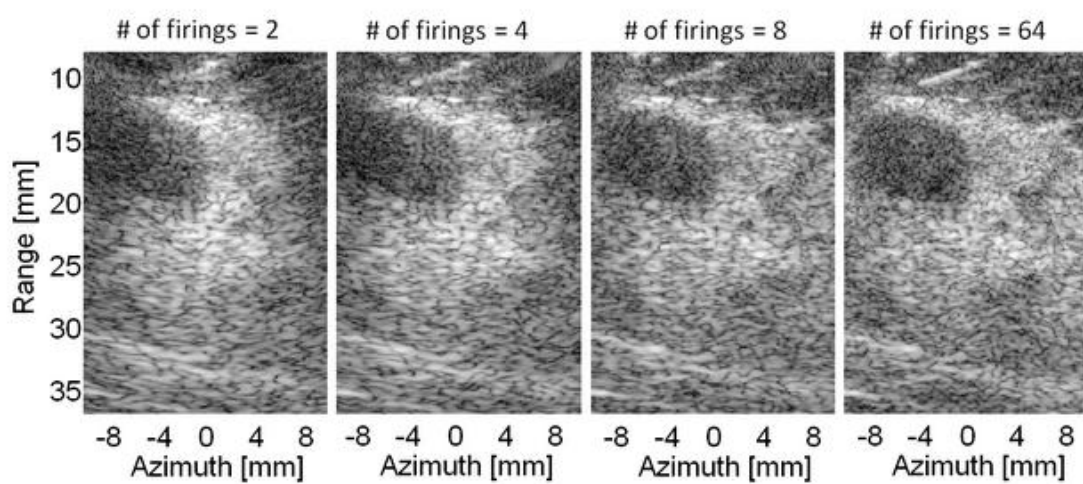
Fig. 4-7. Comparisons of the effects of different number of firings for the STA method.

4.4.2 Fibroadenoma

Fig. 4-8 shows images of a fibroadenoma lesion in a 42-year-old female patient. Fig. 4-8(a) is the conventional B-mode image obtained using a focused transmit beam, and Fig. 4-8(b) is the conventional image obtained using the correlation-based method [3, 4]. Fig. 4-8(c) shows the original HFR image, and Fig. 4-8(d) shows the corrected image obtained using the proposed method. The CRs and CNRs were 15.25 dB and 2.42, respectively, for the original image, and 20.10 dB and 2.97 for the image obtained using the proposed method. The improvements in CR and CNR were 4.84 dB and 22.56% with the proposed method, respectively. In addition, the poor

boundary definition in the original image was noticeably improved using the proposed method, as was the contrast. For Fig. 4-8(a) and Fig. 4-8(b), the CRs and CNRs were 15.87 dB and 2.59, respectively, for the conventional B-mode image, and 16.18 dB and 2.61 for the image obtained using the correlation-based method. The results demonstrate that the proposed method can improve the contrast resolution for HFR imaging even more than the correlation-based method for conventional imaging.
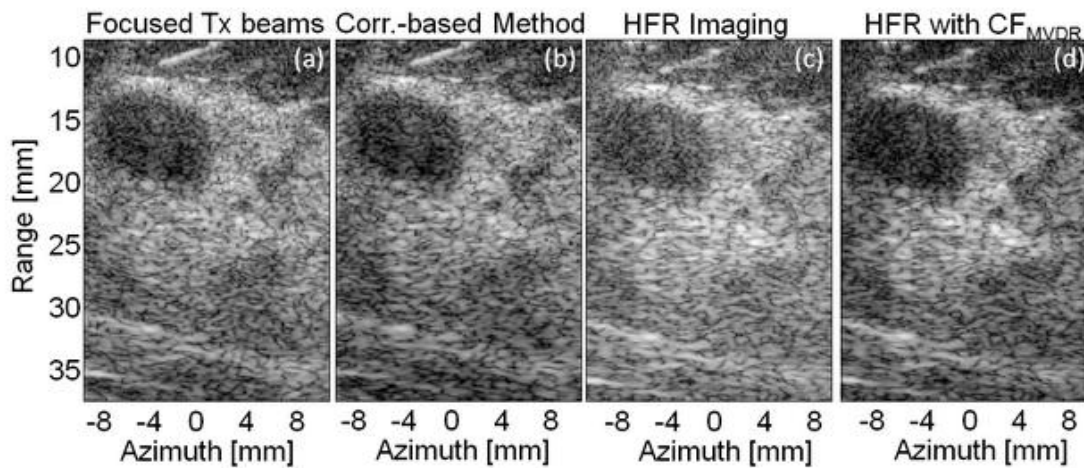
Fig. 4-8. Images of a fibroadenoma in a 42-year-old woman displayed with a dynamic range of 50 dB. The vertical and horizontal axes represent the range and azimuth, respectively. (a) Conventional B-mode image with focused transmit beam. (b) Conventional image obtained using the correlation-based method. (c) HFR B-mode image. (d) HFR image obtained using the proposed weighting method.

4.4.3 Carcinoma

Fig. 4-9 shows images of a carcinoma lesion in a 63-year-old female patient. Fig. 4-9(a) shows the original image, and Fig. 4-9(b) shows the corrected images obtained using the proposed weighting method. The CRs and CNRs were 9.58 dB and 1.76, respectively, for the original image, and 12.41 dB and 2.07 for the image obtained using the proposed method. The improvements in CR and CNR were 2.82 dB and 17.57% with the proposed method, respectively. Again, the original image shows an indistinct lesion margin, and the internal echo texture and several echogenic foci

76

indicating microcalcifications within the breast parenchyma are not clear. The image obtained using the proposed method shows better characterization of the margin, and enhances the conspicuity of microcalcifications within the breast parenchyma due to the improved resolution of the MVDR method.
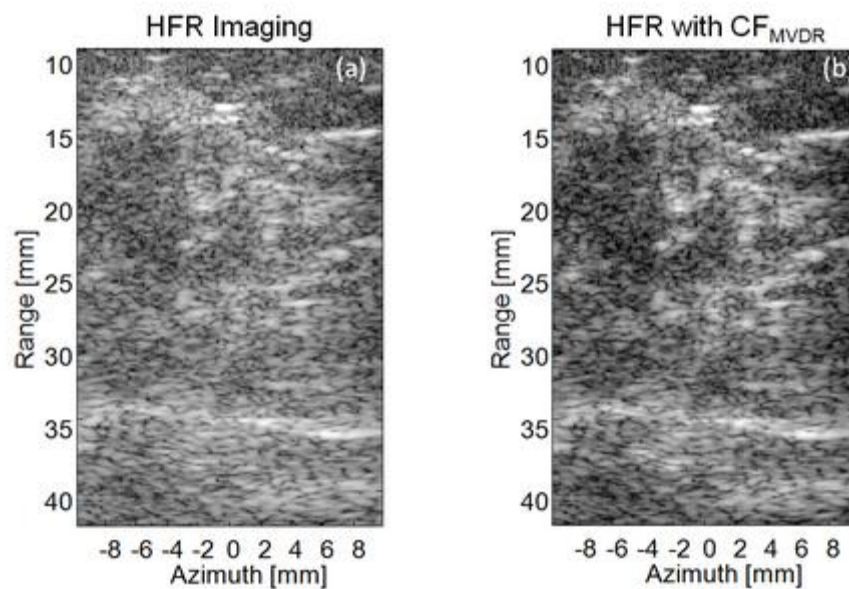
Fig. 4-9. Images of a carcinoma in a 63-year-old woman displayed with a dynamic range of 50 dB. The vertical and horizontal axes represent the range and azimuth, respectively. Microcalcifications are evident in the breast parenchyma region from 1.3 cm to 3.2 cm in depth and from −0.1 mm to 0.8 mm in azimuth. (a) Original B-mode image. (b) Image obtained using the proposed weighting method.

4.4.4 Cyst

Fig. 4-10 shows images of a cyst in a 66-year-old female patient. Fig. 4-10(a) shows the original image, and Fig. 4-10(b) shows the corrected images obtained using the proposed method. The CRs and CNRs were 21.22 dB and 3.41, respectively, for the original image, and 27.32 dB and 4.11 for the image obtained using the proposed method. The improvements CR and CNR were 6.10 dB and 20.43% with the proposed method, respectively. The original image shows an indistinct internal echo texture within the cystic mass, whereas the image obtained using the proposed method

shows the effective suppression of echo signals within the cystic mass and an enhanced contrast between the lesion and the background. Moreover, the margin of the cyst was more distinct than in the original image, indicating that both contrast and boundary definition were improved in this case.
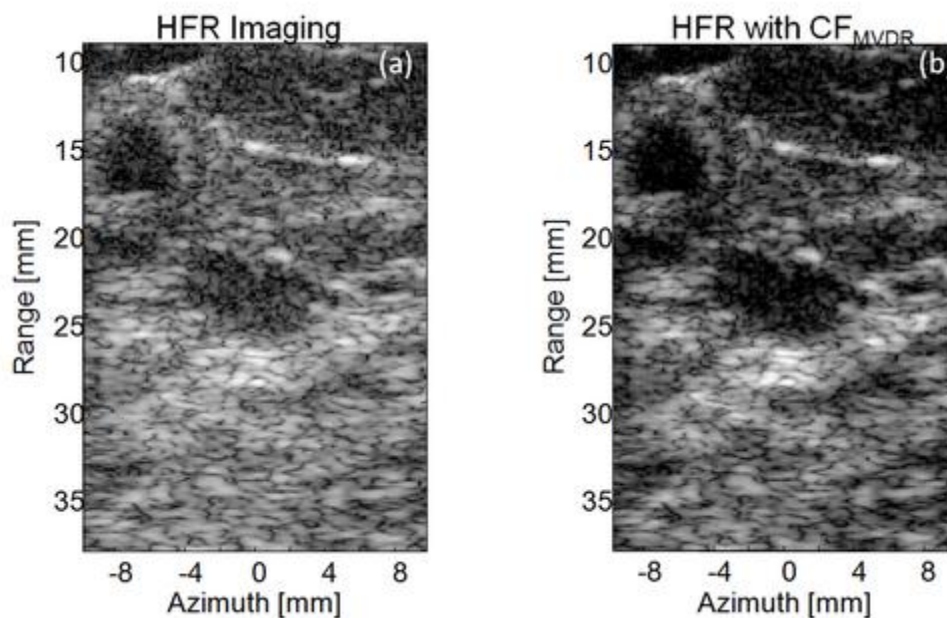
Fig. 4-10. Images of a cyst in a 66-year-old woman displayed with a dynamic range of 50 dB. The vertical and horizontal axes represent the range and azimuth, respectively. (a) Original B-mode image. (b) Image obtained using the proposed weighting method.

4.5 DISCUSSION AND CONCLUDING REMARKS

Adaptive beam forming techniques such as the MVDR method have recently been applied to ultrasound imaging [62, 63]. Due to the minimization of the interference power, adaptive beam forming techniques can narrow the beam width of the mainlobe and effectively suppress the sidelobes. Therefore, such adaptive beam forming methods have the potential of achieving both high spatial and contrast resolutions. These advantages have prompted great interest in the use of the MVDR method for HFR imaging. Although the MVDR method is very suitable for point-like targets, the method needs a more robust estimation of the autocovariance matrix for

speckle-generating targets. In this study, (4-13) and (4-16) were used to improve the robustness for the MVDR method in imaging speckle-generating targets. The *K*-length block approach (i.e., (4-13)) was used for spatial averaging to improve the robustness of the autocovariance matrix estimation. In this study the block length *K* was 4 times the wavelength. Another existing method to improve the robustness of the autocovariance matrix estimation is the subaperture method [62]. Also the CF is estimated not only along the beam axis but also the adjacent steering angles (i.e., (4-16)). This approach was previously used to improve the coherence estimation for speckle-generating targets [16]. The present chapter has demonstrated that the approach can also improve CF_{MVDR} estimation for speckle-generating targets.

In this study, we utilized the high spatial and contrast resolutions provided by the MVDR method in CF estimation. The processing for the proposed method involves weighting each image point with the corresponding CF. Unlike the adaptive beam forming method that weights the aperture domain data as spatial filtering, the proposed method weights the estimated CF on each image point and also reduces the computational complexity compared to the adaptive beam forming method.

The STA was used in this study to improve the quality of HFR imaging. For HFR imaging systems using broad transmit beams, image distortions including warping and skewing [64] manifest from misalignment between the transmit and receive beams. The STA method can improve image quality by utilizing synthesized transmit focusing, and improve the SNR for low-resolution images. Although the use of more firings to synthesize a larger transmit aperture can improve image quality, the data acquisition time needs to remain sufficiently short to avoid motion artifacts. The use of only eight firings in this study to synthesize an image represented a good compromise between image quality and data acquisition time. Note that although the STA was used in this study to improve image quality, the STA is not essential to the proposed method; that is, the proposed method is also suitable for HFR imaging without the STA. As described in Sections III-A and III-B, the MVDR method can estimate the on-axis component with high accuracy without applying the STA method.

Nonetheless, the two-way dynamic focusing applied by the STA method can further improve CF estimation due to the higher coherence resulting from transmit focusing.
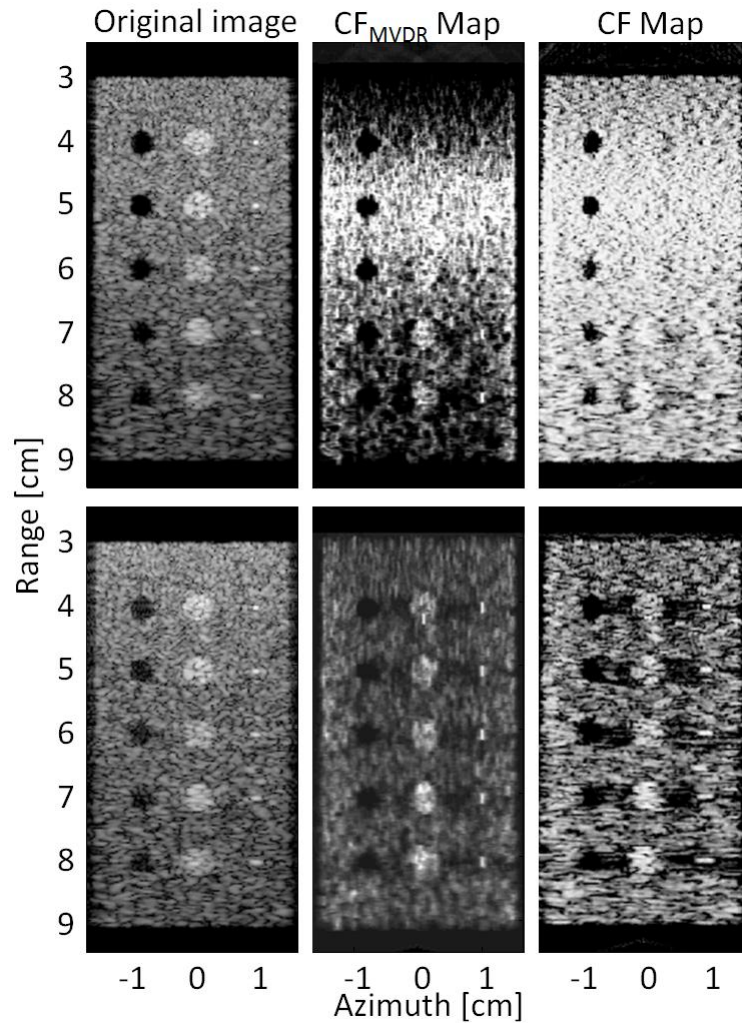
Fig. 4-11. Images of a phantom and their corresponding CF maps. The left panels are the original images obtained using a fixed focal depth of 5 cm on transmit and dynamic receive focusing, and are displayed with a dynamic range of 50 dB. The middle and right panels are the CF maps estimated using the MVDR method and a previously reported method [16, 17], respectively, and are displayed with a dynamic range of 30 dB. Each beam in the upper panels was formed with an aperture size of 64 elements on both transmit and receive. Each beam in the lower panels was formed with aperture sizes of 8 elements on transmit and 64 elements on receive.

This study focused on correcting phase aberrations in HFR ultrasound imaging, but the proposed method can also be applied to conventional imaging system with

focused transmit beams. This corresponding results are illustrated in Fig. 4-11. The left panels of Fig. 4-11 show images formed with a fix transmit focal depth of 5 cm and with dynamic receive focusing. The middle and right panels are the corresponding CF maps estimated using the proposed MVDR method and a previously reported method [16], respectively. The upper panels show the results for transmit and receive apertures with 64 elements, and the lower panels show the results using 8 elements for the transmit aperture and 64 elements for the receive aperture. The upper and lower panels indicate the images obtained using narrow and broad transmit beams, respectively. The results demonstrate some drawbacks when applying the proposed method to ultrasound imaging with focused transmit beams. First, the contrast near to the focal depth is similar to that for the conventional method. Moreover, the estimated coherence degrades rapidly away from the focal point. When imaging using broad transmit beams, on the other hand, the MVDR method can improve CF estimation especially with a point-like target. Also, the MVDR method has considerably higher computational requirements. Therefore, it is preferable to use the conventional method for CF estimation in conventional imaging with focused beams.

In conclusion, this chapter proposes an adaptive technique based on the CF and the MVDR method to reduce focusing errors in HFR ultrasound imaging, especially those resulting from sound-velocity inhomogeneities. The proposed method was evaluated using both simulation and experimental data, with the results demonstrating that it is effective in HFR imaging applications.

CHAPTER 5 CONCLUSIONS AND FUTURE WORKS

5.1 CONCLUSIONS

In this thesis, several aperture domain processing techniques, including vector velocity estimation and the adaptive imaging techniques for both conventional and high-frame-rate imaging have been proposed. Feasibilities of these methods were demonstrated using simulation and experimental results. Moreover, these methods can improve the imaging system using 1D arrays and can be further extended to systems using 2D arrays. In chapter2, the proposed vector velocity estimation method can not only estimate the lateral velocity component but also improve the accuracy of the axial velocity estimation over the conventional flow estimation technique. The mean estimation error for the axial velocity component is 2.18% for the new method, compared to 4.51% for the conventional method. The mean estimation error for the lateral velocity component is 15%, which is comparable to existing methods Furthermore, a subaperture method is introduced to improve the performance of flow estimation at low SNRs.

The proposed adaptive imaging techniques can effectively correct focusing errors resulting from sound-velocity inhomogeneities and improve the contrast of the image. Adaptive imaging using sidelobe-reduction techniques, such as the coherence-based weighting methods investigated in Chapters 3 and 4, are of particular interest since these techniques do not make any assumptions regarding the source of the sidelobes. In chapter 3, Relative to nonweighted imaging, the average improvements in the contrast ratio and contrast-to-noise ratio for the coherence-based method were 8.57 dB and 23.2%, respectively, whereas the corresponding improvements when using the correlation-based method were only 0.42 dB and 3.35%. In chapter 4, we tested the proposed method with the STA method where only eight firings are required to form an image. Both simulations and clinical breast

imaging data were used, and the proposed method enhanced the mean contrast by around 4.6 dB and the mean contrast-to-noise ratio by around 20%. The feasibility of the coherence-based weighting method in improving image quality without the use of a 2D (or 1.5D) array was demonstrated.

5.2 FUTURE WORKS

Future works include further performance investigation on the application of aperture domain data processing in clinics and an efficient implementation of the aperture domain processing techniques.

5.2.1 Vector Flow Estimation

From the results of Chapter 2, it is concluded that real-time two-dimensional estimation of the vector velocity using the aperture domain data is feasible. Future works will extend the proposed method to *in-vivo* experiments and take into account the influence of physiological motion artifacts. Furthermore, the flow estimation method can improve the imaging system using 1D arrays and can be further extended to the systems using 2D arrays for 3D vector velocity estimation. Also, combining the STA method can increase the imaging frame rate up to the pulse repetition frequency [65, 66] . STA imaging gives the possibility to acquire an image with only few emissions and is appealing for 3D ultrasound imaging. In STA imaging, it is possible to focus the receive data in any direction. The 2D vector velocity estimation within the imaging plane can be achieved using a limited number of flow samples since the transmission is spherical and illuminates the full region of interest. Though the number of emissions is low, the change in position of the scatterers leads to distortions in the image. In order to develop velocity estimation methods a further investigation of the nature of motion artifacts is needed. Previous study has shown that correlation between the image frames are high and it is possible to achieve high accuracy flow estimation with STA [67]. Also STA can improve the proposed velocity vector estimation technique in clutter filtering and reducing estimation errors

method and is less affected by physiological motion artifact. Thus, this can be used to devise a high accuracy full vector velocity imaging system.

5.2.2 Microcalcification Detection in Breast Ultrasound

The appearance of microcalcifications in sonography is an important indicator of early breast cancer. Microcalcifications are calcium deposits and are identified as tiny areas slightly brighter than the surrounding tissue. Detection of microcalcification has been performed in clinics to help the diagnosis of the breast tumor malignancy. There are five characteristics of calcifications (morphology, size, distribution, number, and location) described in morphology of breast microcalcifications, and the predictive value for malignancy varies with the classification type [68, 69]. Detection of microcalcifications using ultrasound has not been successful. The general clinical experience shows that the image noise results in unreliable diagnosis. The presence of microcalcifications cannot be positively identified from noise due to similar image characteristics. The acoustic properties of microcalcifications such as spatial coherence of echoes from microcalcifications are currently of interest [70]. Previous simulation results (as shown in the middle panels of Fig. 4-11) have demonstrated that the CF_{MVDR} method can enhance point-like-targets without using a strong transmit focusing. This implies the feasibility to enhance microcalcifications using the proposed CF_{MVDR} method with a plane wave excitation or a defocused transmit beam. Further clinical studies will be performed to test the effectiveness of contrast enhancement of microcalcifications using the CF_{MVDR} method.

5.2.3 Efficient Implementation of the Aperture Domain Processing Techniques

Recently, Graphics processing units (GPUs) will be used for diverse data-parallel computations to increase the programmability and performance of aperture domain processing. GPUs are eminently suitable for aperture domain processing since they can optimally perform the processing for individual channels in parallel. Fine-grained, data-parallel threads are the fundamental means of parallel execution on GPU. As

shown in Fig 5.1, launching a kernel creates a grid of threads that all execute the kernel function. When the kernel is launched at run-time, the kernel functions are executed by each individual created thread. To accelerate the beamforming processing, the STA method using GPU is the directly summing the weighted RF data with proper phase rotation and can be formulated as

$$y(t) = \sum_m \sum_n \sum_i \text{filter}(i) \cdot r(t + \tau + \frac{i}{fs}, m, n) \cdot e^{-j2\pi f_c(t + \frac{i}{fs} - \phi_{rot}(i,m,n))} \tag{5-1}$$

where the filter(i) is the coefficient of low pass filter corresponding to the i-th tap, $\phi_{rot}(i,m,n)$ is the corresponding phase rotation, and m and n denote the index of transmit and receive apertures, respectively. The throughput of the processing is improved since it minimizes the duplicate memory access operations. The Gauss-Jordan Elimination [71] approach is used in the matrix inversion of the adaptive imaging and individual raw operations are executed in accordance using multiple threads on GPU. Besides, the subaperture method [62] is cooperated in the autocovariance matrix estimation to improve the robustness and efficiency. The autocovariance matrix using subaperture method can be expressed as

$$\mathbf{R}_{xx} = \frac{1}{N - L + 1} \sum_{l=0}^{N-L} X_l^H(t) X_l(t) \tag{5-2}$$

where $X_l = \begin{bmatrix} x_l & x_{l+1} & \cdots & x_{l+L-1} \end{bmatrix}^T$, L is the number of subapertures, l is the subaperture index. Preliminary results have demonstrated that the parallel channel processing such as beam formation executed on GPU platform (NVidia GTX260) can be 238 times faster than those on the CPU platform. Furthermore, the CF_{MVDR} estimation for high frame rate imaging executed on GPU platform can be 3.2 times faster than that on the CPU platform. Based on the GPU processors, high speed and high accuracy aperture domain processing becomes more feasible and reliable.
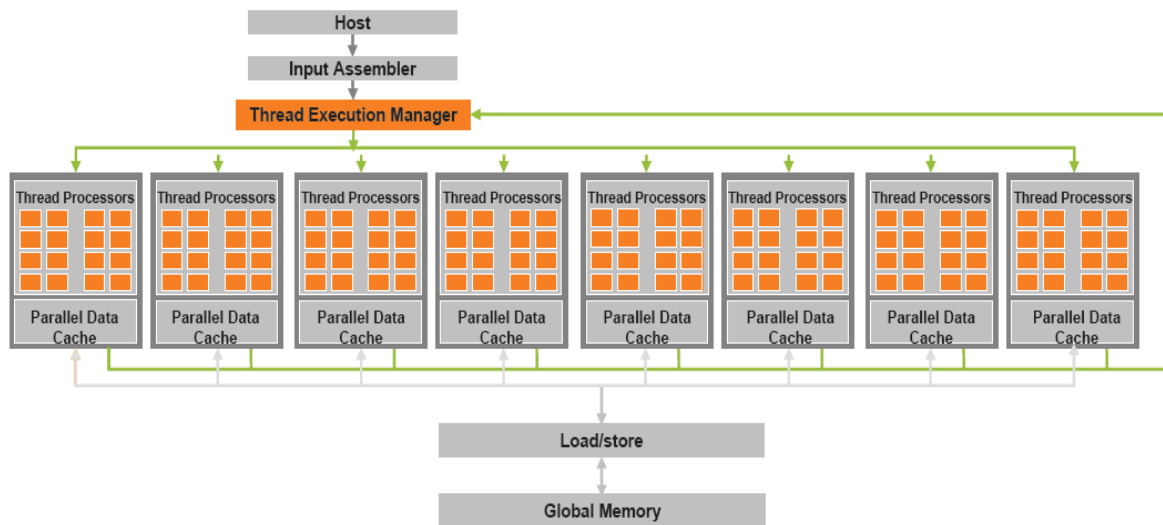
Fig. 5-1. Illustration of multi-processors executing multiple threads. (From: http://www.nvidia.com/)

Finally, the proposed aperture domain processing techniques including the adaptive imaging and vector velocity estimation or other techniques (e.g., parameter imaging for sound velocity [21] and attenuation coefficient [22]) will be integrated and performed on this GPU platform to achieve high-speed high-performance imaging .

REFERENCES

[1] J. Y. Lu, H. Zou, and J. F. Greenleaf, "Biomedical ultrasound beam forming," *Ultrasound Med. Biol.,* vol. 20, pp. 403-28, 1994.

[2] D. H. Johnson and D. E. Dudgeon, *Array signal processing : concepts and techniques.* Englewood Cliffs, NJ: Prentice Hall, 1993.

[3] S. W. Flax and M. O'donnell, "Phase-aberration correction using signals from point reflectors and diffuse scatterers - basic principles," *IEEE Trans. Ultrason., Ferroelectr., Freq. Control,* vol. 35, pp. 758-767, Nov 1988.

[4] M. O'Donnell and S. W. Flax, "Phase-aberration correction using signals from point reflectors and diffuse scatterers - measurements," *IEEE Trans. Ultrason., Ferroelectr., Freq. Control,* vol. 35, pp. 768-774, Nov 1988.

[5] S. Krishnan, K. W. Rigby, and M. O'Donnell, "Improved estimation of phase aberration profiles," *IEEE Trans. Ultrason., Ferroelectr., Freq. Control,* vol. 44, pp. 701-713, 1997.

[6] G. C. Ng, S. S. Worrell, P. D. Freiburger, and G. E. Trahey, "A comparative evaluation of several algorithms for phase aberration correction," *IEEE Trans. Ultrason., Ferroelectr., Freq. Control,* vol. 41, pp. 631-643, 1994.

[7] D. L. Liu and R. C. Waag, "Correction of ultrasonic wavefront distortion using backpropagation and a reference waveform method for time-shift compensation," *J. Acoust. Soc. Am.,* vol. 96, pp. 649-660, 1994.

[8] P.-C. Li and M. O'Donnell, "Phase aberration correction on two-dimensional conformal arrays," *IEEE Trans. Ultrason., Ferroelectr., Freq. Control,* vol. 42, pp. 73-82, 1995.

[9] P. C. Li, S. W. Flax, E. S. Ebbini, and M. O'Donnell, "Blocked element compensation in phased array imaging," *IEEE Trans. Ultrason., Ferroelectr., Freq. Control,* vol. 40, pp. 283-292, 1993.

[10] P. C. Li and M. Odonnell, "Improved detectability with blocked element compensation," *Ultrason. Imag.,* vol. 16, pp. 1-18, Jan 1994.

[11] S. Krishnan, L. Pai-Chi, and M. O'Donnell, "Adaptive compensation of phase and magnitude aberrations," *IEEE Trans. Ultrason., Ferroelectr., Freq. Control,* vol. 43, pp. 44-55, 1996.

[12] S. Krishnan, K. W. Rigby, and M. O'Donnell, "Efficient parallel adaptive aberration correction," *IEEE Trans. Ultrason., Ferroelectr., Freq. Control,* vol. 45, pp. 691-703, 1998.

[13] K. W. Hollman, K. W. Rigby, and M. O'Donnell, "Coherence factor of speckle from a multi-row probe," in *Proc. IEEE Ultrason. Symp.*, 1999, pp. 1257-1260.

[14] R. Mallart and M. Fink, "Adaptive focusing in scattering media through sound-speed inhomogeneities: The van Cittert Zernike approach and focusing criterion," *J. Acoust. Soc. Am.,* vol. 96, pp. 3721-3732, 1994.

[15] S. D. Silverstein, "Ultrasound scattering model: 2-D cross-correlation and focusing criteria-theory, simulations, and experiments," *IEEE Trans. Ultrason., Ferroelectr., Freq. Control,* vol. 48, pp. 1023-1030, 2001.

[16] P.-C. Li and M.-L. Li, "Adaptive imaging using the generalized coherence factor," *IEEE Trans. Ultrason., Ferroelectr., Freq. Control,* vol. 50, pp. 128-141, 2003.

[17] S.-L. Wang, C.-H. Chang, H.-C. Yang, Y.-H. Chou, and P.-C. Li, "Performance Evaluation of Coherence-Based Adaptive Imaging Using Clinical Breast Data," *IEEE Trans. Ultrason., Ferroelectr., Freq. Control,* vol. 54, pp. 1669-1679, 2007.

[18] M. E. Anderson, "Multi-dimensional velocity estimation with ultrasound using spatial quadrature," *IEEE Trans. Ultrason., Ferroelectr., Freq. Control,* vol. 45, pp. 852-861, May 1998.

[19] J. A. Jensen and P. Munk, "A new method for estimation of velocity vectors," *IEEE Trans. Ultrason., Ferroelectr., Freq. Control,* vol. 45, pp. 837-851, May 1998.

[20] S.-L. Wang, M.-L. Li, and P.-C. Li, "Estimating the blood velocity vector using aperture domain data," *IEEE Trans. Ultrason., Ferroelectr., Freq. Control,* vol. 54, pp. 70-78, 2007.

[21] S.-W. Huang and P.-C. Li, "Computed tomography sound velocity reconstruction using incomplete data," *IEEE Trans. Ultrason., Ferroelectr., Freq. Control,* vol. 51, pp. 329-342, 2004.

[22] S.-W. Huang and P.-C. Li, "Ultrasonic computed tomography reconstruction of the attenuation coefficient using a linear array," *IEEE Trans. Ultrason., Ferroelectr., Freq. Control,* vol. 52, pp. 2011-2022, 2005.

[23] J. A. Hossack, "Extended focal depth imaging for medical ultrasound," in *Proc. IEEE Ultrason. Symp.*, 1996, pp. 1535-1540 vol.2.

[24] J. A. Jensen, *Estimation of blood velocities using ultrasound : a signal processing approach.* Cambridge ; New York, USA: Cambridge University Press, 1996.

[25] J. R. Overbeck, K. W. Beach, and D. E. Strandness, Jr., "Vector Doppler: accurate measurement of blood velocity in two dimensions," *Ultrasound Med. Biol.,* vol. 18, pp. 19-31, 1992.

[26] P. J. Phillips, S. W. Straka, and O. T. v. Ramm, "Real-time two-dimensional vector velocity mapping ultrasound systems using subaperture pulse chasing," *Ultrason. Imag.,* vol. 18, p. 60, 1996.

[27] G. E. Trahey, J. W. Allison, and O. T. von Ramm, "Angle independent ultrasonic detection of blood flow," *IEEE Trans. Biomed. Eng.,* vol. 34, pp. 965-7, Dec 1987.

[28] L. N. Bohs, B. H. Friemel, and G. E. Trahey, "Experimental velocity profiles and volumetric flow via two-dimensional speckle tracking," *Ultrasound Med. Biol.,* vol. 21, pp. 885-98, 1995.

[29] V. L. Newhouse, E. S. Furgason, G. F. Johnson, and D. A. Wolf, "The dependence of ultrasound Doppler bandwidth on beam geometry," *IEEE Trans. Sonics Ultrason.,* vol. 27, pp. 50-59, 1980.

[30] V. L. Newhouse, D. Censor, T. Vontz, J. A. Cisneros, and B. B. Goldberg, "Ultrasound Doppler probing of flows transverse with respect to beam axis," *IEEE Trans. Biomed. Eng.,* vol. 34, pp. 779-789, Oct 1987.

[31] P. C. Li, C. J. Cheng, and C. C. Shen, "Doppler angle estimation using correlation," *IEEE Trans. Ultrason., Ferroelectr., Freq. Control,* vol. 47, pp. 188-196, Jan 2000.

[32] C. K. Yeh and P. C. Li, "Doppler angle estimation using AR modeling," *IEEE Trans. Ultrason., Ferroelectr., Freq. Control,* vol. 49, pp. 683-692, Jun 2002.

[33] S. A. Goss, R. L. Johnston, and F. Dunn, "Comprehensive compilation of empirical ultrasonic properties of mammalian-tissues," *J. Acoust. Soc. Am.,* vol. 64, pp. 423-457, 1978.

[34] E. Cherin, R. Williams, A. Needles, G. Liu, C. White, A. S. Brown, Y. Q. Zhou, and F. S. Foster, "Ultrahigh frame rate retrospective ultrasound microimaging

and blood flow visualization in mice in vivo," *Ultrasound Med. Biol.,* vol. 32, pp. 683-91, May 2006.

[35] J. Bercoff, M. Tanter, S. Chaffai, and M. Fink, "Ultrafast imaging of beamformed shear waves induced by the acoustic radiation force. Application to transient elastography," in *Proc. IEEE Ultrason. Symp.,* 2002, pp. 1899-1902 vol.2.

[36] M. O'Donnell, "Efficient parallel receive beam forming for phased array imaging using phase rotation [medical US application]," in *Proc. IEEE Ultrason. Symp.,* 1990, pp. 1495-1498 vol.3.

[37] D. P. Shattuck, M. D. Weinshenker, S. W. Smith, and O. T. Vonramm, "Explososcan: a parallel processing technique for high speed ultrasound imaging with linear phased-arrays," *J. Acoust. Soc. Am.,* vol. 75, pp. 1273-1282, 1984.

[38] J. Bercoff, M. Tanter, and M. Fink, "Supersonic shear imaging: a new technique for soft tissue elasticity mapping," *IEEE Trans. Ultrason., Ferroelectr., Freq. Control,* vol. 51, pp. 396-409, 2004.

[39] J.-Y. Lu, "2D and 3D high frame rate imaging with limited diffraction beams," *IEEE Trans. Ultrason., Ferroelectr., Freq. Control,* vol. 44, pp. 839-856, 1997.

[40] M. Karaman, L. Pai-Chi, and M. O'Donnell, "Synthetic aperture imaging for small scale systems," *IEEE Trans. Ultrason., Ferroelectr., Freq. Control,* vol. 42, pp. 429-442, 1995.

[41] J. Y. Lu and J. F. Greenleaf, "Ultrasonic nondiffracting transducer for medical imaging," *IEEE Trans. Ultrason., Ferroelectr., Freq. Control,* vol. 37, pp. 438-447, 1990.

[42] J.-y. Lu, J. Cheng, and J. Wang, "High frame rate imaging system for limited diffraction array beam imaging with square-wave aperture weightings high frame rate imaging system for limited diffraction array beam imaging with square-wave aperture weightings," *IEEE Trans. Ultrason., Ferroelectr., Freq. Control,* vol. 53, pp. 1796-1812, 2006.

[43] J. Wang and J. Y. Lu, "Effects of phase aberration and noise on extended high frame rate imaging," *Ultrason. Imag.,* vol. 29, pp. 105-21, Apr 2007.

[44] W. F. Walker and G. E. Trahey, "Aberrator integration error in adaptive imaging," *IEEE Trans. Ultrason., Ferroelectr., Freq. Control,* vol. 44, pp. 780-791, 1997.

[45] M. O'Donnell, "Efficient parallel receive beam forming for phased array imaging using phase rotation," in *Proc. IEEE Ultrason. Symp.*, 1990, pp. 1495-1498.

[46] W. F. Walker and G. E. Trahey, "A fundamental limit on delay estimation using partially correlated speckle signals," *IEEE Trans. Ultrason., Ferroelectr., Freq. Control,* vol. 42, pp. 301-308, Mar 1995.

[47] R. F. Gunst and R. L. Mason, *Regression analysis and its application : a data-oriented approach.* New York: M. Dekker, 1980.

[48] K. W. Ferrara and V. R. Algazi, "A statistical-analysis of the received signal from blood during laminar-flow," *IEEE Trans. Ultrason., Ferroelectr., Freq. Control,* vol. 41, pp. 185-198, Mar 1994.

[49] W. F. Walker and G. E. Trahey, "A fundamental limit on the performance of correlation-based phase correction and flow estimation techniques," *IEEE Trans. Ultrason., Ferroelectr., Freq. Control,* vol. 41, pp. 644-654, Sep 1994.

[50] J. A. Jensen, "Field: a program for simulating ultrasound systems," *Med. Biol. Eng. Comp.,* vol. 4, suppl. 1, pt. 1; Tenth Nordic-Baltic Conference on Biomedical Imaging, pp. 351-353, 1996.

[51] L. Thomas and A. Hall, "An improved wall filter for flow imaging of low velocity flow," in *Proc. IEEE Ultrason. Symp.*, 1994, pp. 1701-1704.

[52] F. Viola and W. F. Walker, "A comparison of the performance of time-delay estimators in medical ultrasound," *IEEE Trans. Ultrason., Ferroelectr., Freq. Control,* vol. 50, pp. 392-401, 2003.

[53] L. M. Hinkelman, D.-L. Liu, R. C. Waag, Q. Zhu, and B. D. Steinberg, "Measurements and correction of ultrasonic pulse distortion produced by human breast," *J. Acoust. Soc. Am.,* vol. 97, pp. 1958-1969, 1995.

[54] R. C. Gauss, G. E. Trahey, and M. S. Soo, "Adaptive imaging in the breast," in *Proc. IEEE Ultrason. Symp.*, 1999, pp. 1563-1569.

[55] G. E. Trahey, P. D. Freiburger, L. F. Nock, and D. C. Sullivan, "In vivo measurements of ultrasonic beam distortion in the breast," *Ultrason. Imag.,* vol. 13, pp. 71-90, Jan 1991.

[56] D. L. Liu and R. C. Waag, "Time-shift compensation of ultrasonic pulse focus degradation using least-mean-square error estimates of arrival time," *J. Acoust. Soc. Am.,* vol. 95, pp. 542-555, Jan 1994.

[57] Q. Zhu and B. D. Steinberg, "Wavefront amplitude distortion and image sidelobe levels. I. Theory and computer simulations," *IEEE Trans. Ultrason., Ferroelectr., Freq. Control,* vol. 40, pp. 747-753, 1993.

[58] Q. Zhu, B. D. Steinberg, and R. L. Arenson, "Wavefront amplitude distortion and image sidelobe levels. II. In vivo experiments," *IEEE Trans. Ultrason., Ferroelectr., Freq. Control,* vol. 40, pp. 754-762, 1993.

[59] R. Y. Chiao, L. J. Thomas, and S. D. Silverstein, "Sparse array imaging with spatially-encoded transmits," in *Proc. IEEE Ultrason. Symp.*, 1997, pp. 1679-1682 vol.2.

[60] T. X. Misaridis and J. A. Jensen, "Space-time encoding for high frame rate ultrasound imaging," *Ultrasonics,* vol. 40, pp. 593-597, May 2002.

[61] J. Capon, "High-resolution frequency-wavenumber spectrum analysis," *Proc. IEEE,* vol. 57, pp. 1408-1418, 1969.

[62] F. Vignon and M. R. Burcher, "Capon beamforming in medical ultrasound imaging with focused beams," *IEEE Trans. Ultrason., Ferroelectr., Freq. Control,* vol. 55, pp. 619-628, 2008.

[63] J. F. Synnevag, A. Austeng, and S. Holm, "Adaptive beamforming applied to medical ultrasound imaging," *IEEE Trans. Ultrason., Ferroelectr., Freq. Control,* vol. 54, pp. 1606-1613, Aug 2007.

[64] T. Hergum, T. Bjastad, K. Kristoffersen, and H. Torp, "Parallel beamforming using synthetic transmit beams," *IEEE Trans. Ultrason., Ferroelectr., Freq. Control,* vol. 54, pp. 271-280, 2007.

[65] S. Nikolov, K. Gammelmark, and J. A. Jensen, "Recursive ultrasound imaging," in *Proc. IEEE Ultrason. Symp.*, 1999, pp. 1621-1625.

[66] N. Oddershede and J. A. Jensen, "Effects influencing focusing in synthetic aperture vector flow imaging," *IEEE Trans. Ultrason., Ferroelectr., Freq. Control,* vol. 54, pp. 1811-1825, Sep 2007.

[67] S. T. Nikolov and J. A. Jensen, "In-vivo synthetic aperture flow imaging in medical ultrasound," *IEEE Trans. Ultrason., Ferroelectr., Freq. Control,* vol. 50, pp. 848-856, Jul 2003.

[68] S. P. Weinstein, C. Seghal, E. F. Conant, and J. A. Patton, "Microcalcifications in breast tissue phantoms visualized with acoustic resonance coupled with power Doppler US: Initial observations," *Radiology,* vol. 224, pp. 265-269, Jul 2002.

[69] N. Petrick, B. Sahiner, H. P. Chan, M. A. Helvie, S. Paquerault, and L. M. Hadjiiski, "Breast cancer detection: Evaluation of a mass-detection algorithm for computer-aided diagnosis - Experience in 263 patients," *Radiology,* vol. 224, pp. 217-224, Jul 2002.

[70] M. E. Anderson, M. S. C. Soo, and G. E. Trahey, "Microcalcifications as elastic scatterers under ultrasound," *IEEE Trans. Ultrason., Ferroelectr., Freq. Control,* vol. 45, pp. 925-934, 1998.

[71] G. Strang, *Introduction to linear algebra*, 3rd ed. Wellesly, MA: Wellesley-Cambridge, 2003.